

RPCVD Growth of Epitaxial Si-Ge-Sn Alloys for Optoelectronics Applications

By

Joe Margetis

A Dissertation Presented in Partial Fulfillment
of the Requirements for the Degree
Doctor of Philosophy

Approved April 2018 by the
Graduate Supervisory Committee:

Yong-Hang Zhang, Chair
Andrew Chizmeshya
Shane Johnson

ARIZONA STATE UNIVERSITY

May 2018

ABSTRACT

$\text{Ge}_{1-x}\text{Sn}_x$ and $\text{Si}_y\text{Ge}_{1-x-y}\text{Sn}_x$ materials are being researched intensively for applications in infra-red optoelectronic devices. Due to their direct band gap these materials may in-fact be the enabling factor in the commercial realization of silicon photonics/group IV photonics and the integration of nanophotonics with nanoelectronics. However the synthesis of these meta-stable semiconductor alloys, with a range of Sn-compositions, remains the primary technical challenge. Highly specialized epitaxial growth methods must be employed to produce single crystal layers which have sufficient quality for optoelectronic device applications. Up to this point these methods have been unfavorable from a semiconductor manufacturing perspective. In this work the growth of high-quality Si-Ge-Sn epitaxial alloys on Ge-buffered Si (100) using an industry-standard reduced pressure chemical vapor deposition reactor and a cost-effective chemistry is demonstrated. The growth kinetics are studied in detail in-order to understand the factors influencing layer composition, morphology, and defectivity. In doing so breakthrough GeSn materials and device results are achieved including methods to overcome the limits of Sn-incorporation and the realization of low-defect and strain-relaxed epitaxial layers with up to 20% Sn.

P and n-type doping methods are presented in addition to the production of SiGeSn ternary alloys. Finally optically stimulated lasing in thick GeSn layers and SiGeSn/GeSn multiple quantum wells is demonstrated. Lasing wavelengths ranging from 2-3 μm at temperatures up to 180K are realized in thick layers. Whereas SiGeSn/GeSn multiple quantum wells on a strain-relaxed GeSn buffers have enabled

the first reported SiGeSn/GeSn multiple quantum well laser operating up to 80K with threshold power densities as low as 33 kW/cm².

ACKNOWLEDGEMENT

It should be mentioned that completing a part-time PhD while working full-time with a wife and three little children at home has not been easy. It has been a long and hard sacrifice for me and my family. All PhD's require a tremendous support network of advisors, collaborators, friends, family, and at least in my case, faith. Therefore first and foremost I thank and acknowledge God; *Patris, et Filli, et Spiritus Sancti*, for the Grace and strength afforded to me despite my many mistakes, flaws, and personal failings.

My personal support network includes most importantly my wife Jennifer. She has accomplished super-human feats of motherhood over the last few years while I have been consumed by work projects, PhD research, and PhD course-work. All the while she has been there to support and encourage me even when it meant making her day more difficult, I am lucky to have her and forever indebted to her. To my family Jennifer, Jacob, Julia, and Elizabeth, I love you more than words can express. My grandparents Carmen and Patricia (RIP) Pignatiello who have been so supportive and encouraging of me in everything I do. My mother Kathleen (RIP) whom I am certain is guiding me from up above. My father Paul who taught me by his own example what it means to sacrifice for your family in the face of adversity and how to remain physically, emotionally, and spiritually disciplined. And finally I must acknowledge the U.S. Army and the U.S. Army Ranger School, which built upon the sense self-discipline and persistence in the face of adversity which I learned from my Father, and perfected it; Rangers Lead the Way. My

experiences in the Military, both good and bad - things I am proud of and not proud of, have left an indelible mark on who I have become as a man.

Professionally I must first thank Dr. John Tolle of ASM and Prof. Fisher Yu of the University of Arkansas for their mentoring and friendship. They have been the guiding forces behind this work and without them this work would have never even begun let alone be completed. I am grateful to Prof. Y.H. Zhang for agreeing to advise me in a part-time and off-campus PhD project. Many thanks go to Prof. Andrew Chizmeshya and Prof. Shane Johnson for agreeing to sit on my committee. All of my collaborators and co-authors in Prof. Fisher Yu's University of Arkansas group especially Prof. Wei Du, now at Wilkes-Barre University, for his tremendous effort in coordinating research details and paper proof-reading. Also Dr. Baohua Li of Arktonics, LLC for her organization of research efforts and logistics, and Air Force Office of Scientific Research which funded much of our work under SBIR # FA9550-16-C-0016.

I am thankful for my friends and co-workers at ASM (past and present) who helped with technical discussions, encouragement, and help covering work projects when I was spread too thin. Dr. Nupur Bhargava, Bobby Vyne, Mark Hawkins, Tom Kirschenieter, Doran Weeks, Dr. Somil Rathi, Dr. David Kohen, Dr. Raj Kumar, and Jennifer Spear to name just a few. We have a world-class equipment maintenance team at ASM, and many thanks to Eric Ellison and Damion Fugate, two of the best hardware technicians that I have ever had the privilege to work with. Last but not least I thank ASM's senior management namely, Dr. Alex Demos, who allowed this research work to

be done using company resources and gave official approval of our outside collaborations.

TABLE OF CONTENTS

	Page
LIST OF TABLES.....	viii
LIST OF FIGURES.....	ix
CHAPTER	
1.INTRODUCTION.....	1
1.1 Ge _{1-x} Sn _x Structural Characteristics and Electronic Properties.....	2
1.2 Si-Ge-Sn Epitaxial Growth Overview.....	5
2. EXPERIMENTAL METHODS.....	12
2.1. Theory of Epitaxial Growth.....	12
2.2 Epitaxial Growth Reactor.....	26
2.3. Germanium Buffer Layer Growth.....	30
3. GE _{1-x} SN _x LAYER GROWTH.....	35
3.1 Ge _{1-x} Sn _x Growth Kinetics.....	36
3.1.1. Precursor flow effects.....	36
3.1.2. Temperature effects.....	44
3.1.3. The Initial Stages of GeSn Growth.....	49
3.1.4. Gas-phase and Surface Chemistry.....	53
3.2 Materials characterization of undoped GeSn.....	60

CHAPTER	Page
4. STRAIN-RELAXATION AND THE LIMITS OF SN INCORPORATION	63
4.1 Strain relaxation and defect propagation	63
4.2 The effect of strain on Sn-incorporation	71
5. GROWTH OF UNDOPED $\text{Si}_y\text{Ge}_{1-x-y}\text{Sn}_x$	77
5.1 Introduction to $\text{Si}_y\text{Ge}_{1-x-y}\text{Sn}_x$	77
5.2 $\text{Si}_y\text{Ge}_{1-x-y}\text{Sn}_x$ growth results	78
6. GROWTH OF DOPED SI-GE-SN ALLOYS	84
6.1 p-type $\text{Ge}_{1-x}\text{Sn}_x$	84
6.2 n-type $\text{Ge}_{1-x}\text{Sn}_x$	88
7. OPTICALLY STIMULATED LASING IN GESN	92
8. QUANTUM WELL STRUCTURES	103
8.1 $\text{Ge}_{0.95}\text{Sn}_{0.05}/\text{Ge}_{0.9}\text{Sn}_{0.1}/\text{Ge}_{0.95}\text{Sn}_{0.05}$ Quantum Wells	104
8.2 $\text{Si}_{0.05}\text{Ge}_{0.95}\text{Sn}_{0.05}/\text{Ge}_{0.9}\text{Sn}_{0.1}/\text{Si}_{0.05}\text{Ge}_{0.95}\text{Sn}_{0.05}$ Quantum Wells	108
8.3 Interfacial Composition Control in Quantum Wells	111
8.4 Multiple Quantum Wells on Strain-relaxed Buffer Layers	117
CONCLUSIONS	123
REFERENCES	125

LIST OF TABLES

TABLE	Page
1 Summary Of Ge-buffer Layer Annealing.....	33
2 Summary Of Sample XRD-RSM Characteristics	67
4 Summary Of QW Strain And Band Offsets.....	106
5 Summary Of QW Strain And Band Offsets	110
6 Summary Of Barrier Layer Asymmetry	115
7 Summary Of MQW Strain.....	122

LIST OF FIGURES

FIGURE	Page
1. Ge Bandstructure Diagram.....	3
2. GeSn Bandgaps As A Fucntion Of Strain And Composition	5
3. Surface Processes During Epitaxial Growth	16
4.Thin film And Epitaxial Growth Phase Diagram	18
5. Illustration Of The Reconstructed Si/Ge(100) Surface Viewed Along The [110]	19
6. Thin film And Epitaxial Growth Phase Diagram For Meta-Stable Materials.	22
7. Epsilon® 2000 RPCVD System	28
8. Epsilon® 2000 RPCVD Chamber	29
9. EPD AFM Image For Ge-buffer	33
10. HRXRD RSM of Ge buffer Layer.	34
11. GeSn Growth Rate Vs. SnCl ₄ /GeH ₄	37
12. GeSn Growth Rate Vs. SnCl ₄ /GeH ₄ For Two Temperatures And Types Of Carrier Gas .	39
13. %Sn Vs. SnCl ₄ /GeH ₄ For Two Temperatures And Both Types Of Carrier Gas.	40
14. Precursor Incorporation Efficiency Vs. the SnCl ₄ /GeH ₄ In Both Carrier Gases At A Fixed Temperature.....	42
15. Precursor Incorporation Efficeincy vs. The SnCl ₄ /GeH ₄ In H ₂ Carrier Gas At Two Different Temperatures.	43
16.Reaction Order Plot.....	44
17. Arrhenius Plot For The Ge, Sn, Component And Total Growth Rates	46
18. Arrhenius Plot For The Ge, Sn, Component And Total Growth Rates	46
19. %Sn Incorporated Vs. Temperature For Two SnCl ₄ /GeH ₄ Conditions.	48

FIGURE	Page
20. Comparison Of The Sn-incorporation Vs. Temperature.....	48
21. GeSn Layer Thicknesses vs. Growth Time For 3% And 7% Sn Layers.....	51
22. AFM Images Of The Initial Stages Of Growth	52
23. LEIS Spectra For The Initial Stages Of Gesn Growth	52
24. Gibbs Free Energy vs. Temperature For Reactions 42 and 43.	55
25. Reaction Pathways Diagram	59
26. HR-XRD Of GeSn Layers With 1-12% Sn	61
27. Random And Channeled RBS Spectra Of A 5%Sn Layer.	61
28. PL For 1-2% Sn Layers With Pure Ge Included As A Reference	62
29. Cross-sectional TEM Image Of The 570 Nm Layer.	69
30. XRD-RSM's For 152 nm And 865 nm Layers.....	70
31. SIMS Sn-depth Profiles For Relaxed Layers	71
32. Sn Incorporated At Fixed Growth Conditions While Only Varying The Starting Lattice Constant Of The Relaxed Gesn Buffer Layer.	76
33. 150 K Photoluminescence Spectrum Of A 17.5% Sn Layer Which Was Grown On The Multi-Layered Buffer.....	76
34. Lattice Constants And Band Gaps	77
35. Growth Rate Of SiGeSn vs. SiH ₄ /GeH ₄	81
36. SIMS Comparison Of SiGeSn.....	82
37. HRXRD Scans Of SiGeSn Layers With Various Compositions And Lattice Constants...	83
38. Growth Rate And %Sn-incorporation As A Function Of B ₂ H ₆ Flow.....	86
39. Boron Incorporation Vs. SnCl ₄ /GeH ₄ At Four Different B ₂ H ₆ Flows	86

FIGURE	Page
40. SIMS Depth Profile Of A GeSn:B Layer On Ge-Buffered Si.	87
41. Chemical B Concentration As Determined By SIMS And The Resistivity As A Function Of The B_2H_6 Flow.....	88
42. Growth Rate And The Sn Composition As A Function PH_3 Flow	90
43. SIMS Depth Profile For A GeSn:P Layer On Ge-Buffered Si	90
44. As And P SIMS Content As A Function Of Equal AH_3/PH_3 Respective Flow Rates.	91
45. Temperature-dependent PL Spectra Of Samples D And G.	95
46. Cross-sectional Schematic Of Optical Pumping Structures	96
47. Sample D Light Output Power Versus Pump Laser Power At Various Temperatures.. ...	97
48. Sample G Light Output Power Versus Pump Laser Power At Various Temperature.....	98
49. Threshold Power Density Vs. Temperature for sample D.	100
50. GeSn Laser Performance Characterization.	101
51. Lasing Spectra Of Samples D And G	102
52. Cross-sectional TEM And SIMS Depth Profile Of A $Ge_{0.95}Sn_{0.05}/Ge_{0.9}Sn_{0.1}/Ge_{0.95}Sn_{0.05}$ Structure..	105
53. XRD-RSM Of Quantum Well.	106
54. Calculated Band Alignment And The Energy Sub-Band Levels For The $Ge_{0.95}Sn_{0.05}/Ge_{0.9}Sn_{0.1}/Ge_{0.95}Sn_{0.05}$ QW	107
55. XRD-RSM On The $Si_{0.05}Ge_{0.95}Sn_{0.05}/Ge_{0.9}Sn_{0.1}/Si_{0.05}Ge_{0.95}Sn_{0.05}$	110
56. Calculated Band Alignment And The Energy Sub-Band Levels For The $Si_{0.05}Ge_{0.95}Sn_{0.05}/Ge_{0.9}Sn_{0.1}/Si_{0.05}Ge_{0.95}Sn_{0.05}$	111
57. SIMS Depth Profile Of Two $Ge_{0.95}Sn_{0.05}/Ge_{0.9}Sn_{0.1}/Ge_{0.95}Sn_{0.05}$ QW's	113

FIGURE	Page
58. Temperature And Flow During The Course Of The $\text{Ge}_{0.95}\text{Sn}_{0.05}/\text{Ge}_{0.9}\text{Sn}_{0.1}/\text{Ge}_{0.95}\text{Sn}_{0.05}$ Compensated And Uncompensated QW's	114
59. SIMS Depth Profile Of A SiGeSn/GeSn QW.	116
60. SIMS Depth Profile Of A 4x $\text{Si}_{0.03}\text{Ge}_{0.9}\text{Sn}_{0.07}/\text{Ge}_{0.86}\text{Sn}_{0.14}$ MQW On A Strain-relaxed $\text{Ge}_{0.91}\text{Sn}_{0.09}$ Buffer Layer.....	118
61. Cross-sectional TEM Of The 4x $\text{Si}_{0.03}\text{Ge}_{0.9}\text{Sn}_{0.07}/\text{Ge}_{0.86}\text{Sn}_{0.14}$ MQW.	119
62. Lattice Space Map Of 4x $\text{Si}_{0.03}\text{Ge}_{0.9}\text{Sn}_{0.07}/\text{Ge}_{0.86}\text{Sn}_{0.14}$ MQW On A Strain-Relaxed $\text{Ge}_{0.91}\text{Sn}_{0.09}$ Buffer Layer.....	119
63. Band Diagram For The 4x $\text{Si}_{0.03}\text{Ge}_{0.9}\text{Sn}_{0.07}/\text{Ge}_{0.86}\text{Sn}_{0.14}$ MQW	120
64. Compares Optical Pumping (top) And PL (bottom) At 10K And 80K For The 4x $\text{Si}_{0.03}\text{Ge}_{0.9}\text{Sn}_{0.07}/\text{Ge}_{0.86}\text{Sn}_{0.14}$ MQW	121
65. L-L Output For The MQW at 10,40, And 80K.	122

CHAPTER 1

INTRODUCTION

$\text{Ge}_{1-x}\text{Sn}_x$ and $\text{Si}_y\text{Ge}_{1-x-y}\text{Sn}_x$ materials offer promising technical advantages compared to traditional group IV semiconductors. The incorporation of Sn into SiGe and Ge enables novel strain engineering in advanced complementary metal oxide semiconductors (CMOS) devices due to the tunable lattice constant [1,2]. The alloy also has a tunable band gap which transitions to direct bandgap material at Sn compositions greater than ~8%. These are unique qualities among group IV semiconductors making it ideal for optoelectronic device applications and likely the enabling technology in “silicon photonics” [3]. The great potential of this material has been demonstrated with recent reports of GeSn-based lasers [4,5]. Despite these encouraging results GeSn has not yet been adopted in any commercialized semiconductor device applications which is mainly due to the lack of mature materials growth techniques. Epitaxial growth of device quality alloys is difficult for a number of reasons such as lattice mismatch/strain leading to high dislocation density [6], Sn-segregation/precipitation [7], and amorphous inclusions [8]. Over the past a few years several research groups have demonstrated high-quality layers using various growth methods [9-14]. In order for GeSn to enable group IV photonics the epitaxial growth method must be compatible with high-volume semiconductor manufacturing practices. Therefore, this requirement excludes techniques which utilize molecular beam epitaxy (MBE) or ultra-high vacuum chemical vapor deposition (UHV-CVD). Techniques which employ expensive, non-standard precursors such Ge_2H_6 and SnD_4 are also questionable in their manufacturing suitability.

In this work we investigate the use of industry standard precursors SiH_4 , GeH_4 and SnCl_4 , to deposit epitaxial GeSn/SiGeSn on the industry standard ASM Epsilon® 2000 chemical vapor deposition reactor. This work focuses on identifying the factors that govern Sn-incorporation and defect generation in the epitaxial layer using the SiH_4 , GeH_4 and SnCl_4 chemistry. Moreover, we demonstrate how an understanding of the growth kinetics, Sn-incorporation, and strain-relaxation can be used to produce Si-Ge-Sn bulk and heterostructure lasers.

1.1 $\text{Ge}_{1-x}\text{Sn}_x$ STRUCTURAL CHARACTERISTICS AND ELECTRONIC PROPERTIES

The optical properties of indirect band gap group IV semiconductors can be engineered by modifying the bandstructure. Doping, tensile-strain, and alloying can be used separately or in combination to engineer the bandstructure and optical properties. The energy separation in germanium's indirect (L) and direct (Γ) band gaps is ~ 140 meV which is quite small and makes it an ideal material for band structure modification. It has even been shown that high levels of n-type doping in germanium can influence direct gap behavior without directly modifying the bands [15,16]. The Ge bandstructure is shown in figure 1 below, for heavily doped n-type material the position of the Fermi level allows for thermal exchange of electrons out of the indirect valley and into the direct valley.

The application of strain modifies the symmetry of the crystal lattice and can change the band structure of a semiconductor. In germanium, biaxial tensile-strain in particular is beneficial for optical properties. The application of tensile-strain lifts the degeneracy of

the valence bands and the light hole (LH) band moves up in energy relative to the heavy hole (HH) band. Additionally tensile-strain will make the Γ -energy gap decrease relative to the L-energy gap such that at $\sim 1.5\%$ tensile strain germanium becomes a direct gap material [15]. Alloying germanium with tin also moves Γ -energy gap down relative to the L-energy gap which enables tuning of the band gap in the infra-red range. The amount of Sn required to make $E_g^\Gamma < E_g^L$ is not a simple linear interpolation between the band gap of pure germanium and pure tin. Such a linear interpolation would put the direct crossover at $x = 0.2$, it is experimentally found however that there is a large bowing in the energy gap vs. x relationship [17, 18]. This relationship can be expressed as:

$$E(x) = E_{Sn} \cdot x + E_{Ge} \cdot (1-x) - b \cdot x(1-x) \quad (1)$$

Where E_{Sn} is the band gap of Sn, E_{Ge} is the band gap of Ge, and b is the bowing

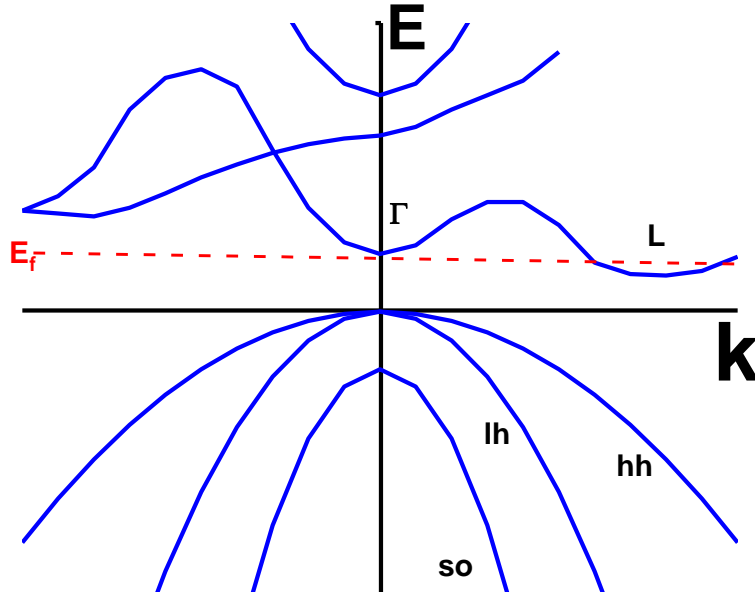


Figure 1. Band-diagram of a highly doped n-type germanium the red dashed line is the Fermi level. Even though the Fermi level is below the Γ -valley the Fermi-tail extends into the Γ -valley making electron occupation increasingly probable [10]

coefficient. It is generally agreed that the direct gap crossover point is between 6-8% Sn [17,18] however this result assumes a strain-free layer. Adding Sn to the Ge lattice will also increase the lattice constant of the material as:

$$a_{GeSn}(x) = a_{Sn}x + a_{Ge}(1 - x) - bx(1 - x) \quad (2)$$

Where $a_{Sn} = 6.489 \text{ \AA}$, $a_{Ge} = 5.658 \text{ \AA}$, and b is the bowing parameter. Figure 2 below illustrates how the direct crossover point varies with Sn content and strain-state as predicted by Gupta and coworkers [17]. It can be seen from this figure that compressive strain counter-acts the addition of Sn, and tensile strain assists the addition of Sn in terms of direct gap conversion. Therefore in-theory it is desirable to grow $Ge_{1-x}Sn_x$ alloys on substrates which are lattice-matched or even substrates having a slightly larger lattice constant. However, one of the primary attractions of GeSn as an optoelectronic material is integration on a silicon platform. This means that growth of GeSn directly on silicon or Ge-buffered silicon will result in a compressively strained layer. Relaxation of the layer via annealing or growth beyond the critical thickness can relieve the compressive strain in the layer however the introduction of dislocations due to relaxation can be detrimental to the radiative recombination efficiency.

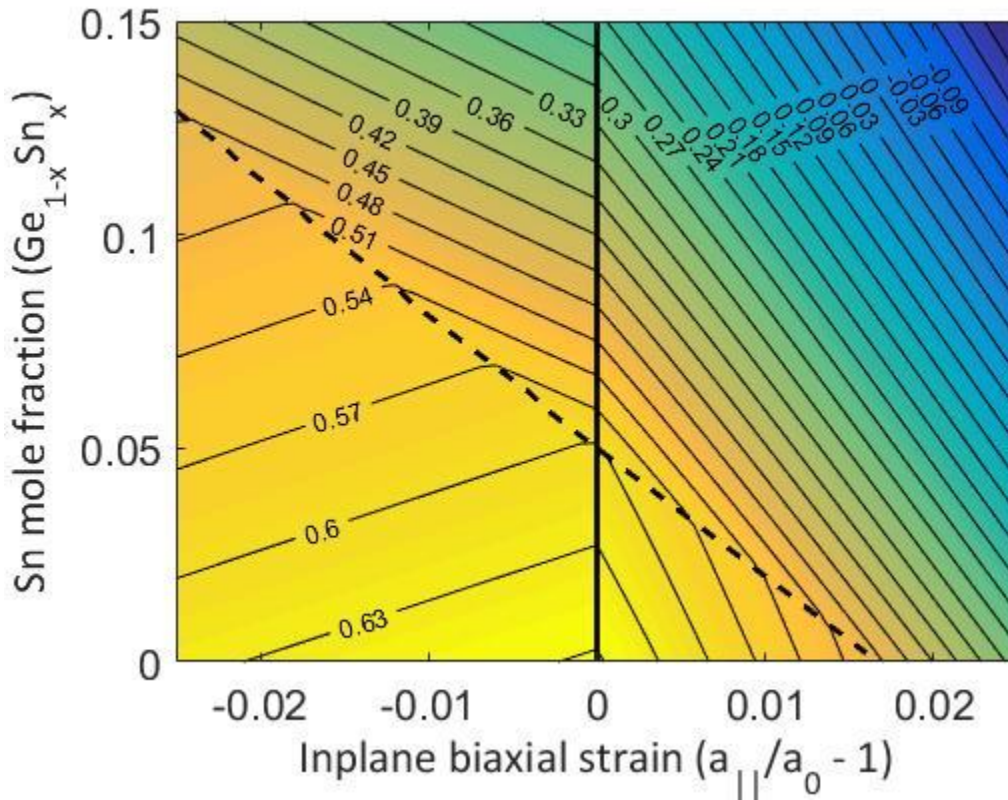


Figure 2. (a) Contour plot of bang gap with strain and Sn-content the solid black line divides regions of compressive and tensile strain. The dashed black line divides regions of indirect and direct band gap (b) is the same plot only the energy offset in direct and indirect gaps make-up the contours.

1.2 SI-GE-SNEPITAXIAL GROWTH OVERVIEW

In reviewing epitaxial growth technology of GeSn we limit our discussion to that which is relevant to achieving CMOS compatible integrated photonics. There is a ~ 13% lattice mismatch between Sn and Ge therefore strain is a highly important consideration. Lattice matched $\text{Ge}_{1-x}\text{Sn}_x$ has been demonstrated on $\text{In}_{1-x}\text{Ga}_x\text{As}$ buffered GaAs [22] however the practicality of this approach is limited.. These works are interesting in their own right however in terms of achieving CMOS compatible photonics do not make

technical sense. That is to say, if one has gone to the trouble of integrating III-V materials as buffer layers on Si (100) then why not just use a better performing III-V light source as well? The promise of Si-Ge-Sn photonic materials is not in their superior performance relative to their III-V counterparts, but in their integratability. This means we have omitted work which has used III-V growth substrates and/or III-V buffer layers. For similar reasons we also tend to focus on CVD-based approaches and only briefly discuss MBE-grown GeSn, in 300 mm silicon CMOS fabs one does not find MBE machines.

Successful epitaxial growth of GeSn relies on non-equilibrium conditions at low temperatures to suppress Sn-surface segregation and precipitation caused by the insolubility of Sn in Ge and the instability of diamond Sn above 13°C. Sn-solubility is strain dependent however for unstrained bulk GeSn is ~ 1%. Thermodynamic limits are overcome by limiting the kinetic pathways leading to secondary phase formation. These pathways are in general:

- 1.) Segregation: the preferential diffusional site-exchange of subsurface Sn atoms with surface Ge atoms resulting in a larger surface Sn fraction relative to the bulk Sn fraction.
- 2.) Surface diffusion: mobile Sn surface atoms seek sites which are energetically favorable for secondary phase formation.
- 3.) Precipitation: the accumulation of Sn atoms at energetically favorable sites allows for secondary phase formation.

Low growth temperatures limit the available thermal energy such that steps 1 and 2 are frustrated [19,20]. Growth pressure and the growth rate, GR, can also kinetically limit the approach to equilibrium. A higher pressure decreases the surface diffusivity via increased collisional frequency between surface species. While an increased growth rate can be used to “bury” the Sn faster than it can be exchanged to the surface. There is a time interval, Δt , available for exchange to the surface and it is equal to the time it takes to deposit one monolayer ($a/4$), $\Delta t = a/4(GR)$ [21]. By increasing the growth rate Δt is minimized, Sn is buried more efficiently, and thus more Sn is retained in the film.

MBE utilizes low growth rate UHV conditions such that growth temperatures must be $< 200^\circ\text{C}$ to achieve sufficient departure from equilibrium and successful GeSn growth. MBE-grown single crystal $\text{Ge}_{0.92}\text{Sn}_{0.08}$ on Ge (100) was demonstrated by Shah et. al. as early as 1987 [23] and IBM soon followed with $\text{Ge}_{0.7}\text{Sn}_{0.3}$ on Ge-buffered Si (100) [24]. The IBM group noted the strong tendency for the Sn atoms to surface-segregate and using reflection high energy electron diffraction (RHEED) they were able to determine that Sn does not immediately incorporate into the growing layer despite constant Sn atomic flux to the surface. He and Atwater were the first to demonstrate that the optical properties change with Sn content in MBE grown $\text{Ge}_{1-x}\text{Sn}_x$ by using optical transmittance measurements to map the absorption critical-points for alloys of $x = 0.06, 0.11, \text{ and } 0.15$ [25]. Sn compositions of up to 25% have been reported in MBE-grown materials on Si [26]. Of course to achieve this, the growth temperature was lowered to 120°C and there has been no analysis of the light emitting quality of those materials. These ultra-low growth temperatures are a key advantage of MBE over CVD; there is no need to provide

sufficient energy for chemical reactions. However these low growth temperatures may negatively impact point defect density of the layer resulting in non-radiative recombination centers.

In CVD of-course the surface reaction chemistry is of vital importance in determining the growth rate and Sn-incorporation. In general Ge-hydrides ($\text{Ge}_n\text{H}_{2n+2}$) are reacted with SnCl_4 or SnD_4 to form GeSn. Higher-order Ge-hydrides have the advantage of higher growth rate relative to lower-order hydrides at the same temperature. However higher-order Ge-hydrides are more expensive, Ge_2H_6 is $\sim 10x$ the cost of GeH_4 per unit mass. Additionally, Sn-hydrides are extremely unstable and expensive to produce in-fact to synthesize stable Sn-hydrides deuterium must be used in place of hydrogen. This molecule, SnD_4 , is still only marginally more stable and still requires specialized handling to avoid decomposition prior to its use in epitaxial growth.

The first demonstration of CVD-grown epitaxial GeSn was in 2001 by the Kouvetakis group at Arizona State University which utilized SnD_4 and Ge_2H_6 in ultra-high vacuum (UHV) at 350°C [9]. Soon afterwards this same group was the first ever to demonstrate epitaxial growth of the ternary alloy $\text{Si}_y\text{Ge}_{1-x-y}\text{Sn}_x$ [26]. Again UHV conditions were employed at 350°C to first grow a GeSn buffer on Si (100). Then SnD_4 was used with H_3SiGeH_3 to deposit the ternary layer and compositions of $y = 0.14$ and $x = 0.02-0.06$ were realized. H_3SiGeH_3 although requiring specialized synthesis has the benefit of preformed Si-Ge units for facile incorporation into the lattice. This group must be credited with bringing Si-Ge-Sn materials to the technological mainstream. Along with their early breakthroughs in CVD epitaxial growth they systematically began

studying the optical properties of these materials by spectroscopic ellipsometry and Raman spectroscopy [27]. They were also the first to report photoluminescence (PL) from GeSn which demonstrated its potential as a group IV light emitter [Matthews]. Finally, the ability to dope the material *n* and *p*-type by common doping precursors such as PH₃ and B₂H₆ confirmed its utility as an optoelectronic material [28].

H₃SiGeH₃ although beneficial due to the preformed Si-Ge units does place constraints on compositional adjustment because the Si and Ge precursors cannot be changed independently. Therefore the ASU group later developed UHV-CVD growth processes based on SnD₄, Ge₂H₆, and Si₃H₈ [29] and then mixtures on higher order germanes and silanes e.g. Si₄H₁₀ and Ge₄H₁₀ [30]. These were again significant breakthroughs in epitaxial growth technology however the method and precursors were still highly specialized and thus not scalable to manufacturing.

IMEC was the first to show that GeSn could be grown on an industrial CVD reactor, Vincent et. al. used SnCl₄ and Ge₂H₆ on an ASM Epsilon® at atmospheric pressure and 320°C [10]. They were able to achieve doped and undoped layers with up to 8% Sn. Wirths et. al. used SnCl₄, Ge₂H₆, and Si₂H₆ to achieve GeSn and SiGeSn with Sn contents up to 12% and Si contents up to 19% [31]. The use of SnCl₄ was a significant step forward in terms of growth chemistry because this precursor is more stable and more readily available than SnD₄. The presence of Cl in the molecule also has potential benefit in applications requiring selective area growth however this has not yet been reported using higher-order germanes and silanes.

The next major achievement in growth chemistry was our demonstration of a GeH_4 and SnCl_4 based process for GeSn [12] and SiH_4 was added to achieve SiGeSn [32]. This chemistry was in-fact selective to SiO_2 , perhaps due to the lower nucleation efficiency of GeH_4 relative to Ge_2H_6 . Furthermore, the low cost and widespread availability of these chemicals in large-scale fabs makes this the best choice for GeSn/SiGeSn integration into CMOS processing. The disadvantage of this choice seemed to be in comparing Sn incorporation between GeH_4 and Ge_2H_6 .

As we have explained in section 1.1 applications in group IV photonics would favor growth on Si or Ge-buffered silicon. Which means GeSn layers will always initially grow compressively strained. For optoelectronic applications this strain must be relieved in some manner preferably while minimizing dislocation density. Annealing at elevated temperatures has had limited success in this regard [33] as the thermal energy required for strain relaxation also induces Sn precipitation. Growth beyond the critical thickness must be carefully controlled because dislocations and extended defects can act as nucleation centers for secondary phase formation.

Our growth method utilizes a relaxed Ge buffer layer for GeSn growth so that GeSn layer relaxation can be better controlled. Growth directly on silicon was found to relax at very low thickness in an uncontrolled manner. The defect density of this Ge buffer layer must be minimized so that threading dislocations do not propagate into the GeSn layer. GeSn layer relaxation and defect control is discussed in detail in chapter 4, leading to our demonstration of a GeSn laser. Finally our understanding of the surface

chemistry and strain evolution are combined to maximize Sn-incorporation and extend produce GeSn materials emitting light at world-record wavelengths.

CHAPTER 2

EXPERIMENTAL METHODS

2.1. THEORY OF EPITAXIAL GROWTH

Epitaxial crystal growth has been and continues to be a primary enabling technology in the production of electronic and optoelectronic devices. The ability to grow low-defect density layers with tailored doping and/or composition profiles allows a wide array of semiconductor heterojunctions to be realized. However achieving intended results requires an understanding of the physical and chemical phenomena occurring on the surface during crystal growth. Epitaxial layers can be deposited by physical vapor deposition methods such as molecular beam epitaxy (MBE) or chemical vapor deposition methods. The fundamental mechanisms governing epitaxial growth can be applied to both MBE and CVD therefore we start with a discussion of these fundamentals and then specifically on CVD surface chemical reactions.

In epitaxial growth from the vapor phase either atomic or molecular species must be transported to the surface. The rate of impingement of atoms and/or molecules on the surface per unit time and area is called the flux, F , and can be expressed as:

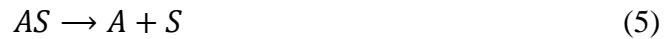
$$F = \frac{P}{\sqrt{2\pi mk_B T}} \quad (3)$$

Where P is the pressure, T is the temperature, m the atomic/molecular mass, and k_B is Boltzmann's constant. Incoming atomic and/or molecular species may adsorb on the

surface either by weak Van Der Waal's interaction (physisorption) or by forming a chemical bond with atoms on the surface (chemisorption). In the former case the energy of interaction between the surface and adsorbate is $\sim 0.01-0.1$ eV and in the latter the case energies are typically 1-5 eV. Therefore, physisorbed species can easily gain the necessary energy to leave the surface by desorption using surface lattice vibrations as a thermal reservoir. However atomic and molecular adspecies which first physisorb may then form chemical bonds with surface atoms once initial energetic and kinetic barriers are overcome. Adsorption kinetics are often modeled using the Langmuir isotherm which accounts for the rate dependence on the number of open adsorption sites. Consider adsorbate A which reacts with the surface S :



which is for adsorption, and for desorption we have:



The adsorption and desorption rates can then be written as:

$$r_a = k_a[A] \theta \quad (6)$$

$$r_d = k_d(1 - \theta) \quad (7)$$

where k_a and k_d are the rate constants, $[A]$ is the concentration of the adsorbate, and θ is the fraction of open surface sites. An expression for the number of open sites can be derived by considering that at equilibrium $r_a = r_d$ so that:

$$\frac{(1-\theta)}{\theta} = \frac{k_a}{k_d} [A] \quad (8)$$

and finally [34]:

$$\theta = \frac{1}{1 + \frac{k_a}{k_d} [A]} \quad (9)$$

This represents the simplest case of adsorption and in reality the probability that the adsorbate will stick to the surface must also be considered. This probability is called the sticking coefficient, $s_o(\theta)$, and it is typically also dependent on the surface coverage. An additional complication is that often times the adsorbing species requires more than one surface site. This is the case for disassociative adsorption of molecular species and it will change the expression for adsorption rate from a first-order dependence on θ to a n^{th} -order dependence. Combing equations 3 and 6 we can rewrite the adsorption rate in a more sophisticated way as:

$$r_a = s_o(\theta) k_a \theta^n \frac{P}{\sqrt{2\pi m k_B T}} \quad (10)$$

where we have replaced $[A]$ with the flux. Also recognizing that the rate constant is a Boltzmann-type expression with a specific activation energy, E_{ads} , we can finally write [34]:

$$r_a = s_o(\theta) \exp(-E_{ads}/k_b T) \theta^n \frac{P}{\sqrt{2\pi m k_B T}} \quad (11)$$

The thermal reservoir also provides energy for adspecies to diffuse on the surface and seek more energetically favorable sites. The time between diffusion and desorption attempts is given by:

$$\tau_{dif} = v^{-1} \exp\left(\frac{E_{dif}}{k_b T}\right) \quad (12)$$

$$\tau_{des} = v^{-1} \exp\left(\frac{E_{des}}{k_b T}\right) \quad (13)$$

Where v is the lattice vibrational frequency and E_{dif}/E_{des} are the respective activation energies. If a is the distance between surface sites then the diffusion constant can be defined as:

$$D = \frac{a^2}{4} v \exp\left(\frac{E_{dif}}{k_b T}\right) \quad (14)$$

The RMS distance traveled during random Brownian motion is given by $\langle x \rangle = (D\tau)^{1/2}$ before desorption. This distance can also be written as $\langle x \rangle = a \exp\left(\frac{E_{des}-E_{dif}}{2k_B T}\right)$ so that difference in desorption and diffusion energies represents how easily an adatom can be incorporated at various sites. In the simple terrace-ledge-kink model adatoms diffuse along atomic terraces and are ideally incorporated into regions of atomic steps called ledges and kinks. Ideally for epitaxial growth adatoms are able to diffuse and incorporate to ledges and kinks before being captured by nuclei which may form on the terraces. The more that separate nuclei are allowed to form on the terraces the more likely it is that the growth will be polycrystalline. A diagram of these surface process are shown in figure 3.

There is a net flux of material leaving the surface F_s , that is in balance with the incoming flux F at equilibrium. In order to have net condensation or film growth $F > F_s$ or equivalently the pressure P of the incoming flux must be greater than the vapor pressure of the material p_s . The ratio of these two pressures P/p_s is defined as the supersaturation, or simply S , a quantity which is linked to the thermodynamic driving force for film growth ΔG . If the flux to the surface is fixed and the temperature of the

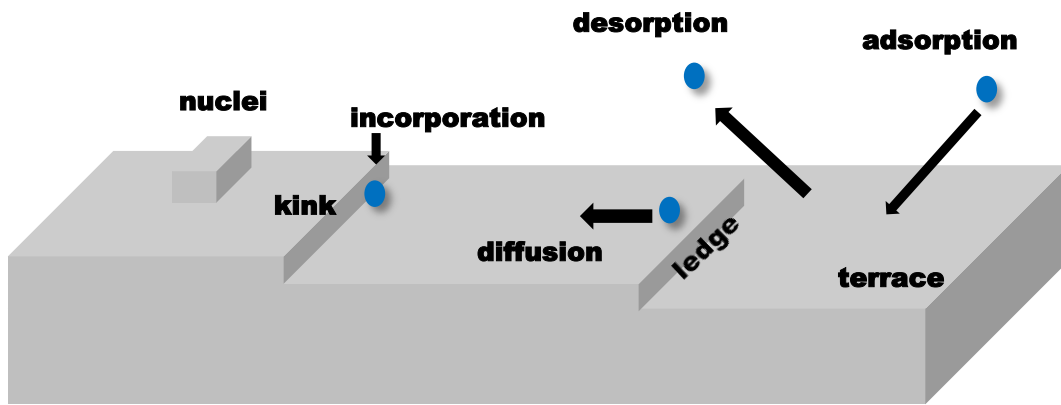


Figure 3 shows the various processes occurring at the surface during epitaxial growth. The adatom must adsorb, diffuse, and incorporate at a step-ledge before desorption or capture by nuclei on the terrace

substrate is increased then S will decrease due to the higher vapor pressure at the substrate. The cost in energy to transfer n atoms from the vapor phase to the condensed phase is:

$$\Delta G = -nk_bT \ln(S) \quad (15)$$

Without supersaturation $\Delta G \geq 0$ and nucleation and growth will not proceed at all. In the simple case of classical homogenous nucleation the total change in free energy of nuclei formation is a combination of volume free energy ΔG_v and interfacial energy γ . During the initial phases of nucleation the increase in γ counteracts the energy decrease from ΔG_v

and the nuclei are unstable until a critical volume of material is formed. It can be shown that the critical radius size is $r^* = -2\gamma/\Delta G_v$, so that high a supersaturation leads to small sized critical nuclei. High supersaturation also leads to high nucleation rates which is why for epitaxial growth low supersaturation is desired. In this way adatom diffusion to ledges/kinks is enabled while the formation rate of terrace nuclei is low [34].

Figure 4 below illustrates these concepts as film growth phase diagram, it is seen that epitaxial growth tends to the high temperature/low pressure limit. This is because at high temperature the adatom mobility is increased due to thermal activation and it can more easily reach the ledge before being captured on the terrace. Adatom mobility is also increased at low pressure however it more importantly lowers the supersaturation and the nucleation rate. MBE typically achieves epitaxial growth conditions through the use of extremely low pressures/low supersaturation. CVD on the other hand can produce epitaxial layers at high pressures by increasing the corresponding growth temperature and maximizing adatom mobility. As the pressure is increased and the temperature is decreased the layer becomes polycrystalline and ultimately amorphous. This is due to the kinetic frustration of adatoms and the ever increasing nucleation density.

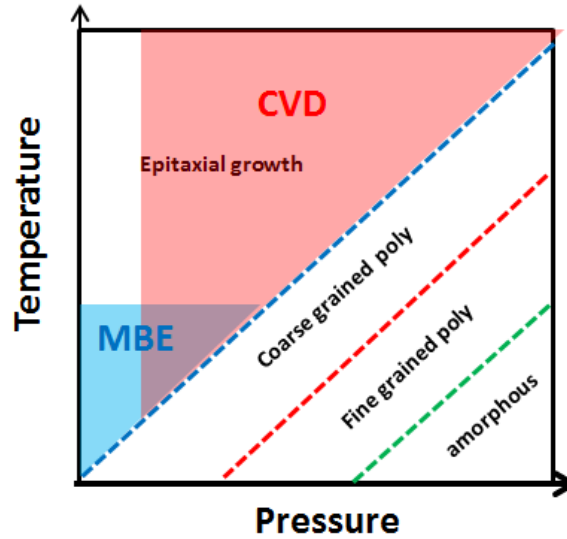


Figure 4 is a phase diagram for thin film growth structural regimes as a function of temperature and pressure. Classical epitaxy occurs in the high temperature-low pressure limit and the structural quality degrades as temperature is reduced and pressure is increased.

The illustration in figure 3 portrays the terraces as a flat-slabs however the atoms on the surface rearrange themselves in a way that some directions are preferred diffusion pathways and others are not. The altered energetic landscape of the surface creates preferred adsorption, diffusion, and incorporation sites. A detailed discussion of semiconductor surface reconstruction is beyond the scope of this work and only the basic concepts related to the Si/Ge (100) surface will be considered. The atoms of the Si/Ge surface are backbonded to two subsurface atoms and due to the tetrahedral nature of bonding they have two unsatisfied sp^3 orbitals which have one unpaired electron each. This unreconstructed surface is termed the Si/Ge (100) 1×1 and it is not energetically favored in most cases. To reduce the energy of the surface the atoms on the surface will rearrange themselves into rows of bonded dimers along the [110] directions such that each atom only has one unsatisfied bond. This causes bond strain but the energy gain due

to the strain is offset by the reduced number of dangling bonds. Troughs are formed in between the rows of dimers due to the displacement of silicon atoms to either side. It can be seen from figure 5 below that the displacement of the surface atoms away from their original positions creates local compressive and tensile strain in the troughs and dimers. This local strain influences preferred incorporation sites so that atoms larger than the host lattice will prefer tensile sites and atoms smaller than the host lattice will prefer compressive sites.

Once epitaxial growth is initiated how it proceeds is dependent on the lattice mismatch, $(a_{epi} - a_{sub})/a_{sub}$, and difference in surface energy, $\Delta\gamma$, between the epitaxial layers and the substrate. When $\gamma_{epi} < \gamma_{sub}$ and the lattice mismatch is minimal and growth proceeds by 2-dimensional step-flow, where the growth-front advances by adatom incorporation at step-ledges. Volmer-Weber growth occurs when $a_{epi} \sim a_{sub}$ and $\gamma_{epi} > \gamma_{sub}$;

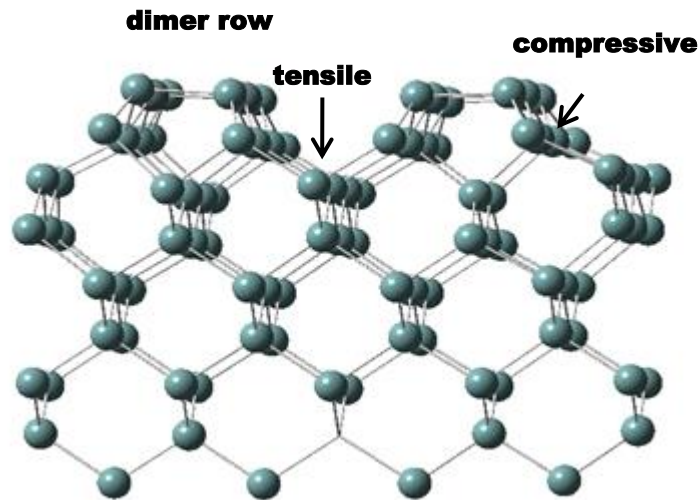


Figure 5 is an illustration of the reconstructed Si/Ge(100) surface viewed along the [110] direction. The displacement of Si surface atoms creates rows of dimers which are separated by troughs.

the strain energy is minimal however the interfacial energy mismatch causes islanding/dewetting during the initial stages of growth. The growth-front advances by adatom attachment to the islands until the separate islands coalesce and a continuous layer is formed at which point the growth-front proceeds vertically. When $a_{epi} > a_{sub}$ and $\gamma_{epi} < \gamma_{sub}$ it results in a third mode termed Stranski-Krastanov growth. In this mode an initial 2-dimensional growth is interrupted by the formation of interfacial dislocations and de-wetting of the surface. Strain-induced atomic migration is observed such that clusters of semiconductor pyramids/islands are surrounded by depleted regions. The growth-front advances by adatom attachment to the islands until the separate islands coalesce and a continuous layer is formed. Layers grown in this way are typically rough and very defective. The theory of epitaxial strain relaxation and defect formation is discussed in more detail in chapter 4.

Up to this point our discussion has been mainly relevant to the growth of elemental/binary semiconductor materials or equilibrium alloys. We have not considered how epitaxial dynamics change for the growth of meta-stable alloys. In certain cases there is a low solubility of the solute atom in a host lattice which can be driven by a mismatch in atomic size and/or bond energy. This condition will cause the solute atoms to segregate back to the surface after incorporation and once on the surface these solute atoms will seek to aggregate and form equilibrium secondary phases. Segregation physics are also discussed in more detail in chapter 4.

To prevent segregation and secondary-phase formation the growth conditions must be set far from equilibrium. Shifting the conditions away from equilibrium in simple

terms means that the rate of atomic/molecular transfer from the vapor phase to the surface is much greater than the rate at which the atoms on the surface can diffuse and incorporate. In our equilibrium model pictured in figure 4 we desired to maximize the mobility of the adatoms on the surface such that diffusion to the most energetically favorable positions could be achieved. For the meta-stable alloy the most energetically favorable configuration is agglomeration and phase-separation. We therefore choose conditions which kinetically frustrate atomic segregation and diffusion. Figure 6 below is an altered non-equilibrium growth phase diagram. Here we see that for successful epitaxial growth we move the growth conditions to high pressure and low temperature. The low temperature and high pressure limit the mobility of the solute atoms on the surface and limits their ability to exchange back to the surface after incorporation. MBE inherently must use very low pressure therefore it must use very low temperatures to kinetically limit the solute atoms. CVD on the other hand can access a higher range of pressure and therefore can still employ moderate temperatures for non-equilibrium growth. For meta-stable epitaxial growth CVD has two major advantages over MBE. The first advantage is the ability to grow meta-stable materials at moderate temperatures which likely reduces the crystal defect density. The second is that chemical reactions taking place on the surface effectively passivate sites which solute atoms may otherwise exchange to. This leads us to our discussion of CVD growth fundamentals.

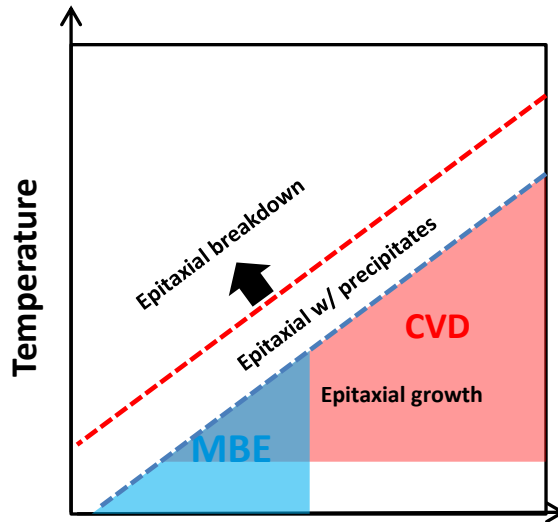
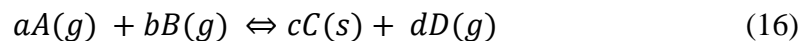


Figure 6 Phase diagram for the growth of meta-stable materials as a function of temperature and pressure. Single-phase epitaxial material is achieved in the low temperature-high pressure limit which is opposite of the conditions used for classical epitaxy.

CVD significantly complicates the models and mechanisms we have discussed up to this point. Chemical reactions occurring in the gas-phase (homogenous) and on the surface (heterogeneous) now influence the supply of adspecies to and from the surface. The removal of reaction byproducts from the surface often limits the continued adsorption of the reactants and in some cases the byproducts can introduce unwanted impurities in the epitaxial layer. The thermodynamics/energetics of the reaction are of the utmost importance in understanding the growth dynamics. Consider a general CVD reaction where a moles of A and b moles of B react to form a solid C and a gaseous byproduct D :



The Gibb's free energy of reaction, ΔG_r , qualifies the thermodynamic driving force for it to proceed. A negative value of ΔG_r indicates a favorable reaction:

$$\Delta G_r = \sum \Delta G(\text{products}) - \sum \Delta G(\text{reactants}) \quad (17)$$

Or alternatively:

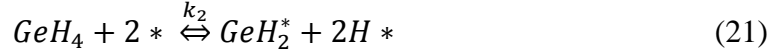
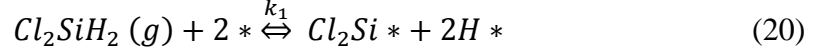
$$\Delta G_r = \Delta H_r - T\Delta S_r \quad (18)$$

where T is the temperature and ΔH_r and ΔS_r are the enthalpy and entropy of reaction, respectively. Tabulated values for standard enthalpies and entropies of formation are available for many of the gaseous precursors used in CVD. The equilibrium constant, K, is a more quantitative measure of the favorability of the forward reaction and is given by [35]:

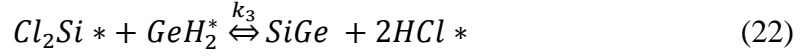
$$K = \frac{p_D^d}{p_A^a p_B^b} \quad (19)$$

where p_i are the partial pressures of the gaseous reactants and byproducts. In real CVD growth process there are often multiple parallel reaction pathways and these thermodynamic values can be used to predict those that are the most favored.

Although thermodynamics can predict the most favored reaction pathways often times kinetic limitations determine the reaction mechanisms. Surface adsorption reactions and subsequent reactions between adsorbates will have a rate constant, k_i , which has a Boltzmann-type relationship with an activation energy $E_{a,i}$. As an example we consider a simplified model the epitaxial growth of SiGe from H_2SiCl_2 and GeH_4 . The adsorption reactions are given by:



where * denotes a surface site/species. The surface reaction is given by:



Finally we have the desorption reactions:



The total rate constant is the sum of the individual rate constants:

$$k = k_1 k_2 k_3 k_4 k_5 \quad (25)$$

$$k = A_1 A_2 A_3 A_4 A_5 \exp\left(\frac{-E_{a,1} - E_{a,2} - E_{a,3} - E_{a,4} - E_{a,5}}{k_b T}\right) \quad (26)$$

The total activation energy is $E_a = \sum E_{a,i}$ and can be experimentally determined from the slope of an Arrhenius-type plot of growth rate on a log-scale vs. the reciprocal temperature.

At the higher pressure ranges (> 1 torr) typically used in CVD fluid flow considerations also become important. The flow of gaseous precursors through the reactor must be controlled to maximize the efficiency of the growth process. Laminar flow is desired over turbulent conditions to create a more homogenous distribution of reactants in the gas-stream. Additionally, frictional forces between the gas volume and the reactor walls (and substrate surface) cause boundary layer/stagnant layer formation.

Therefore reactants must diffuse through the boundary layer from the moving gas stream in order to reach the wafer surface. The thickness of this boundary layer, δ , is dependent on the gas velocity, v , the gas density, ρ , and the gas viscosity η as $\delta \sim \eta / v\rho$.

A concentration of reactants in gas stream, C_g , is different from the concentration of gases at the substrate surface, C_s . The flux of reactants to the surface can be expressed as:

$$F = h_g(C_g - C_s) \quad (27)$$

where h_g is the gas-phase diffusion coefficient. The flux which is consumed at the surface is given by $F_o = kC_s$, where k is the reaction rate constant from eq. 26. If we set $F_o = F$ for steady-state conditions then we can obtain the following expression for the concentration of reactant at the surface:

$$C_s = \frac{C_g}{1 + \frac{k}{h_g}} \quad (28)$$

This expression indicates that if $k \gg h_g$, then $C_s \rightarrow 0$. In CVD this is called the mass-transport limited regime and it is characterized by a weak growth rate dependence on temperature and strong dependence on precursor flow rate. This regime is usually encountered at high temperatures where the precursors react on the surface more quickly than they can be supplied from the gas-stream. The exact temperature at which this occurs will depend on the precursor and its activation energy barrier for reaction. The other limiting case is when if $k \ll h_g$ and $C_s \rightarrow C_g$. This condition is called the kinetically limited (or surface reaction rate limited) regime and it is characterized by an exponential

dependence of growth rate on temperature and a weak dependence of growth rate on precursor flow. This regime is encountered at lower temperatures and it results from the accumulation of reactants and their byproducts on the surface due to limitation in the available thermal energy. It is important to understand which regime the epitaxial growth will be occurring in when selecting precursor flow rates and temperatures. In circumstances where more than one precursor is used it may be the case that one precursor is mass-transport limited and the other is kinetically limited.

In reality epitaxial growth mechanisms can be incredibly complex and describing them with simple models may only give partial insight. Never the less an understanding of the simplified epitaxial growth models discussed in this section helps in planning experiments and interpreting results. It will be shown in later chapters that many of our results can be explained using the fundamental mechanisms of epitaxial growth described in this section.

2.2 EPITAXIAL GROWTH REACTOR

Epitaxial growth-runs were done on an ASM Epsilon® 2000 which is a commercially available CVD tool designed for high volume semiconductor manufacturing. Wafer cassettes can be loaded into dual load-locks on the front end of the tool and stored in an inert environment while awaiting processing. The load locks are each N₂ purged and connected to a vacuum pump which is capable of bringing each load lock to a base-pressure of 100 mTorr. After loading wafers, the load locks are pumped to base-pressure and then purged in N₂ multiple times in order to reduce the moisture and O₂ level.

Connected to the front-end load locks is a wafer handling chamber which houses a robot that moves wafers between the load locks and the deposition chamber. The wafer handling chamber is continuously purged with N_2 and is also equipped with a vacuum pump which is capable of achieving a base pressure of 1 Torr. Great care must be taken to ensure either residual H_2O or O_2 is not transferred into the processing chamber. The wafer handling chamber is made of Ni-plated billeted aluminum for optimum moisture control. It is further equipped with a laser spectrometer for monitoring the moisture content with the specification that $p_{H_2O} < 10$ ppb. After completion of the pump-purge cycles wafers are assigned a growth recipe in a graphical user interface (the contents of a typical growth recipe will be discussed later). Figure 7 below is a cut-away sketch of the Epsilon® 2000 showing the three main components of the tool; the front-end load locks, wafer handling chamber, and reactor. Each unit is separated by gate-valves allowing isolation at all times except during wafer transfer.

When a wafer is selected for processing the gate-valve separating the load lock and the wafer handling chamber is opened and the transfer arm removes the wafer from the cassette and moves it into the wafer transfer chamber. The transfer arm is made of high purity quartz and is based on the Bernoulli-effect. Gas flow channels are formed in the arm and N_2 gas is directed through them which creates a vacuum between the wafer surface and the arm, and thus enables the arm to pick-up (gas on) and put-down (gas off) the wafer. The gate valve separating the deposition chamber from the wafer handling chamber is then opened so that transfer arm can place the wafer on the susceptor for processing.

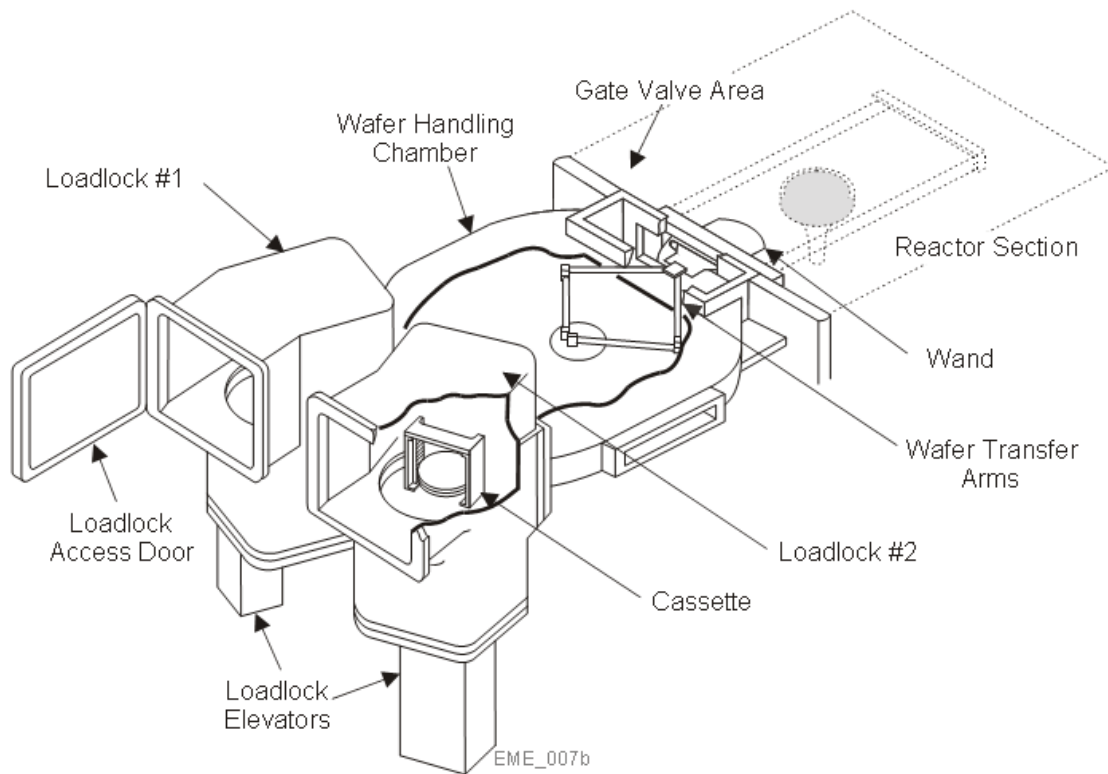


Figure 7 A cross-section of an Epsilon® 2000 highlighting the front-end wafer load-locks and wafer handling chamber.

The last and most important part of the tool is reactor/deposition chamber illustrated in figure 8 below. The chamber is made of high-purity ribbed quartz, the ribs structurally reinforce the chamber to prevent an implosion at reduced pressure. The wafer sits on graphite susceptor which is coated with SiC for improved chemical stability and lifetime. This susceptor is rotated by a ferrofluidic assembly underneath the chamber which greatly improves the deposition uniformity. Deposition and gases are injected from a manifold at the front-end of the chamber and are pumped out of the exhaust at the rear which creates a laminar flow across the wafer surface with no gas recirculation. The

manifold is equipped with five separate gas injector ports which can be individually controlled to bias the deposition gas flow to varying sides of the wafer. This can be used to tune the deposition profiles across the wafer in the mass-transfer limited growth regime.

The reactor is heated by two linear lamp-bank arrays on the top and bottom of the susceptor and the inside of the chamber is coated with gold maximize the radiant efficiency. There are 9 linear lamps on the top array and 8 linear lamps on the bottom array which can be individually addressed to adjust the temperature uniformity across the wafer/susceptor. The temperature is monitored by three thermocouples which are located in the center and on the left and right sides of the susceptor. The temperature measured at the thermocouples is actively controlled relative to the set-point with a PID-driven power supply.

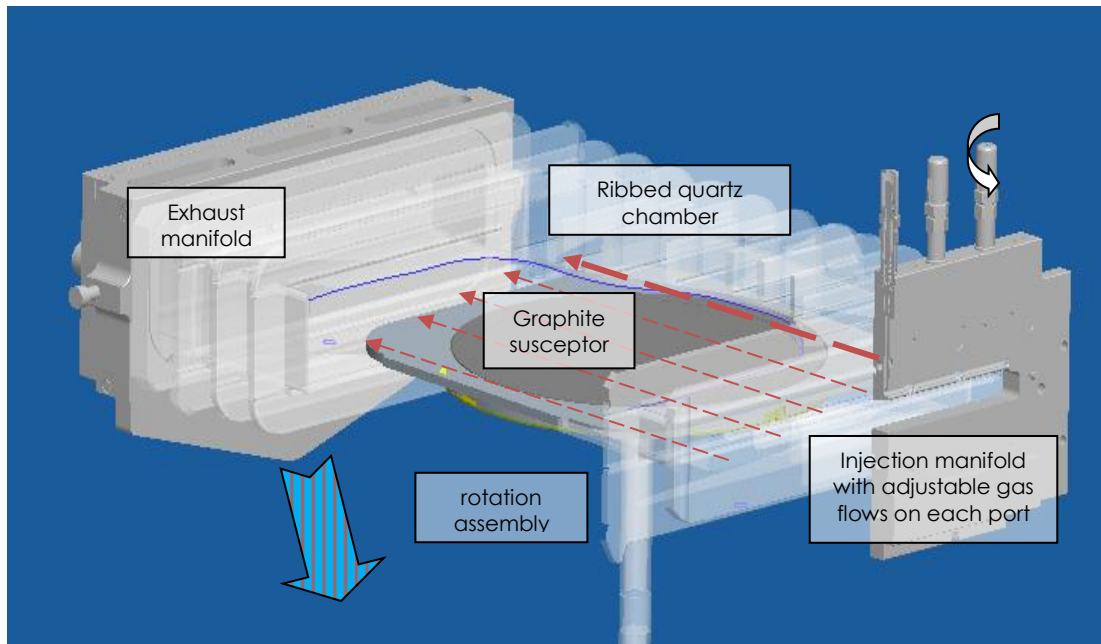


Figure 8 Cut-away drawing of the deposition chamber. The injection manifold (far-right) has five ports of which three are shown

The SnCl_4 was delivered using a bubbler vessel held at 20°C in which H_2 gas is metered to it to increase or decrease to the desired SnCl_4 mass flow rate. The vapor pressure of the SnCl_4 at this temperature is ~ 20 torr. The SnCl_4 mass flow rate is measured up-stream of the bubbler by a piezoelectric acoustic sensor. This signal is fed back to a H_2 mass flow controller, upstream of the bubbler, in a dynamic control loop to continually monitor and adjust the SnCl_4 relative to the desired set-point. GeH_4 , SiH_4 , and dopant gas flows such as B_2H_6 , PH_3 , and AsH_3 are controlled by mass flow controllers (MFC's) located in the tool gas-cabinet. The gas flow can be directed either to the reactor ("run") or to the exhaust ("vent") such that pressure and flow transients can be avoided which enables greater interfacial control at the wafer surface. When directed to the reactor the gases are injected through the aforementioned five-port injection manifold.

2.3. GERMANIUM BUFFER LAYER GROWTH

All GeSn and SiGeSn epitaxial growth was done on Ge-buffered silicon wafers. A low defect buffer layer is necessary to produce quality epitaxial layers. In diamond structured group IV semiconductors dislocation motion occurs along $\{111\}$ planes in the $\langle 110 \rangle$ direction which are at 60° relative to the layer substrate interface. These dislocations on the growth surface can readily thread through the epitaxial layer during layer growth. The growth of Ge on Si proceeds via a Stranski–Krastanov mechanism in which an initial ~ 3 continuous monolayers form followed by the formation of islands. There have been several approaches demonstrated that circumvent this growth behavior. We chose to adopt a two-step growth process similar to that proposed by Luan et al. to avoid island formation during the initial stages of growth

[36]. Germanium buffer layers (approximately 700 nm thick) were grown *in-situ* prior to GeSn growth using 10% GeH₄ in purified H₂ carrier gas. Prior to growth of the Ge buffer layer the silicon substrate is heated to 1060°C at 20 torr to remove the native oxide. The buffer layers were grown by a two-step growth method. First, a 150 nm seed layer was grown at < 400°C in H₂ carrier at a GeH₄ partial pressure of 0.2 Torr, then the temperature was increased to 600°C. Once the temperature has stabilized at 600°C, the remaining ~ 500 nm was grown and a post-growth *in-situ* anneal was done at > 800°C. In this process the initial growth is conducted at low temperatures < 400°C to extend the 2-D growth followed by a high temperature > 600°C growth in which the bulk of the film is deposited. The higher temperature growth reduces the dislocation by promoting glide and subsequent annihilation of threading defects as well as providing an increased growth rate. Further defect reduction is accomplished by *in-situ* annealing of the layers at 850°C. The annealing can be done in cyclical stages of growth and annealing or can be accomplished as one final post-growth anneal. The anneal conditions were optimized by comparing the FWHM of Ge-buffer XRD ω -scans between conditions. The FWHM value is a measure the distribution of in-plane lattice constants probed in the layer, a larger distribution would indicate the presence of more misfit dislocations and result in a wider FWHM. Ayers et al showed that the threading dislocation density TDD can be correlated to the FWHM, β , by $TDD = \beta^2 / 4.36b^2$ where b is the burgers vector [37]. The annealing temperature and buffer-layer thickness were fixed and only the times and cycles were varied. The annealing conditions and the resulting XRD ω -scan FWHM are shown in table 1 below. The

deposited baseline condition is used as a reference for the degree of crystal quality improvement. Cyclic annealing adds an additional temperature ramp, and cool-down time to the growth recipe. This negatively impacts throughput which must be considered for high-volume manufacturing processes. Cyclic annealing was found to be quite effective in improving the crystal quality however single post-growth annealing with increased soak time was found to be equally effective without such a negative impact on throughput. Therefore condition (3) was selected for this process. Utilizing this approach relaxed Ge buffer layers with thicknesses of ~ 700 nm can be grown with threading defect densities of $\sim 1 \times 10^8 \text{ cm}^{-2}$. Defect densities of $\sim 1 \times 10^7 \text{ cm}^{-2}$ were achieved by extending the layer thickness to greater than 1500 nm however we limit our discussion to the thinner Ge-buffer layers in the interest of manufacturability.

Etch-pit density (EPD) measurements were close to the XRD defect densities. Figure 9 shows a typical AFM image of the etched Ge-buffer surface. The etch pit density in this figure is $8 \times 10^7 \text{ cm}^{-2}$ which is slightly lower than the XRD measured value of $1 \times 10^8 \text{ cm}^{-2}$. This is expected because the EPD measurement is much more representative of the surface, whereas XRD value is more representative of the bulk defect values. A typical XRD lattice space map of the (224) Bragg reflection for a 700 nm thick buffer is shown in Figure 10. As can be seen in the figure the ellipsoid corresponding to the Ge epilayer lies above the dashed line which represents the position of a fully relaxed layer indicating that the Ge is under a slight tensile strain of 0.26% with $a = 5.6725 \text{ \AA}$, $c = 5.6463 \text{ \AA}$. This residual strain is associated with the

difference in the coefficient of thermal expansion between the Ge epilayer and the Si substrate during cooldown.

Table 1 Summary of Ge buffer layer annealing

Annealing condition	XRD ω -scan FWHM (arc sec)	Estimated defect density (cm^{-2})
Baseline (no anneal)	357	1.4×10^{10}
One post-growth 30 second anneal at 850°C	220	5.3×10^9
One post-growth 180 second anneal at 850°C	178	1.1×10^8
Two 30 second anneal cycles at 850°C	181	1.1×10^8
Two 180 second anneal cycles at 850°C	180	1.1×10^8

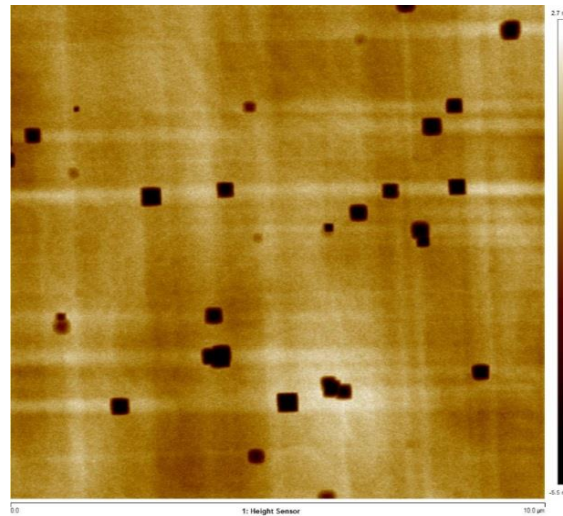


Figure 9 A 10 x 10 μm AFM scan of a relaxed Ge-buffer which was then HCl etched in-situ so that the defects (etch-pits) can be decorated and counted.

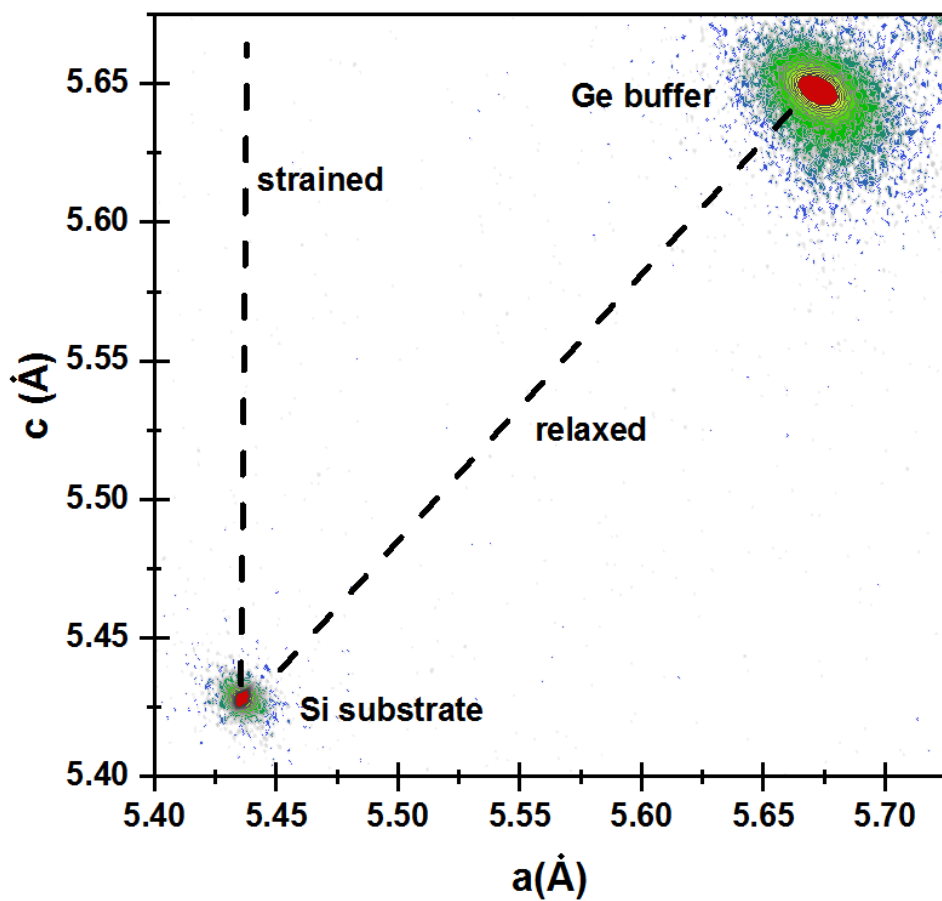


Figure 10 XRD lattice space map which from the FWHM of the Ge peak has a TDD $\sim 1 \times 10^8 \text{ cm}^{-2}$

CHAPTER 3

GE_{1-x}SN_x LAYER GROWTH

Prior to this work CVD growth of epitaxial GeSn relied on either UHV and SnD₄ approaches or Ge₂H₆ and SnCl₄. The use of GeH₄ is attractive for high volume manufacturing perspective mainly for reasons of cost and infrastructure. The considerations which went into the development of this process were a.) pressure b.) temperature c.) flow ratio. For metastable materials such as GeSn we desire growth conditions which are far from thermodynamic equilibrium. We start with a pure-Ge growth process at low temperature and then add small amounts of SnCl₄ to the chemistry to achieve dilute GeSn layers. Bearing in-mind the requirement for non-equilibrium growth conditions we initially investigated the temperature range of 275-400°C. In this range GeH₄-based growth rates are expected to be 5-10 nm/min so we utilize high GeH₄ partial pressures of 1-4 Torr and SnCl₄ flow rates ranged from 1-4 x 10⁻⁵ mol/min. In our initial screening we also evaluate the effect of the carrier gas; both H₂ and N₂.

In this chapter we discuss the how the process conditions affect the growth rate, Sn composition and morphology. We find that there are narrow windows for temperature, pressure, and flows in which single crystal GeSn can be realized. The understanding gained by studying the fundamentals of the growth chemistry and kinetics is a foundation for more advanced structures. For growth of GeSn on Ge we are able to demonstrate GeSn layers with Sn contents form 1-12% which all show room temperature photoluminescence.

3.1 GE_{1-x}SN_x GROWTH KINETICS

3.1.1. PRECURSOR FLOW EFFECTS

In figure 4 below the growth rate of pure Ge and GeSn is plotted as a function of SnCl₄ molar flow fraction (SnCl₄/GeH₄) at 350°C and a fixed $p_{\text{GeH}_4} = 2$ Torr. We observe an initial decrease in the growth rate at low flow which we attribute to an etching component of the chemistry. The reaction and decomposition of SnCl₄ or SnCl₄-intermediates should generate Cl* species on the growth surface which can have an etching effect from the desorption of GeCl₂ and SnCl₂ [38,39]. Therefore, in order to achieve GeSn growth the etching rate has to be less than the deposition rate of the film. The growth rates for N₂ carrier are consistently higher than those with H₂ carrier which is expected due to decreased H coverage on the growth surface. The growth rate for pure Ge in N₂ carrier is 16 nm/min and it decreases to 8.1 nm/min at the lowest SnCl₄ flow due to etching. Pure Ge in H₂ carrier gas has a growth rate of 9.9 nm/min and decreases to 6.3 nm/min for the lowest SnCl₄ flow. This is a 2x decrease in growth rate for the N₂ carrier and only a 1.6x decrease for the H₂ carrier for the same increase in SnCl₄ flow. For the same reasons that N₂ carrier results in increased growth rate it can also result in an increased etch rate, less H coverage on the growth surface allows for more Cl coverage and subsequent GeCl₂/SnCl₂ desorption.

An increase in growth rate was observed for $\text{SnCl}_4/\text{GeH}_4 > 1.7 \times 10^{-5}$ in both H₂ and N₂ the slopes appear very similar. The etching component is balanced by an apparent catalytic component at higher SnCl₄/GeH₄ conditions. This is likely due to the facile H and Cl desorption from Sn surface sites relative to Ge surface sites. When SnCl₄/GeH₄ is

increased the surface becomes more Sn-rich, and the Sn-Cl and Sn-H bonds are weaker (3.3 eV and 2.6 eV respectively) than the Ge-Cl and Ge-H bonds (3.6 eV and 3.0 eV). We therefore, expect an increase in the H and Cl desorption rate and thus higher growth rate as the Sn fraction on the surface increases [39].

These phenomena are further explored in figure 11 where the growth rate is plotted vs. $\text{SnCl}_4/\text{GeH}_4$ over a larger flow ratio range and for a second temperature of $T = 320^\circ\text{C}$. We see that Sn incorporation is higher for the 320°C relative to the 350°C which is not intuitive based on disassociation energies of the precursors involved. For the reaction $\text{SnCl}_4 \rightarrow \text{SnCl}_2 + \text{Cl}_2$, $\Delta H_r = 362 \text{ kJ/mol}$ [40,41] while for the reaction GeH_4

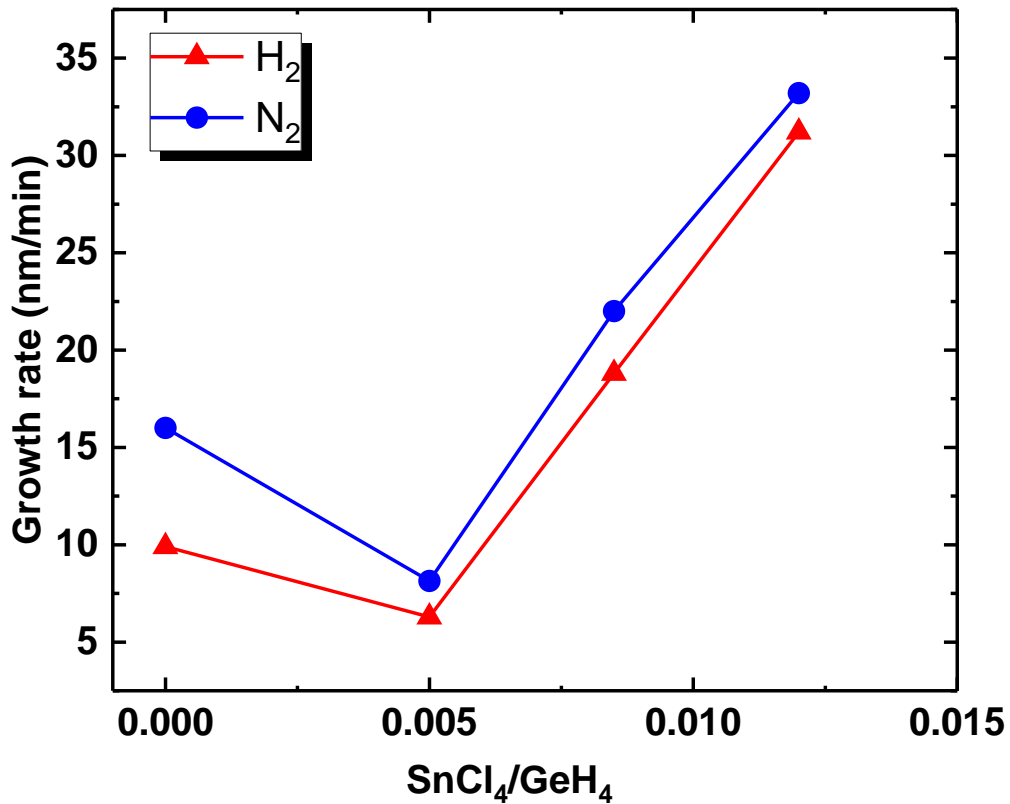


Figure 11 Growth rate of Ge and GeSn as a function of the molar flow fraction at $T = 350^\circ\text{C}$ and a fixed $p_{\text{GeH}_4} = 2 \text{ Torr}$. There is an initial decrease in the growth rate, which is due to etching, followed by a strong increase at higher SnCl_4 flow.

→ GeH₂ + H₂, ΔH_r = 235 kJ/mol [42]. Due to the greater disassociation energy of the SnCl₄ molecule its reactivity should be lower than that of GeH₄ as the temperature is decreased and lower Sn incorporation would be observed. We delay a detailed discussion of temperatures effects until the next section.

In figure 12 the improvement in growth rate in switching from H₂ to N₂ reduces with increasing SnCl₄/GeH₄ and lower temperature. This is not surprising given that the surface will become increasingly covered by Cl in both instances such that the surface sites that would have been open by removing H₂ carrier gas are now covered by Cl. Growth at the higher temperature shows a linear increase in GR with SnCl₄/GeH₄ whereas growth at the lower temperature is sub-linear. At 350°C the Cl desorption is more efficient and as SnCl₄/GeH₄ is increased the balance between Cl coverage and desorption is maintained. However at 320°C the balance between coverage and desorption is not as well maintained and the growth rate begins to decrease at higher

SnCl₄/GeH₄. A rough Boltzmann-like approximation $\left(\frac{\exp(-x_{Sn}\Delta G_{Sn-cl}+(1-x_{Sn})\Delta G_{Ge-cl}/k_bT_2)}{\exp(-x_{Sn}\Delta G_{Sn-cl}+(1-x_{Sn})\Delta G_{Ge-cl}/k_bT_1)}\right)$ using our values for Ge-Cl (3.6 eV) and Sn-Cl (3.3 eV) bond energies indicates a ~ 50x increase in Cl desorption rates between 320°C and 350°C for a 5% Sn layer.

The Sn concentration is only weakly dependent on the SnCl₄ flow. From figure 13 we also see that the Sn content does not increase linearly with increasing SnCl₄/GeH₄ but rather increases as a power law type function i.e. $[SnCl_4/GeH_4]^n$. This type of behavior is common in other group IV alloy CVD growth using mixed hydride/chloride chemistries [43, 44] and indicates unequal reaction orders for GeH₄ and SnCl₄. We can separately

consider the growth rate components for Ge and Sn which are given by:

$$R_{Ge} = \frac{s_{GeH_4}[GeH_4]N_a\theta^m}{N} \quad (29)$$

$$R_{Sn} = \frac{s_{SnCl_4}[SnCl_4]N_a\theta^n}{N} \quad (30)$$

Where s_{GeH_4} and s_{SnCl_4} are the precursor reactive sticking coefficients, N is the surface site density, N_a is Avagadro's number, θ is the vacant surface site coverage, and m and n are the respective adsorption reaction orders. The value of n and m therefore indicate the mechanism of adsorption and how many open surface sites are preferred. We can see from taking the ratio of eq's 3 and 4:

$$\frac{R_{Sn}}{R_{Ge}} = \frac{s_{SnCl_4}[SnCl_4]}{s_{GeH_4}[GeH_4]} \theta^{n-m} \quad (40)$$

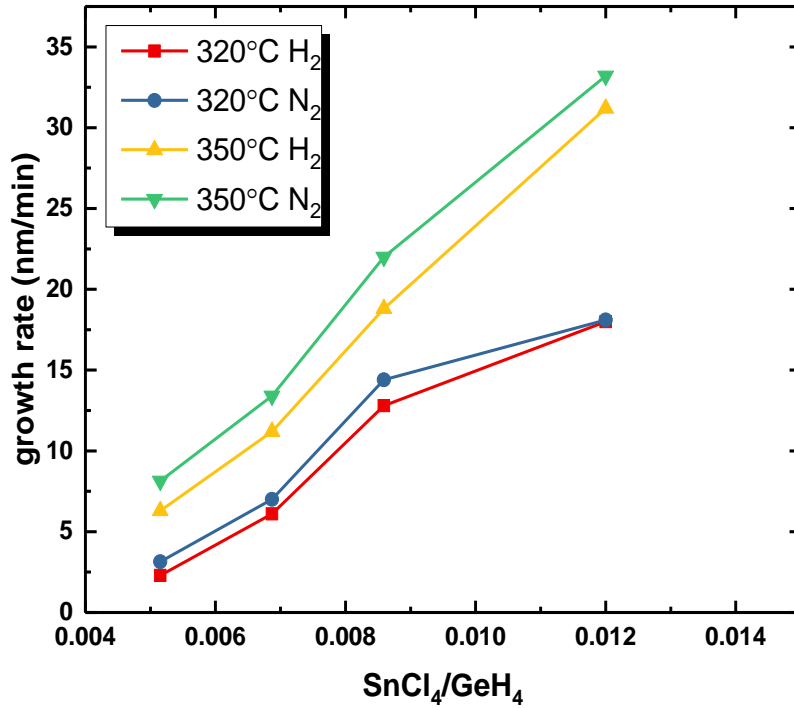


Figure 12 Plots the growth rate vs. SnCl₄/GeH₄ for two temperatures and both types of carrier gas

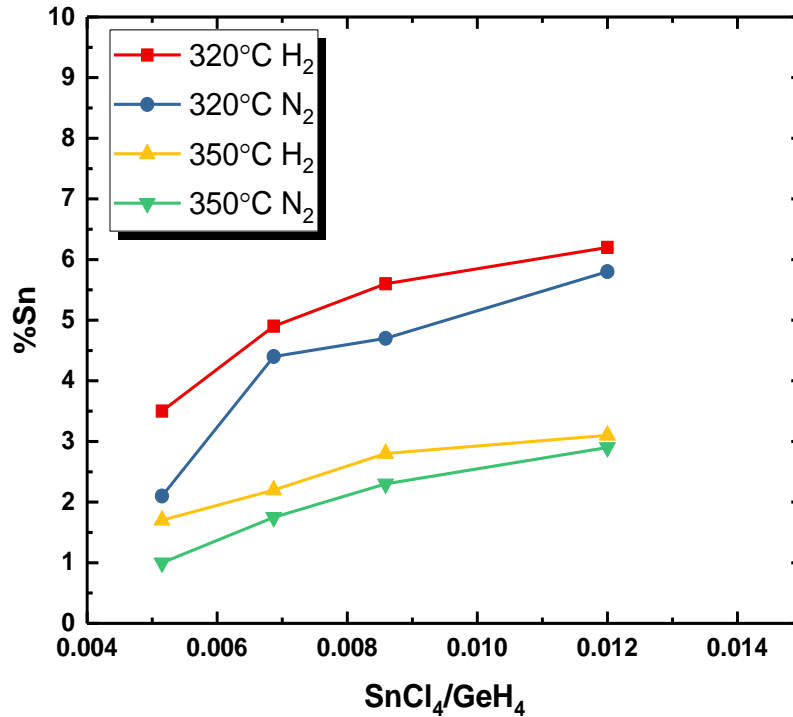


Figure 13 Plots the %Sn vs. SnCl₄/GeH₄ for two temperatures and both types of carrier gas.

that when the reaction orders are equal, $m - n = 0$, and we expect a linear dependence between % Sn and SnCl₄/GeH₄. However the observed power law dependence of $n < m$ indicates the reaction order for GeH₄ is higher than that of SnCl₄. Thus at higher SnCl₄/GeH₄ Ge atoms incorporate more easily than Sn atoms. The reasons for this are both kinetic and thermodynamic and will become clearer when the chemistry is discussed but stated simply here; an increase in open site density θ will increase GeH₄ adsorption exponentially while only increasing SnCl₄ linearly.

The sticking coefficients are coverage dependent and reflect how efficiently the precursors adsorb and stay adsorbed. Experimental determination of the coverage-dependent sticking coefficient is difficult in practice. However the relative efficiency of

each precursor can be measured by considering the input molecular flow rates of each precursor, and based on the final composition and film-volume, calculating the fraction of precursor which was incorporated. In figure 14 the incorporation fraction is plotted for SnCl₄ and GeH₄ in both H₂ and N₂ as a function of the molar flow rate. It can be seen that Sn incorporation is ~ 10x more efficient than Ge and that both incorporate more efficiently as the SnCl₄ molar flow rate increases. It is suspected that not only do Sn atoms on the surface allow more open sites, but gas-phase reactions between SnCl₄ and GeH₄ generate more reactive intermediates thereby increasing the efficiency. We will return to this discussion in section 3.1.4 when we discuss the chemical reactions involved in growth. However of primary interest in figure 14 is the comparison of precursor efficiencies in H₂ and N₂. We note that Sn incorporation efficiency is higher for H₂ carrier gas where Ge incorporation is improved by N₂ carrier gas. This again suggests that the GeH₄ incorporation efficiency being limited by the open site density, θ , whereas the SnCl₄ incorporation efficiency is not as sensitive to θ and is most likely reacting in the gas phase to produce a reactive intermediate species. Figure 15 compares the precursor efficiencies at 320°C and 350°C and we see a significant improvement in the Ge incorporation efficiency and decrease in that of Sn. Based solely on the input precursor bond energy it is expected that higher temperature should assist in Sn incorporation due to the stronger Sn-Cl bond relative to the Ge-H bond.

. The effective reaction order of $n - m$ can be estimated by borrowing from the model proposed by Suh and Lee [43] where the ratio of Sn to Ge is related to [SnCl₄]/[GeH₄] by:

$$\frac{x_{Sn}^{1+q}}{1-x_{Sn}} = \left(\frac{[SnCl_4]}{[GeH_4]} \right)^{n-m=\beta} \quad (41)$$

where q can take values between 0 and 1. This reflects the extent to which competing Cl desorption steps are active, a value of $q = 0$ indicates direct Cl desorption from surface

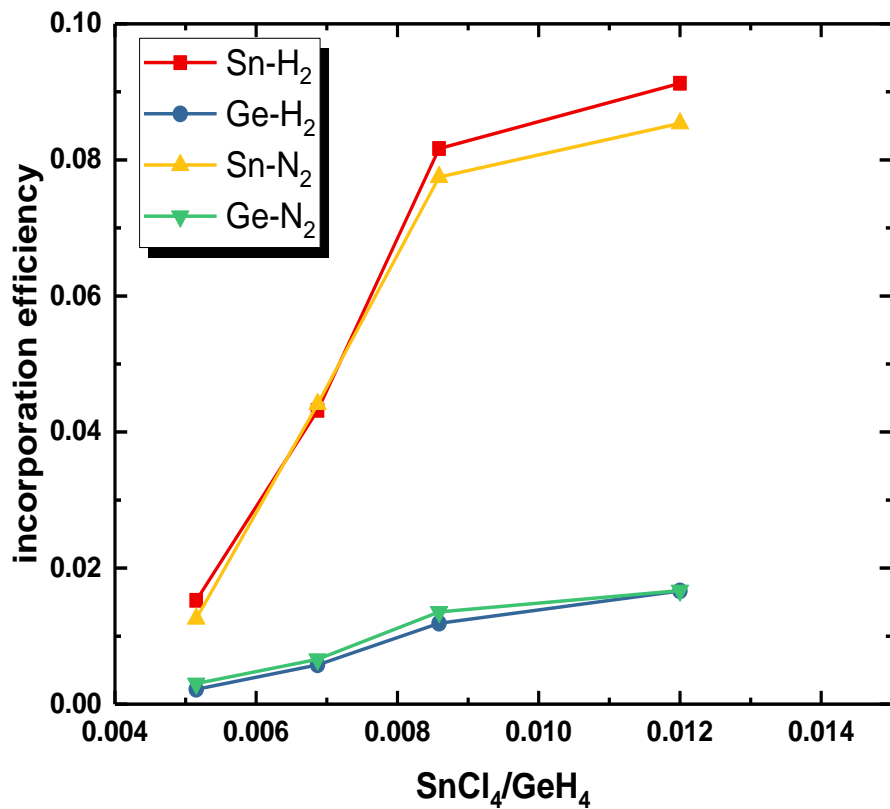


Figure 14 Plots the fraction of precursor incorporated vs. the SnCl₄/GeH₄ molar flow ratio in both carrier gases at a fixed temperature.

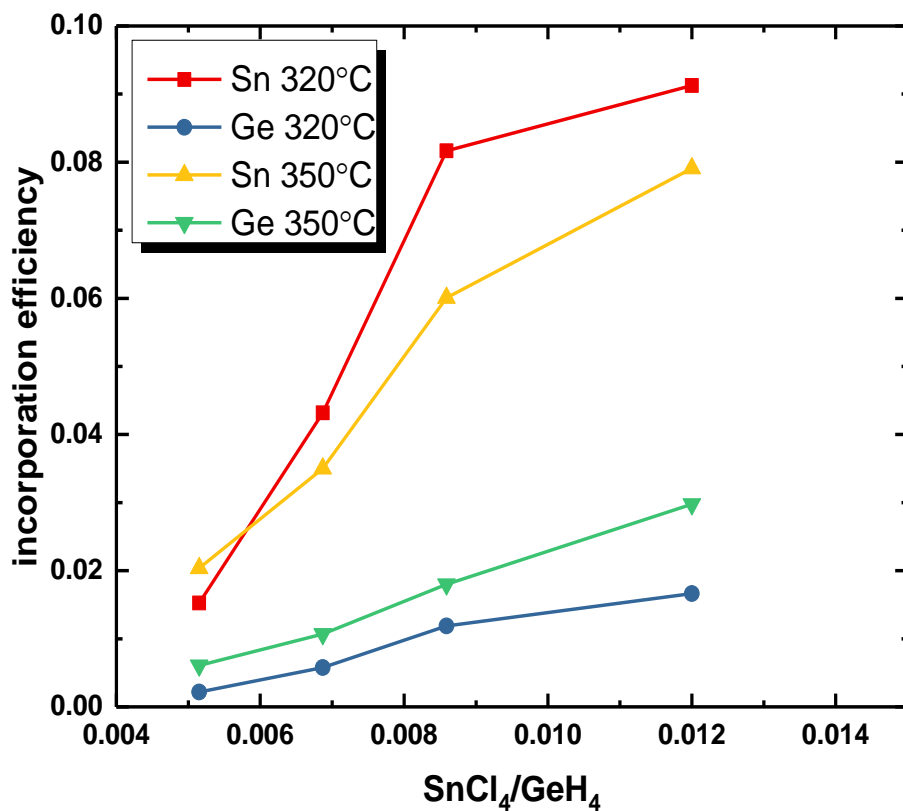


Figure 15 Plots the fraction of precursor incorporated vs. the SnCl₄/GeH₄ molar flow ratio in H₂ carrier gas at two different temperatures.

Ge and $q = 1$ indicates Cl migration to neighboring Sn before desorption [43]. In figure 16 we have plotted $x_{Sn}^{1+q}/(1 - x_{Sn})$ vs. $M[SnCl_4]/M[GeH_4]$ on a log-log scale such that the slope of the fitted line = β , which is the overall reaction order. The linear fits were better for $q = 1$ than $q = 0$ (not shown) suggesting that two-step Cl desorption is dominant. A linear fit of the lines in figure 16 yields the power exponent, β , for each condition: $\beta(T_1, H_2) = 0.41$, $\beta(T_1, N_2) = 0.46$, $\beta(T_2, H_2) = 0.10$, and $\beta(T_2, N_2) = 0.11$. There is a larger difference in the power exponent observed when changing temperatures than when switching carrier gases at the same temperature. This may be a result of the rate limiting step being Cl-desorption at low temperature and precursor adsorption the rate limiting

step at higher temperature. Reaction mechanisms are discussed in more detail in the next section.

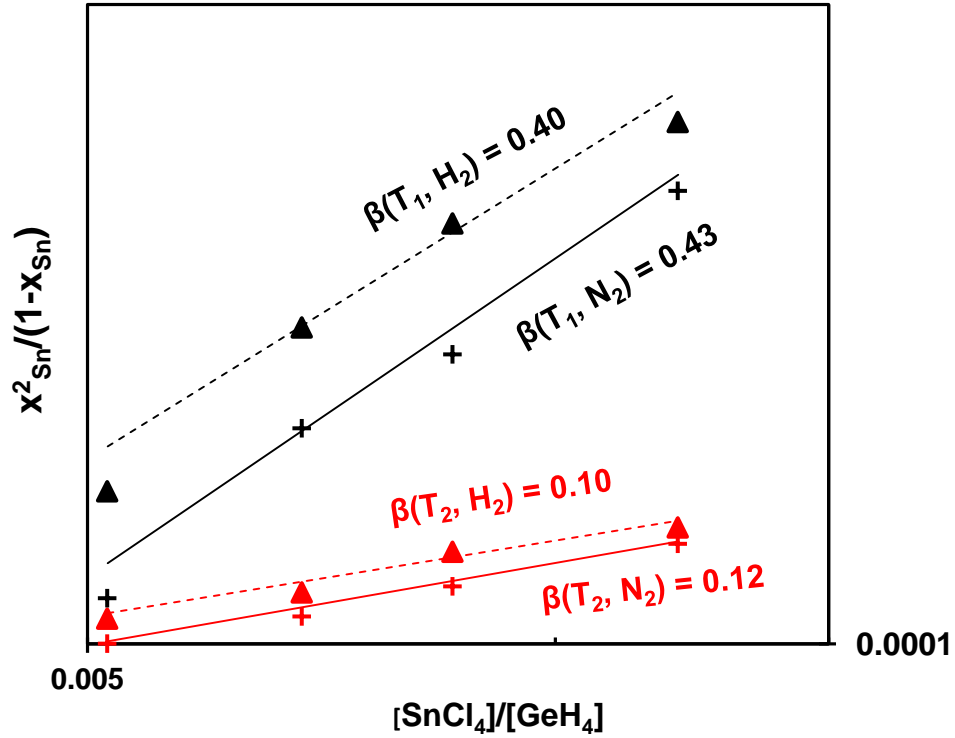


Figure 16 Log-log plot of $x_{Sn}^{1+q}/(1-x_{Sn})$ vs. $M[SnCl_4]/M[GeH_4]$. The slope(s) of the linear fit(s) should indicate the overall reaction order for GeSn growth via $GeH_4 + SnCl_4$ in H_2 and N_2 .

3.1.2. TEMPERATURE EFFECTS

The growth rate for GeSn varies between 8 nm/min, at the lowest growth temperatures, to 45 nm/min at the highest. Figures 17 and 18 are Arrhenius plots for the total growth rate, Ge-component of the growth rate, and Sn-component of the growth rate for $SnCl_4/GeH_4 = 0.0085$ and 0.012. The total activation energy for the lower flow ratio is $E_a = 0.36$ eV and for the higher flow ratio $E_a = 0.52$ eV. The higher activation energy at

higher flow ratio is due to the increased surface reaction and coverage and the requirement to remove those reaction byproducts to continue growth. The kinetic constants for each condition can be described as $k_1 = 10^{9.56} \cdot \exp\left(\frac{-0.36}{k_b T}\right)$ and $k_2 = 10^{13.1} \cdot \exp\left(\frac{-0.52}{k_b T}\right)$ [42]. The Ge and components of the activation energy are $E_{a,Ge} = 0.39$ eV and 0.55 eV for the low and high flow ratios respectively. In both cases this is a ~ 0.03 eV increase from the total E_a and if we consider that $E_a = E_{a,Ge} + E_{a,Sn}$ than we must again conclude that the presence of Sn on the surface decreases the total activation energy for deposition. The Sn component of the growth rate is also shown in figures 17 and 18 and we see an inverse dependence on T or a negative activation energy. Extraction of this value from the slope of the line is not valid however as the final Sn composition measured in the layer is not only a function of surface reaction energetics but also post-surface-reaction segregation/out-diffusion. As the temperature is increased Sn surface segregation is enabled and these Sn atoms can be etched and removed from the surface as $SnCl_x$ (g). Therefore the value of 0.03 eV from above is probably closer to reality. Despite the uncertainty in the precise Arrhenius behavior of Sn incorporation it is qualitatively apparent that the Sn-component of the growth is not thermally activated. This implies that the Sn-precursor is already partially decomposed and reactive by the time it reaches the growth surface. However this is not intuitive again considering the decomposition enthalpies; $SnCl_4 \rightarrow SnCl_2 + Cl_2$, $\Delta H_r = 362$ kJ/mol and $GeH_4 \rightarrow GeH_2 + H_2$, $\Delta H_r = 235$ kJ/mol.

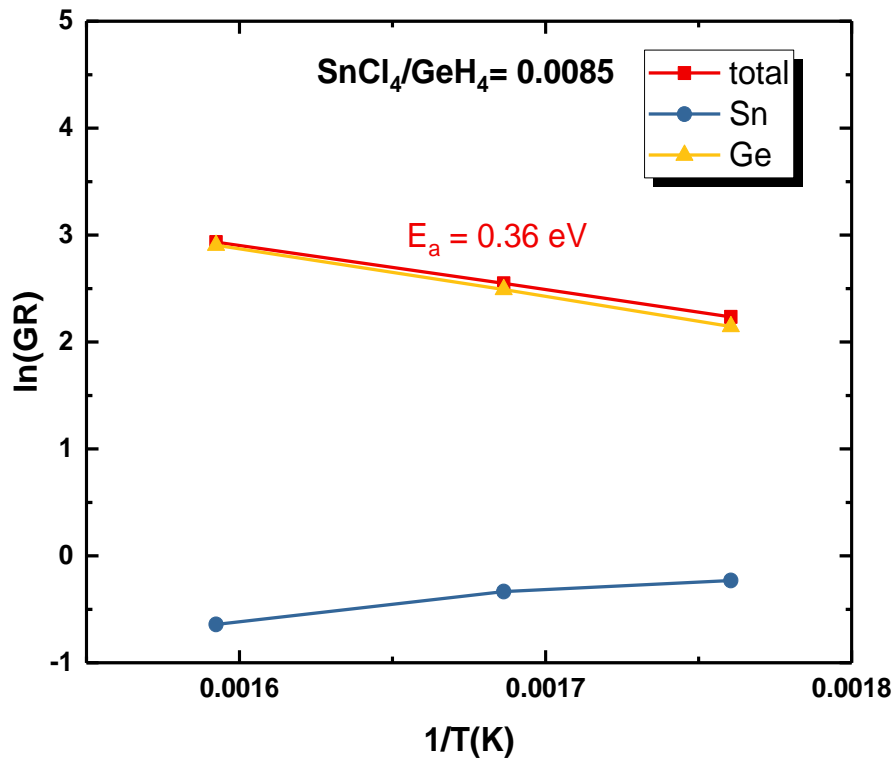


Figure 17 Arrhenius plot for the Ge, Sn, component and total growth rates with the total activation energy shown for $\text{SnCl}_4/\text{GeH}_4 = 0.0085$.

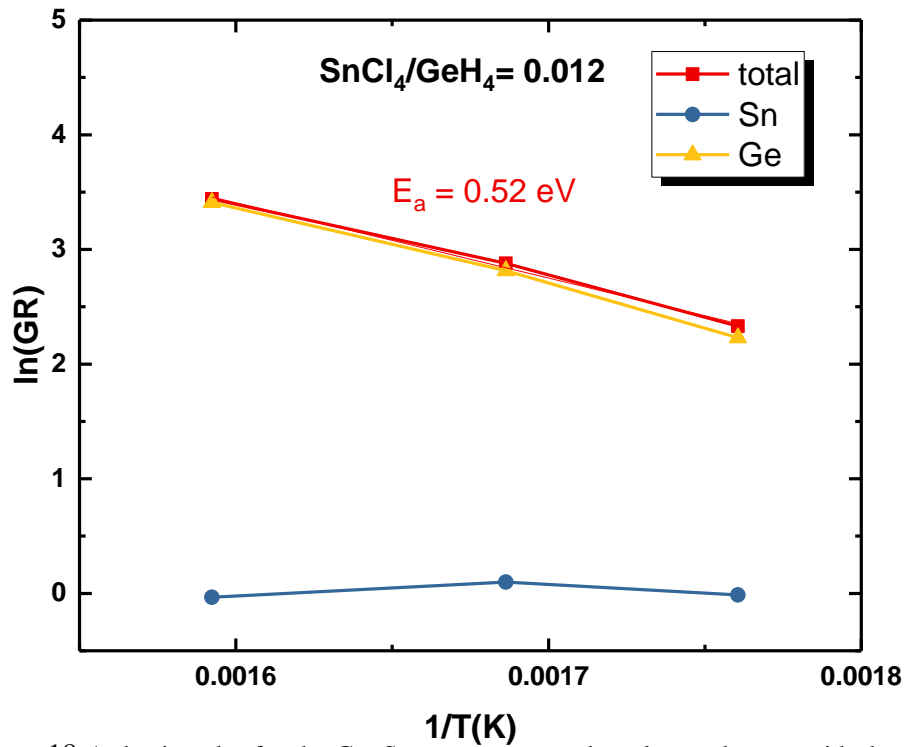


Figure 18 Arrhenius plot for the Ge, Sn, component and total growth rates with the total activation energy shown for $\text{SnCl}_4/\text{GeH}_4 = 0.0012$.

There is a $\sim 120^\circ\text{C}$ temperature window in which GeSn can be grown and within this window the Sn composition is highly sensitive to temperature changes. In figure 8 the % Sn is plotted vs. temperature for $\text{SnCl}_4/\text{GeH}_4 = 0.0085$ and 0.012 and it is seen that there is a $\sim 1\%$ Sn increase for every 10°C temperature decrease. At the highest end of the range, $T > 400^\circ\text{C}$, the Sn concentration becomes very dilute and is no longer an alloy but only a Ge layer doped with Sn. As the temperature is decreased Sn segregation is kinetically frustrated and the GeH_4 reactivity decreases which results in an increase in Sn composition. However at the lowest end of the temperature window growth completely ceases. This is curious because it implies that at a temperature of $\sim 280^\circ\text{C}$ both precursors suddenly lose their reactivity. It is known that below 285°C GeH_4 does not disassociatively adsorb [42] which may hint that either the GeH_2 and/or the 2H generated during the adsorption reaction are required to reduce SnCl_x fragments on the surface. A comparison of the temperature dependences for GeH_4 and Ge_2H_6 also supports this idea. Figure 9 shows the Sn incorporations as functions of temperature using GeH_4 and Ge_2H_6 for the same flow conditions, $\text{SnCl}_4/\text{GeH}_4 = \text{SnCl}_4/\text{Ge}_2\text{H}_6$. There has not yet been a direct comparison of these two precursors for the purpose of GeSn growth. Growth in GeH_4 results in a drastic decrease in Sn incorporation at $\sim 285^\circ\text{C}$ whereas the low temperature growth limit for using Ge_2H_6 is $\sim 15^\circ\text{C}$ lower than that of using GeH_4 . This is because the reactivity of Ge_2H_6 is greater than that of GeH_4 and a lower growth temperature capability is expected for Ge_2H_6 . However, if the limiting factor was only the reactivity of Ge-hydrides then an increase in Sn incorporation as the efficiency of the Ge precursor

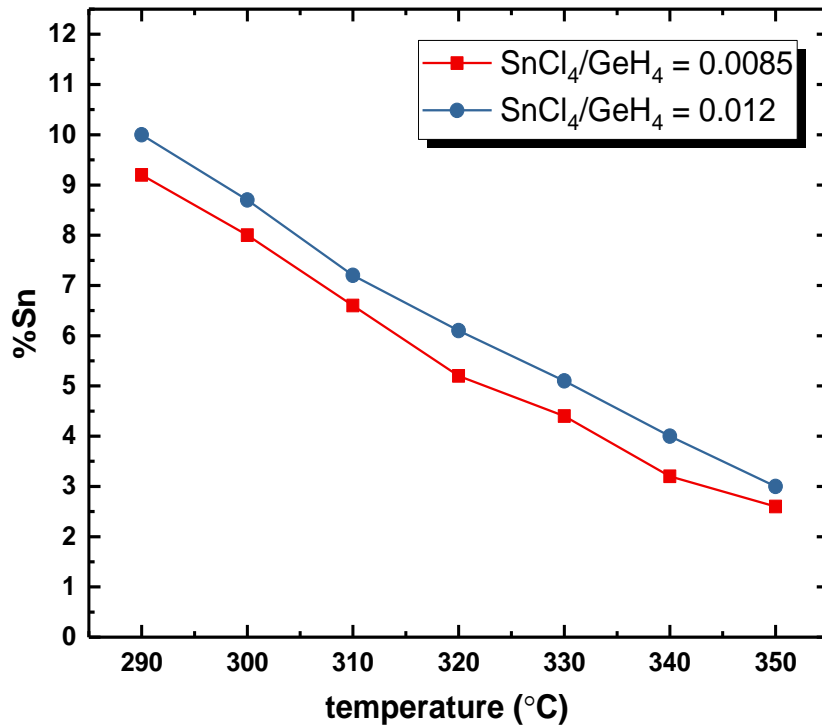


Figure 19 Plots how the %Sn incorporated changes with temperature for two SnCl₄/GeH₄ conditions.

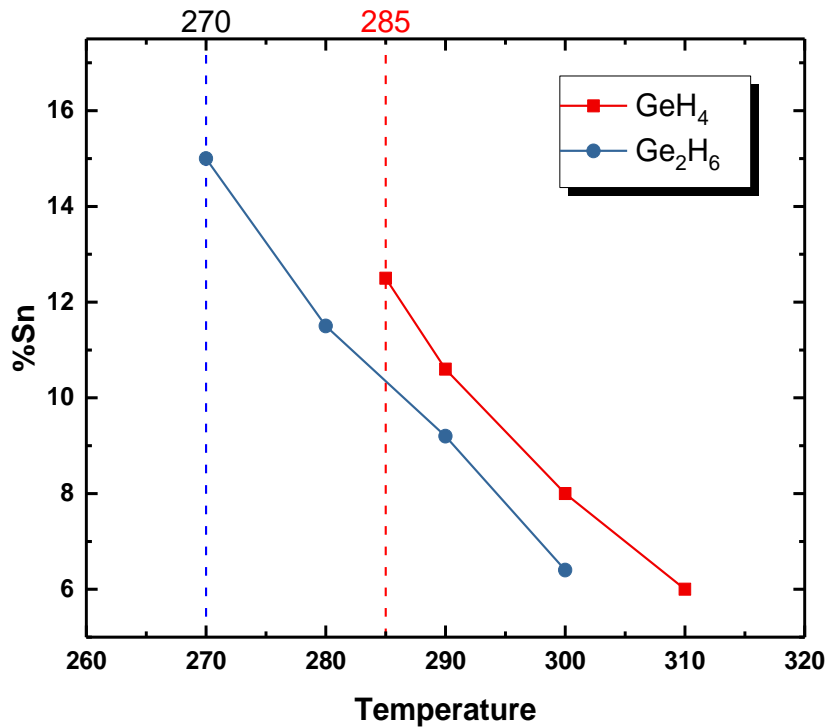


Figure 20 A comparison of the Sn incorporation vs. temperature between using GeH₄ and Ge₂H₆. All other growth conditions were kept the same. The red and blue dashed lines demark the temperatures below which all epitaxial growth ceases

decreased would be expected. The shift in the low temperature limit between GeH_4 and Ge_2H_6 indicates the reactivity of the Ge-hydride is the limiting factor. The generation of surface H and reactive GeH_2 species during Ge-hydride adsorption are most-likely required to complete the reduction on SnCl_x on the surface. Therefore, when the lower temperature limit of Ge-hydride adsorption is reached the SnCl_x can desorb before being incorporated. Within the temperature window we can see that for the same temperature and for $\text{SnCl}_4/\text{GeH}_4 = \text{SnCl}_4/\text{Ge}_2\text{H}_6$ that the Sn composition is higher for GeH_4 -based growth. This is most likely due to an increase in the Ge growth rate component for the Ge_2H_6 -based chemistry.

3.1.3. THE INITIAL STAGES OF GESN GROWTH

The understanding of the initial stages of heteroepitaxial growth is very important, through this understanding the defect generation and relaxation can be better controlled. Additionally, with this understanding more precise interfacial composition control can be achieved. For some materials the early stages of growth can be delayed by the formation of islands which then coalesce to form a continuous layer similar to what we have described in section for Ge growth on silicon. Controlling this coalescence will improve the layer morphology and defectivity. We have observed a GeSn growth delay time (t_0) which can be up to 80 seconds, however it is not immediately evident that this delay is due to a classic nucleation process. Figure 21 plots the GeSn layer thicknesses as functions of growth time for flow ratios of $\text{SnCl}_4/\text{GeH}_4 = 0.0085$ and 0.012 . The temperatures were adjusted to 320°C (high-

flow) and 330°C (low-flow) to ensure identical growth rates of 22 nm/min. Despite the identical growth rates different values of $t_0 = 79$ sec and 56 sec were measured for the low-flow and high-flow respectively [32]. This seems to indicate that the delay time is independent of growth rate. Epitaxial growth modes have been described by Bauer [45] as a balance between interfacial energy and strain energy. The Sn atom has a lower surface energy than the Ge atom so that an alloy of GeSn should wet a Ge surface from a surface energetics point-of-view. Obviously the addition of Sn to the Ge lattice should also introduce interfacial strain energy which can counteract the layer wetting and 2-dimensional growth. Under certain conditions these considerations can lead to an epitaxial nucleation delay. Figures 22(a)-(c) compare 5x5 μm AFM scans taken at 20, 40, and 60 seconds of growth on the high-flow layer. In the AFM images it is apparent that some amount of islanding and coalescence is occurring in these early stages. The dark regions are exposed growth surface and the lighter regions are elevated epitaxial islands with surface-steps delineating the epitaxial peaks and troughs. Based on the sequence of AFM images it would appear that islands are nucleated and coalesce through a classic step-flow mechanism. However further analysis indicates the initial stages of growth are far more complicated. Figure 23 compares the LEIS spectra for the samples shown in figures 22(a)-(c).

Low energy ion scattering (LEIS) is a highly surface-sensitive measurement of the composition in the upper-most 10Å of the surface [46]. In the 20 and 40 sec samples there is only a Ge peak and an O peak due to the surface oxide. A Sn peak does not appear however until the 60 sec of growth time, this means that for at least

the first 40 sec of growth no Sn is incorporated. Moreover the decreasing delay time with increasing $\text{SnCl}_4/\text{GeH}_4$ suggests that is in fact a kinetic limitation to the initial Sn incorporation which is responsible for the delay. There may be a dynamic balance between SnCl_x adsorption and desorption which must be attained before epitaxial layer growth can initiate. The Ge-buffer surface is hydrogen terminated when GeSn growth starts and at $T < 400^\circ\text{C}$ the desorption of H would be slow and thus precursor adsorption would also be. Once enough Sn is incorporated to form an initial monolayer of GeSn the availability of sites becomes more rapid. At higher SnCl_4 flow an adsorption equilibrium is achieved more rapidly and thus the delay is decreased

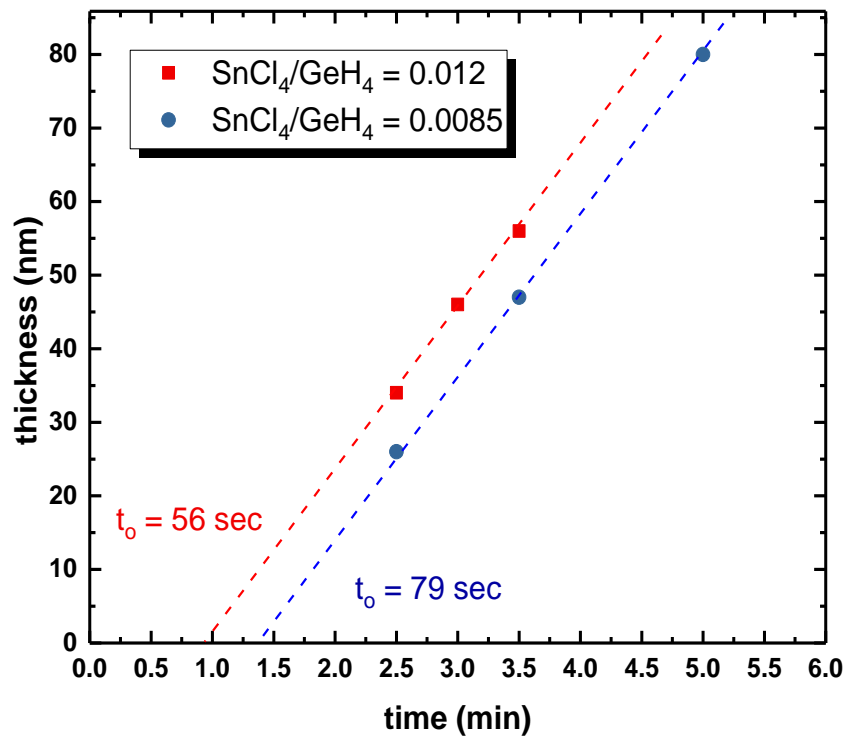


Figure 21 GeSn layer thicknesses vs. growth time for 3% and 7% Sn layers. The identical growth rate of 22 nm/min was observed. The nucleation delay times (t_0) of 79 and 56 s were extracted for 3% and 7% Sn layers, respectively [32].

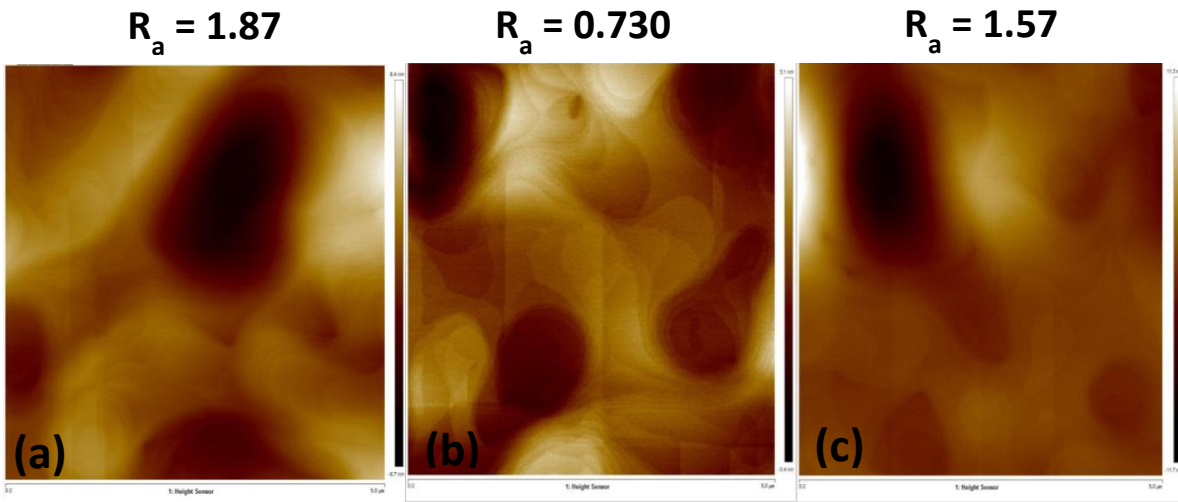


Figure 22(a)-(c) AFM images of the initial stages of growth (a) 20 seconds, (b) 40 seconds, and (c) 60 seconds.

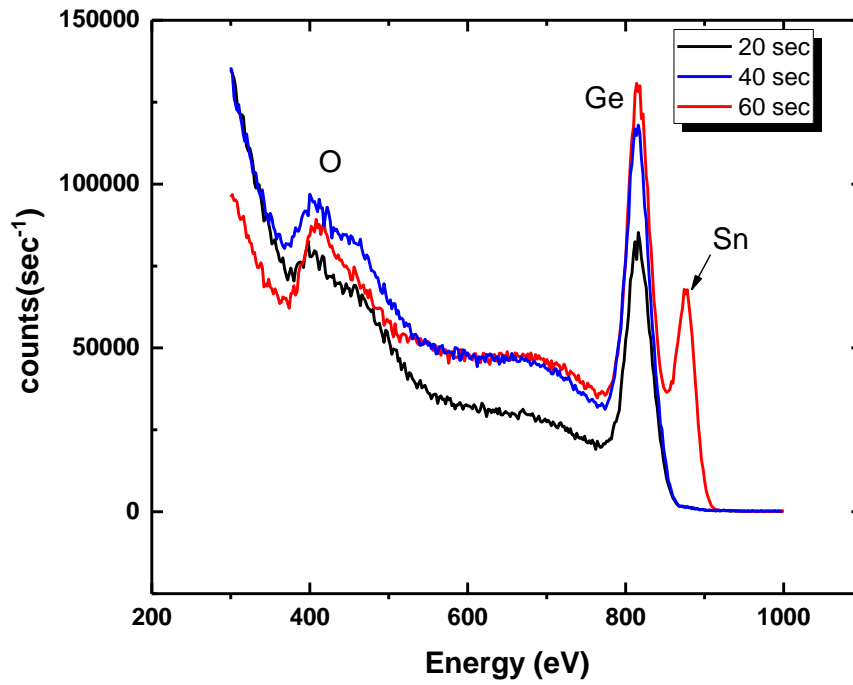


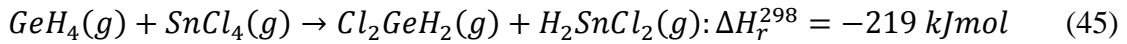
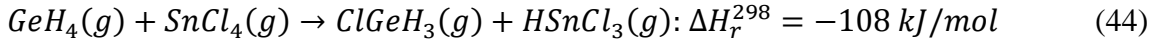
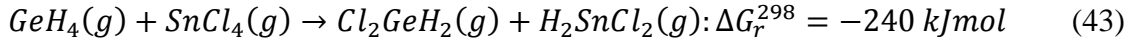
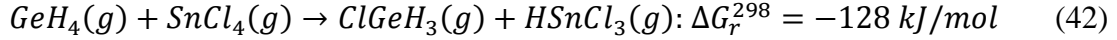
Figure 23 LEIS spectra for the initial stages of GeSn growth at 20, 40 and 60 sec. No Sn is measured on the surface until after 40 seconds growth time.

3.1.4. GAS-PHASE AND SURFACE CHEMISTRY

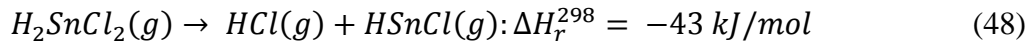
Using the observed data we have presented in sections 3.1.1 through 3.1.3 we can develop an understanding of the growth chemistry. The reaction pathway consists of the following general steps: 1) Gas-phase reaction of GeH_4 and SnCl_4 ; 2) Adsorption of SnCl_x^* and GeH_x^* on the growth surface; 3) Reduction SnCl_x to Sn^* ; and 4) Diffusion of Sn^* to an incorporation site – and incorporation. However step 4 is reversible via segregation of incorporated Sn atoms out of the growing layer and back to the growth front.

In the gas phase homogenous reactions would be expected due to the high growth pressure. As explained in section 3.1.1 the homogenous decomposition reactions are unlikely due to their high activation energies; $\text{SnCl}_4 \rightarrow \text{SnCl}_2 + \text{Cl}_2$, $\Delta H_r = 362 \text{ kJ/mol}$ and $\text{GeH}_4 \rightarrow \text{GeH}_2 + \text{H}_2$, $\Delta H_r = 235 \text{ kJ/mol}$. However reaction between SnCl_4 and GeH_4 in the gas-phase has not been analyzed experimentally or theoretically. Serenate et. al. have suggested that SnCl_4 and Ge_2H_6 react in the gas phase to form chlorostannanes and chlorogermanes of the form $\text{H}_x\text{SnCl}_{4-x}$ and $\text{Cl}_x\text{Ge}_2\text{H}_{6-x}$ [47]. However no further discussion or experimental work is offered to support this notion. Here we use thermochemical data from references [48] and [40] to predict reactions occurring in the gas phase and on the surface which lead to the formation of epitaxial GeSn. The thermochemical values discussed herein are not intended to be exact but only used to predict general reaction mechanisms and trends.

The gas-phase reaction of the starting precursors was found to be highly energetically favorable. ΔG_r^{298} and ΔH_r^{298} are calculated for reactions 42 and 43 however due to limited thermochemical data only values are calculated for subsequent reactions.



These values are for $T = 298\text{K}$ however both reactions remain favorable with $\Delta G_r < 0$ over the range of temperatures used for GeSn growth. Figure 24 plots ΔG_r vs. T at 1 atm for both reactions, the dichloro-products are favored over the trichloro-products over this whole temperature range. H_xSnCl_{4-x} should be far less stable and much more reactive than the tetrachloride which would enable the low temperature growth. The Sn-H bond is quite weak and SnH_4 is known to readily disassociate at elevated temperatures. Reference [40] predicts the Sn-H bond energy to decrease with increasing Cl substitution therefore we would expect homogenous decomposition of the form:



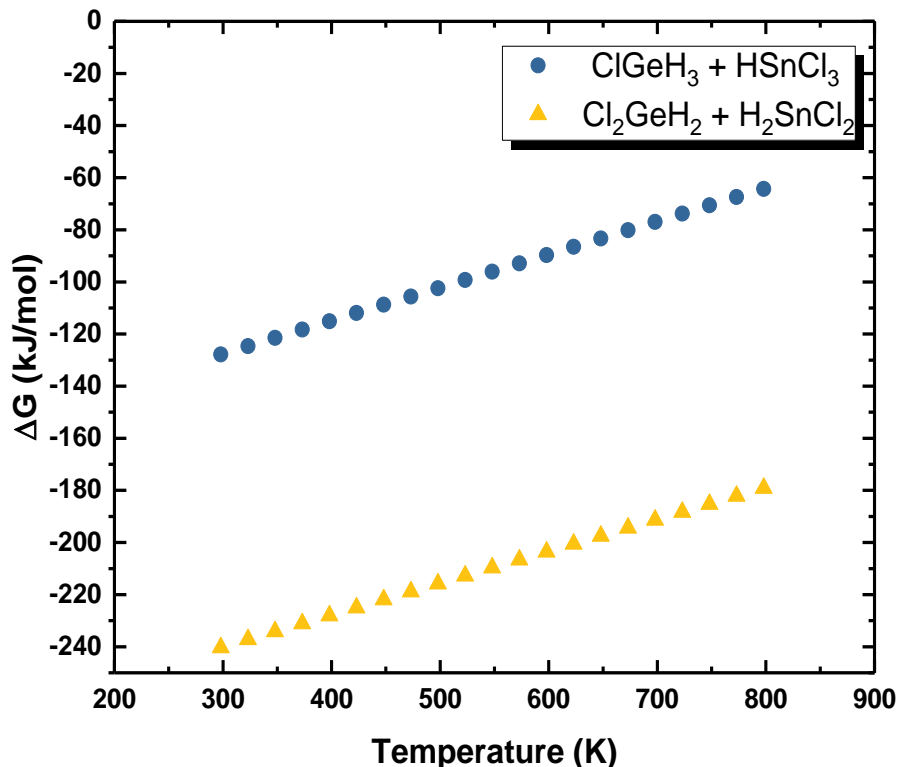
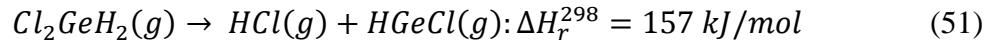
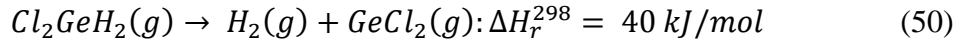
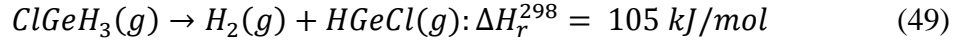


Figure 24 Plots the Gibbs free energy vs. temperature for reactions 42 and 43 the dichloro-products are favored for all temperatures.

The negative enthalpies imply that these reactions readily occur and are not thermally activated. Thus pre-dissociated molecular Sn fragments are available which makes for facile adsorption on the growth surface. The adsorption reaction may only be first-order in θ because only one open site (denoted by $*$) would be strictly required; $SnCl_2(g) + _ * \rightarrow SnCl_2^*$ and/or $HSnCl(g) + _ * \rightarrow HSnCl^*$. Therefore the Sn-fraction would be proportional to $x_{Sn} \sim [SnCl_2][HSnCl]\theta$ and the dependence on Cl and H desorption would relatively small. The negative ΔH_r values would also explain why the Sn-component of the growth has an apparent negative activation energy.

The rate constant for the reaction $\text{GeH}_4 \rightarrow \text{GeH}_2 + \text{H}_2$ can be estimated as $k = 10^{14.3} \cdot \exp(-225 \text{ kJ/mol}/RT)$ which for a temperature of 320°C, $k = 3.2 \times 10^{-6} \text{ s}^{-1}$ [42]. Therefore the homogenous decomposition of GeH_4 is not a significant reaction pathway for the incorporation of Ge. On the other hand, the energetic barriers for homogenous decomposition of $\text{Cl}_x\text{GeH}_{4-x}$ species are significantly lower:

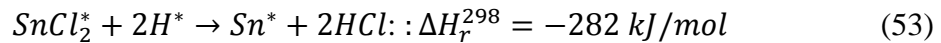
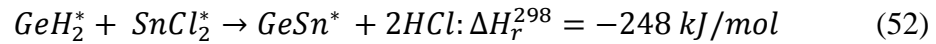


Only a small portion, roughly 1%, of the GeH_4 would be converted to chlorogermanes because $\text{GeH}_4/\text{SnCl}_4 \sim 100$. However as we see in section 3.1.1 the incorporation efficiency of GeH_4 is in the range of 0.3-3% and increases with SnCl_4 flow. In fact the GeH_4 incorporation efficiency scales as $\sim 0.5(\text{SnCl}_4/\text{GeH}_4)$ which suggests that roughly half of the Ge incorporated is done so through the chlorogermane conversion pathway. This also indicates that the high growth rates (at low temperature) are not only due to catalytic Cl and H desorption from surface-Sn, but also gas-phase conversion of SnCl_4 and GeH_4 to more reactive intermediates. Similarly we could expect that only one site would be required for adsorption of these pre-dissociated species, $\text{GeCl}_2(g) + _ * \rightarrow \text{GeCl}_2^*$.

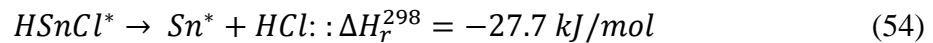
In parallel to the single-site adsorption of GeCl_2 and HGeCl we would also expect the dissociative adsorption of germane. This can take the form of $\text{GeH}_4(g) + 2_ * \rightarrow \text{GeH}_3^* + \text{H}^*$ and/or $\text{GeH}_4(g) + 3_ * \rightarrow \text{GeH}_2^* + 2\text{H}^*$ [49]. The adsorption of GeH_4 is therefore 2nd or 3rd-order in θ , however the 2nd-order reaction most-likely dominates at

the high surface coverages/low temperatures for our growth conditions. We would expect the Ge growth rate component to be much more dependent on the desorption of H and Cl and the creation of open surface-sites i.e. thermally activated. Furthermore the germanium fraction in the layer could be written as, $x_{Ge} \sim ([GeCl_2][HSnCl])\theta[GeH_4]\theta^n$, where n could take-on values between 2 and 3 depending on how operative the 2nd or 3rd-order reactions are. It is important to relate this back to figure 13 and our discussion in section 3.1.1 where we see the Sn-incorporation had a non-linear dependence. The higher reaction order in θ of GeH_4 means that as the Sn content on the surface is increased the Ge incorporation becomes more efficient. The increased H and Cl desorption increases θ , and x_{Ge} will increase as θ^3 or θ^4 whereas x_{Sn} will only increase as θ .

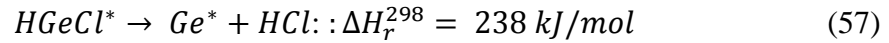
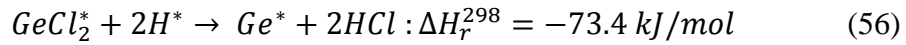
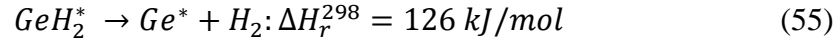
We next use the thermochemical values in references [40] and [50] as a qualitative guide to the reaction energetics. However these values have inherent error due to the involvement of the surface which will change the energetics somewhat. The adsorbed GeH_2^* and H^* are likely critical in the subsequent surface reaction steps with the chlorinated Sn and Ge species also on the surface:



The formation of HCl is the driving force for many of the surface reactions as seen above, and may also occur without the need for two reacting surface species:



The creation of Sn^* and $GeSn^*$ is followed by surface diffusion and incorporation. Reaction 52 is preferred from a growth perspective over reactions 53 and 54 as it creates a Ge-Sn bonded pair whereas the creation of independent Sn atoms on the surface may allow for the formation of Sn-Sn bonded pairs and ultimately Sn-precipitates. Ge^* surface species are created by the reactions:



The Ge^* also diffuses on the surface and incorporates. We notice that surface reactions 52, 53, 54, and 56 are exothermic reactions 55 and 57 are thermally activated. We expect that most of the Ge is incorporated via reaction 55 however the formation of $GeCl_2$ creates an exothermic reaction pathway for Ge incorporation in reaction 56 which could also explain the increased GeH_4 efficiency with increasing $SnCl_4$. Figure 25 is a diagram which summarizes the primary gas-phase and surface reactions which lead to GeSn growth.

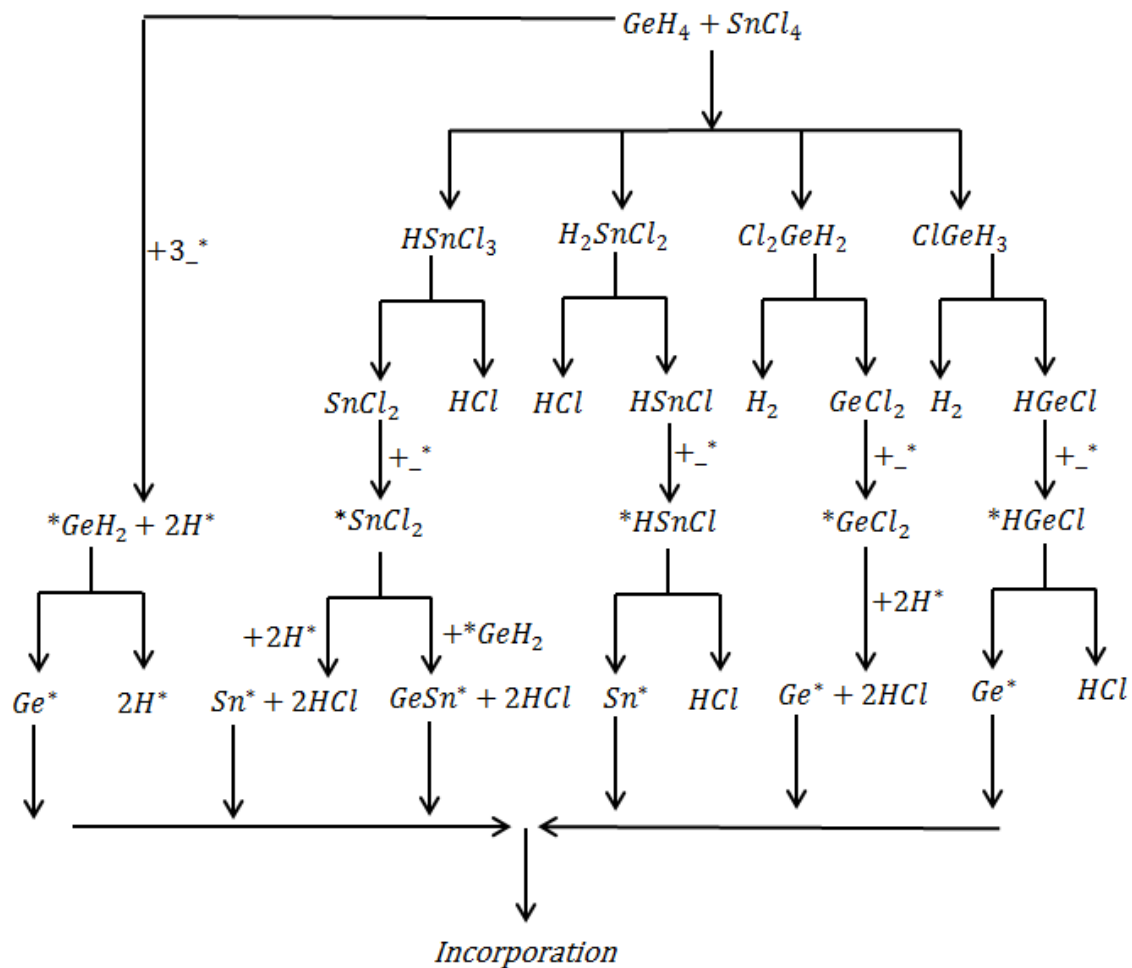


Figure 25 Possible reaction pathways starting with GeH_4 and $SnCl_4$ in the gas-phase. Dichloro-product formation is highly favored (center pathways) however the high excess of GeH_4 means that dissociative adsorption (far-left pathway) must be responsible for supplying the majority of reactive Ge species to the growth surface

3.2 MATERIALS CHARACTERIZATION OF UNDOPED GESN

In this section HRXRD, RBS, and PL results briefly discussed to demonstrate material quality on GeSn on Ge layers. Representative XRD spectra for $\text{Ge}_{1-x}\text{Sn}_x$ ($x = 0.01$ to 0.12) are shown in figure 26 and indicate that the layer is single crystal. The GeSn peak shifts to lower Bragg angle with increasing Sn which is indicative of tetragonal distortion of the out-of plane lattice constant and demonstrates tunability of the lattice constant. The GeSn peak position allows for determination of the Sn-content through Vegard's law. If the layer is partially-relaxed then both in-plane and out-of-plane lattice constants must be measured to determine the Sn-content. Figure 27 shows random and aligned RBS spectra of a $\text{Ge}_{0.93}\text{Sn}_{0.07}/\text{Ge}/\text{Si}(100)$ structure showing a χ_{\min} (ratio of the aligned spectra to the random spectra) of 5% for both the Ge and Sn of the GeSn layer indicating that the Sn is fully substitutional within the Ge lattice. The χ_{\min} is a measure of the crystalline perfection of the layer in which a perfect Si crystal would have a theoretical χ_{\min} of 4.2%.

Figure 28 shows the room temperature photoluminescence spectra of for $\text{Ge}_{1-x}\text{Sn}_x$ layers with $x = 0.01$ to 0.12 , a pure Ge sample is included for reference. The intensity has been normalized however it can be seen that the PL wavelength increases with the Sn-content which demonstrates the band gap tunability. Furthermore this figure demonstrates light-emitting and photonic device quality material over the entire range of compositions.

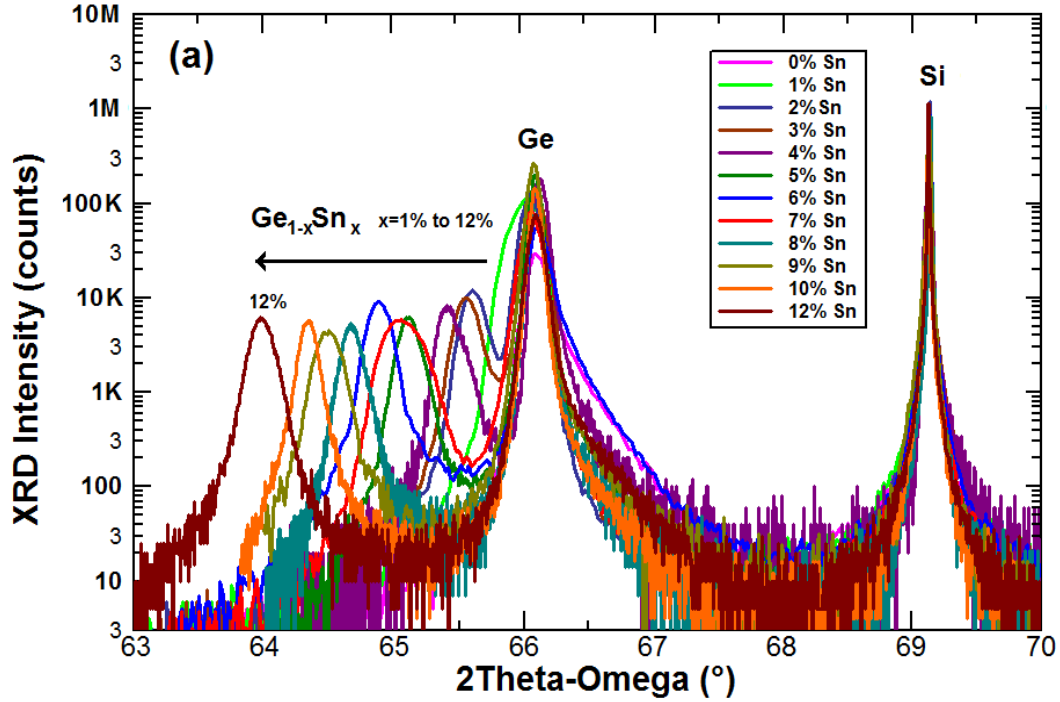


Figure 26 HR-XRD of GeSn layers with 1-12% Sn where the increase in Sn is shifting the peak to lower Bragg angle.

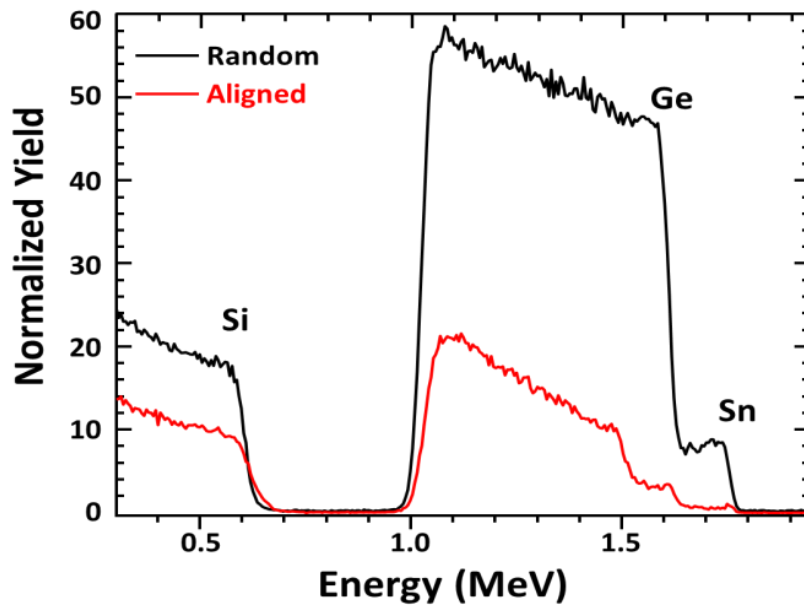


Figure 27 Random and channelled RBS spectra of a 5%Sn layer. The low intensity of the channelled peak means that the Sn is highly substitutional

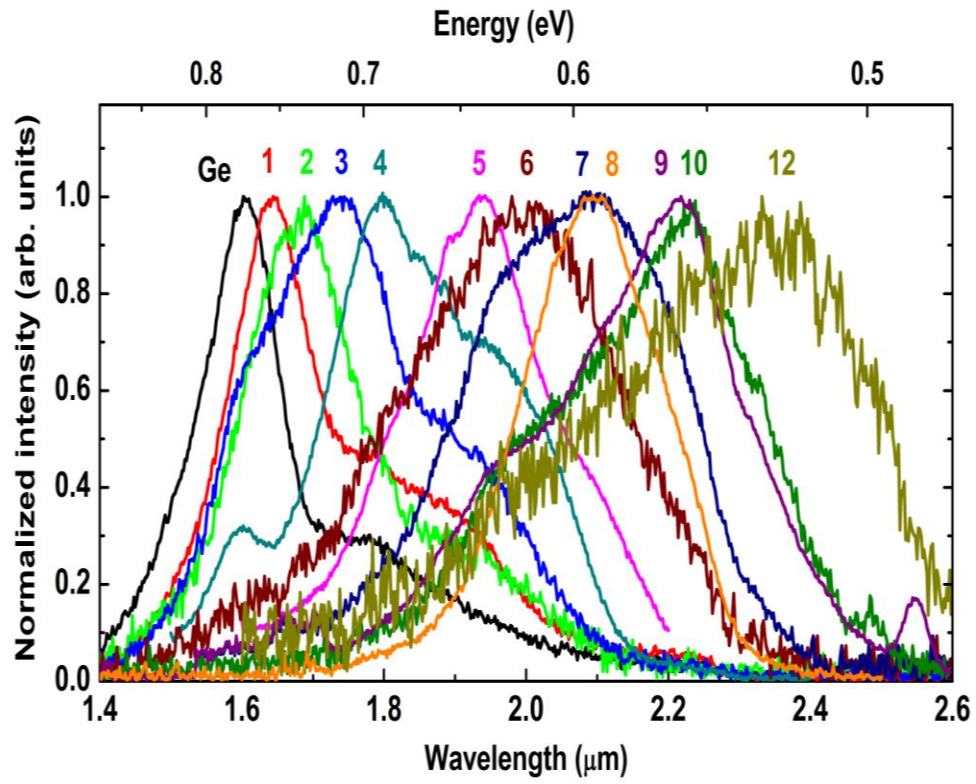


Figure 28 Normalized room temperature PL for 1-2% Sn layers with pure Ge included as a reference

CHAPTER 4

STRAIN-RELAXATION AND THE LIMITS OF SN INCORPORATION

4.1 STRAIN RELAXATION AND DEFECT PROPAGATION

Thus far we have only discussed the growth of layers strained to the Ge-buffer layer. As explained in section 1.1 Strain-relaxation of GeSn layers is favorable for optoelectronic properties. Strain relaxation can be facilitated through post-growth annealing and/or growth beyond the critical thickness. Post-growth annealing is not favored for GeSn because of the alloy's meta-stable nature, thermal energy from the annealing decreases the kinetic barriers to Sn diffusion and precipitation. Strain relaxation proceeds when the strain energy accumulated during further growth in the layer matches the dislocation formation energy where the strain is relieved by the necessary formation of misfit and $\langle 110 \rangle (111)$ threading dislocations. It is well known that these crystal defects can act as non-radiative recombination centers much to the detriment of device performance. Therefore while strain relaxation is desired it must be done in a way that minimizes the defect density in active device layers. Here we present a systematic study of $\text{Ge}_{0.91}\text{Sn}_{0.09}$ growth well beyond the critical thickness as a means to produce strain-relaxed, direct band gap, optoelectronic device quality materials.

We chose to study layers with $\sim 9\%$ Sn because it is technologically relevant, that is to say it has high enough Sn content to be direct-gap, but low enough to avoid problems such as Sn-segregation. The $\text{Ge}_{0.91}\text{Sn}_{0.09}$ Layers were grown on Ge-buffered

silicon and had (SIMS measured) thicknesses of 152 nm, 180 nm, 257 nm, 570 nm, and 865 nm. The People and Bean model for critical thickness, h_c , is expressed as:

$$h_c = \frac{1+\nu}{1-\nu} \frac{1}{16\pi\sqrt{2}} \frac{b^2}{a} \left(\frac{1}{f^2} \ln\left(\frac{b}{h_c}\right) \right) \quad (58)$$

where ν is the Poisson ratio, b the burger's vector, a the GeSn layer lattice constant, and f the lattice mismatch between the GeSn and Ge buffer [51]. A critical thickness of 100 nm is predicted for a layer containing 9% Sn.

X-ray diffraction reciprocal space maps (XRD-RSM) were used to extract the in-plane, a_{\parallel} , and out-of-plane, a_{\perp} , lattice constants which are related to the peak positions in reciprocal space (Q_x , Q_y) by the expressions:

$$a_{\perp} = \frac{2\lambda}{Q_y} \quad (59)$$

$$a_{\parallel} = \frac{\lambda\sqrt{8}}{2Q_x} \quad (60)$$

Where λ is the X-ray wavelength = 1.54056 Å. The unstrained lattice constant for a given Sn composition is given by:

$$a_0^{GeSn} = \frac{(a_{\perp}^{GeSn} + 2a_{\parallel}^{GeSn} \left(\frac{C_{12}}{C_{11}}\right))}{(1 + 2\left(\frac{C_{12}}{C_{11}}\right))} \quad (61)$$

where C_{12} and C_{11} are the elastic constants. We next obtain the degree of relaxation by, $R = (a_{\parallel}^{GeSn} - a_{\parallel}^{Ge}) / (a_0^{GeSn} - a_{\parallel}^{Ge})$. The composition was determined by using the calculated value of a_0^{GeSn} in conjunction with Vegard's law. The full width half max (FWHM) values of the (004) RSM peaks are an effective indicator of threading

dislocation density (TDD) in the layer. Secondary ion mass spectrometry (SIMS) was then used to obtain Sn depth profiles in order to examine the evolution of the compositional profile.

The energy of dislocation formation is a critical point for this study. For GeSn growth, in general the low growth temperatures less than 400 °C are necessarily to be employed. The formation of 90° edge dislocations is typically less energetically favored than 60° $a/2$ $\langle 110 \rangle \{111\}$ dislocations, however the strain relieving efficacy of the former is superior to the latter case. Despite the low growth temperatures, GeSn is known to form 90° Lomer edge dislocations for growth on Ge-buffered Si(100) even for relatively low mismatch and low relaxation [8]. Layers grown on Ge-buffered Si by CVD at temperatures between 300-400°C relax mainly through the formation of sessile 90° edge dislocations [4, 51-54] with defects confined at the GeSn/Ge interface. While reports of layers grown on Ge(100) by MBE at temperatures of 100-150°C feature relaxation through glissile 60° misfits with threading segments extending through the layer [52]. In our work, on relaxed GeSn growth we have observed an extended interfacial defective region, however the defects are confined in this region, allowing low-defect layers to be grown on top. To the best of our knowledge no prior study of how different substrates/buffer-layers and/or growth temperatures affect the relaxation mechanism has been reported yet. We believe that the defect density in the starting growth surface as well as the growth temperature are responsible for the observed differences. Etch-pit density measurements on our relatively thin Ge buffers reveal defect densities in the 5-9

$\times 10^7 \text{ cm}^{-2}$ range. This is a relatively high defect density and would make relaxation by threading of 60° dislocations from the buffer to the GeSn more likely.

It has been shown that the relative density of 60° and 90° dislocations can be estimated from the aspect ratio of the XRD-RSM peak [55]. The aspect ratio is defined as the full width at half maximum (FWHM) in the Q_x direction over the FWHM in Q_y direction, i.e., $\Delta Q_x/\Delta Q_y$. For layers with mainly 60° dislocations the aspect ratio is larger than those which contain mainly 90° dislocations. This is due to the increased anisotropy of the strain-field around the 60° dislocation relative to the pure-edge dislocation ultimately causing the peak to elliptically distort. Table 2 lists the sample thicknesses with their degree of relaxation and their (004) XRD-RSM aspect ratio $\Delta Q_x/\Delta Q_y$ [56]. For the sample with 152 nm thickness the layer is 10% relaxed and $\Delta Q_x/\Delta Q_y = 1.96$ with a highly elliptical shape to the peak, which indicates the initial stage of relaxation is mainly accommodated by 60° misfits propagating from the Ge-buffer and across the GeSn. As the thickness and the degree of relaxation increase, the $\Delta Q_x/\Delta Q_y$ decreases to a final value of 1.59, which suggests an increasing number of 90° misfit dislocations are being formed later in the relaxation process. The formation of pure edge-type dislocations becomes easier for increased strain relaxation which can be a result of mobile 60° misfits reacting to form immobile 90° misfits. Bolkhovityanov and Sokolov have thoroughly reviewed these phenomena in group IV semiconductor growth [57], which is suitable for GeSn in this study. Two 60° MD's gliding along $\{111\}$ mirror-planes with Burgers vectors of \mathbf{b}_1 and \mathbf{b}_2 can meet on $\{100\}$ growth-planes and form a pure edge dislocation with Burgers vector \mathbf{b}_3 , for example:

$$\frac{a}{2} [10\bar{1}] + \frac{a}{2} [011] = \frac{a}{2} [110] \quad (62)$$

Table 2 SUMMARY OF SAMPLE XRD-RSM CHARACTERISTICS

<u>Total thickness (nm)</u>	<u>Relaxation</u>	(004) $\Delta Q_x/\Delta Q_y$	<u>Overlayer %Sn</u>	<u>over layer thickness (nm)</u>
152	10%	1.96	-	-
180	44%	1.92	-	-
257	66%	2.10	10.0%	107
570	88%	1.68	11.7%	420
865	94%	1.59	12.0%	715

To proceed this reaction the energy of \mathbf{b}_3 must be less than $\mathbf{b}_1 + \mathbf{b}_2$. Not all complimentary $\langle 110 \rangle \{111\}$ MD's meet this requirement. Other possible interactions between complimentary 60° MD's can result in annihilation, i.e., when $\mathbf{b}_1 + \mathbf{b}_2 = \frac{a}{2} [000]$. Therefore, it is obvious that as the degree of relaxation increases the chance of complimentary MD's capable of forming pure edge dislocations increases. Figure 29 shows a cross-sectional transmission electron microscopy (TEM) image of the 570 nm layer, where a ~ 150 nm-thick defective bottom layer is observed at the GeSn/Ge interface. However defects in this region do not propagate to the rest of the GeSn layer. This may be explained as follows; the initial strain relaxation is accommodated by the propagation of 60° dislocations from the Ge buffer to the GeSn layer. These are mobile and are able to continue to glide through the GeSn layer as they grow. However 60° MD interaction increases which may form networks of immobile 90° dislocations. These

networks can then block remaining 60° MD's from gliding into subsequently grown material. This implies that optimization of the Ge buffer layer may not be crucial to achieve high quality relaxed GeSn as conventional experience would suggest. Typically defect densities of $< 1 \times 10^7 \text{ cm}^{-2}$ are sought in Ge-buffer applications. Generally speaking, the buffer layer thickness must be $\sim 1.5\text{-}2 \text{ }\mu\text{m}$ to achieve low defect which is costly from a manufacturing perspective. In this study, the newly discovered growth mechanism suggests a thickness of $\sim 600 \text{ nm}$ would be sufficient.

(224) XRD-RSM's for the 152 nm and 865 nm layers are shown in figure 30 where we observe that the single GeSn peak splits into two distinct peaks with increasing thickness. This of course indicates that two different Sn compositions are grown however no growth conditions were altered during the process. In table 2 we also list the Sn compositions of these secondary layers which increase with thickness and become increasingly relaxed relative to the base layer. We defer discussion of why the Sn composition is changing to the next section however the fact that the composition seems to be increasing gradually means that a spontaneous grading results which is relevant to our discussion of defects. Grading the composition of epitaxial layers as a means of defect reduction has been studied extensively and further theoretical discussion can be found in reference [58]. Figure 31 shows the SIMS Sn depth profiles for the layers in table 2, and we can see at 152 nm the composition is fairly flat. However at 270 and 570 nm we can see the development of a graded region, and finally in the 865 nm it appears there are three distinct regions. The first $\sim 100 \text{ nm}$ are relatively flat followed by a $\sim 350 \text{ nm}$ graded region and then a second flat region which constitutes the overlayer. It is

important to note that the Sn-composition gradient, $\Delta\text{Sn}/\Delta x$, revealed by SIMS analysis likely causes underestimation of the actual $\Delta\text{Sn}/\Delta x$ value due to the SIMS “knock-on” effect. This is especially relevant noting the 5 keV Cs⁺ beam energies used, however

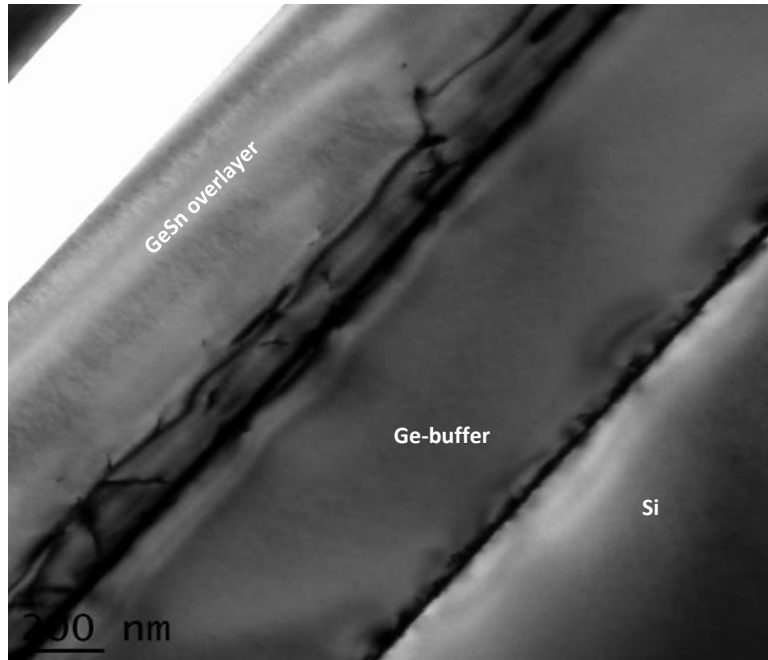


Figure 29 Cross-sectional TEM image of the 570 nm layer. A highly defective interfacial layer is seen on the Ge buffer and then an apparently low defect density layer on top of the defective interfacial layer [56].

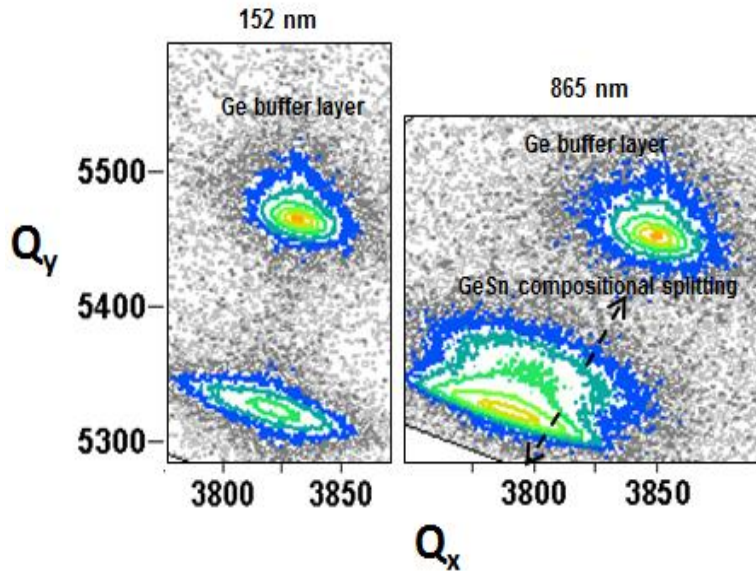


Figure 30. XRD-RSM's for the 152 nm and 865 nm layers. There is a single GeSn peak for the 152 nm layer, this peak splits into two distinct peaks in the Q_y direction after relaxation. This indicates two compositions are present in the layer [56]

beam energies in the 500 eV range would be required to properly resolve the gradient, resulting in unpractical sputter rates for an 865 nm layer. The actual value of $\Delta\text{Sn}/\Delta x$ aside, the gradual grading in between the first layer and the overlayer physically separates dislocations. Through physical separation dislocation-dislocation interaction is minimized which increases the glide length and strain-relieving efficacy of each 60° dislocation. Resulting in a lower number of dislocations required to facilitate layer relaxation. Ultimately there are two contributing factors to defect reduction in our thick relaxed layers; 1.) the conversion of mobile 60° MD's during the initial relaxation into immobile 90° MD's which can then also act as impediments to remaining mobile 60° MD 2.) The spontaneous development of a compositionally graded region in-between the defective interfacial region and secondary layer.

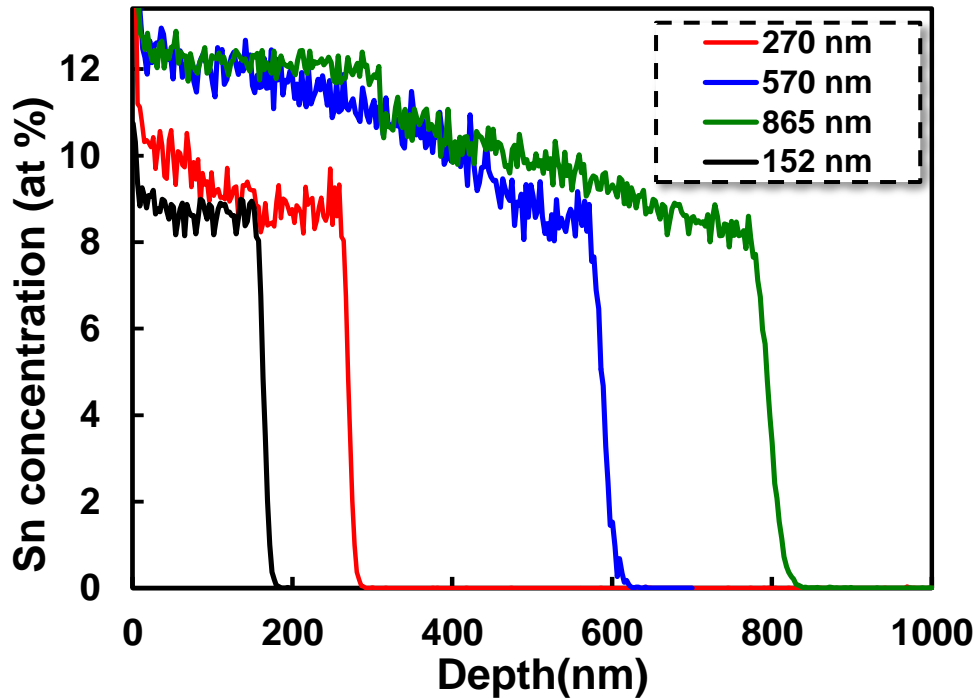


Figure 31 SIMS Sn-depth profiles for the 152 nm, 270nm, 570 nm, and 865 nm layers. Comparing the profiles shows an initially uniform composition which starts to grade as the thickness is increased [56]

4.2 THE EFFECT OF STRAIN ON SN-INCORPORATION

Up to this point we have only discussed the effects of the spontaneous grading in composition and have ignored discussion of the origin of the grading. In this section we explain the source of this spontaneous increase in Sn incorporation and propose that the final Sn composition is primarily limited by strain, and chemistry is only secondary. We finally use this data to engineer light emitting layers with Sn compositions up to 17.5% Sn which is the highest Sn composition reported thus far on an industrial CVD reactor. Moreover, photoluminescence of these layers produces light emission at $\sim 3.1 \mu\text{m}$. Up to 25% Sn has been reported by UHV-CVD growth methods [9] but these methods do not produce light emitting materials at such high levels of Sn.

There are three fundamental factors governing Sn-incorporation during CVD GeSn layer formation: 1.) Chemistry, the chemical reaction of precursors supplies reactive intermediates of Ge and Sn to the growth front 2.) Surface kinetics, the diffusion of Ge and Sn to lattice incorporation sites 3.) Surface segregation, the loss of Sn from the sub-surface lattice sites and back to the surface of the growth front. The growth chemistry effects the ratio of Sn:Ge that can be made available at the growth front. In terms of chemistry there are two common approaches; utilizing Sn-hydrides [9,47] or Sn-chlorides [10-12]. In both cases various Ge-hydrides are used as Ge precursors. The difference between these two methods mainly is found in comparing the stability of the Sn-hydride vs. that of the chloride. The Sn-H bond is weaker than the Sn-Cl and thus is more reactive at the low temperatures required for GeSn epitaxy. Of course the SnH₄ molecule is so unstable, even at room temperature, that to achieve epitaxial growth the hydrogen must be replaced with deuterium (SnD₄). This deuterated stannane molecule is still highly unstable and specialized synthesis and handling is required however it does have a distinct advantage over SnCl₄ in that the partial pressure can be varied independently of the Ge-hydride because it is sufficiently reactive on its own [47]. This means that a larger ratio of Sn:Ge can be made available for incorporation at the growth front.

The use of SnCl₄ is preferable from a manufacturing standpoint, however epitaxial growth can only be accomplished within a narrow range of partial pressures. As we have discussed in our previous work [32] and in chapter 3 the Ge-hydride is required to facilitate gas-phase and surface reactions which otherwise would not proceed due to the strong Sn-Cl bond. Therefore growth conditions always require excess GeH₄/Ge₂H₆ and

there is an upper limit to the ratio of Sn:Ge intermediates that can be produced at the growth front. Now with a Sn:Ge ratio established on the surface of the growing layer, surface kinetic factors will influence the transport of Sn* and Ge* adatoms either to lattice incorporation sites or to form secondary phases. At a given temperature and pressure there is a maximum value of Sn:Ge ratio that can be accommodated without secondary phase formation. For example higher temperature and lower pressure conditions will increase surface diffusivity enabling Sn* adatoms to form equilibrium secondary Sn phases. This is in contrast to classical epitaxial growth conditions where high temperatures and low pressures are favored such that adatoms can diffuse and find the most energetically desired sites.

Now to our central argument, the amount of Sn that is incorporated and remains incorporated depends mainly on temperature and strain. A sub-surface and incorporated Sn atom has a tendency to segregate back to the surface via site exchange. This is due to the lower bond energy of the Sn atom relative to the Ge atom and also due to the mismatch in atomic radii which are 0.12 nm for Ge and 0.14 nm for Sn. The segregated Sn content, C_{Sn}^0 , relative to the subsurface content, C_{Sn} , is expressed as:

$$\frac{C_{Sn}^0}{C_{Sn}} = \exp\left(\frac{-\Delta G_{seg}}{kT}\right) \quad (63)$$

where:

$$\Delta G_{seg} = \frac{1}{\rho} (\sigma_{Ge} - \sigma_{Sn}) + \frac{-24K_{Sn}G_{GeSn}r_{Sn}r_{GeSn}(r_{Sn}-r_{GeSn})^2}{3K_{Sn}r_{Sn}+4G_{GeSn}r_{GeSn}} \quad (64)$$

where ρ is the surface atomic density and σ_{Ge} and σ_{Sn} are the respective bond energies. This first term represents the driving-force for segregation due to the mismatch in bond energies. The second term represents the driving force for segregation due to strain, where K_{Sn} is the bulk modulus of Sn, G_{GeSn} is the shear modulus of $Ge_{1-x}Sn_x$, and $r_{Sn} - r_{GeSn}$ represents the difference in atomic radii between the solute and solvent. For the $Ge_{1-x}Sn_x$ alloy this is more accurately the *average* atomic radius in the alloy due to lattice expansion [59,60]. Changes in the bond-energetic term are only minor as C_{Sn} increases whereas the strain energy term increases (decreases) as $(r_{Sn} - r_{GeSn})^2$ and thus strain dominates ΔG_{seg} . However a given Sn atom's ability to segregate to the surface can be kinetically frustrated at low temperature. Therefore the Sn-composition is known to increase with decreasing growth temperature. If we neglect the bond energy term and set the numerator and denominator in the strain term to be A , then eq. 61 can be approximated as:

$$\frac{C_{Sn}^0}{C_{Sn}} = \exp\left(\frac{-A(r_{Sn}-r_{GeSn})^2}{kT}\right) \quad (65)$$

From this expression a comparison of strain and temperature effects on Sn segregation can be made clearer. For example, a 1% increase in temperature results in a $\sim 1.3x$ increase in $\frac{C_{Sn}^0}{C_{Sn}}$. However a 1% increase in r_{GeSn} results in a $\sim 30x$ increase in $\frac{C_{Sn}^0}{C_{Sn}}$. Therefore controlling the strain in the growing layer should be the most important control parameter in terms of maximizing Sn-content.

In order to test the effect of layer strain on Sn incorporation we systematically varied the starting in-plane lattice constant $a_{||}$ on the intended growth surface. This was done through a step-grading technique whereby the starting lattice constant was varied by adjusting the Sn-content and degree of relaxation of a $\text{Ge}_{1-x}\text{Sn}_x$ buffer layer. For each starting $a_{||}$ a second $\text{Ge}_{1-y}\text{Sn}_y$ layer was grown in which all other growth conditions were held constant so that any increase in y would only be the result of a reduction in strain due to the larger starting $a_{||}$. Figure 32 plots the measured Sn-composition in the $\text{Ge}_{1-y}\text{Sn}_y$ layer vs. the starting $a_{||}$ in the $\text{Ge}_{1-x}\text{Sn}_x$ buffer layer. The first point at $a_{||} = 5.665\text{\AA}$ was grown on a Ge-buffer as a reference and resulted in 12.0% Sn as measured by XRD-RSM. The Sn content increases rather linearly and at our largest value of $a_{||} = 5.759\text{\AA}$ we achieve 19% Sn as measured by XRD-RSM and SIMS. This is the highest Sn-content yet reported on an industrial CVD reactor. Moreover, in figure 33 the photoluminescence spectra at 150 K reveals the longest emission wavelengths of 3133 nm that ever reported of GeSn. Prior to this the longest reported wavelength of light emission from GeSn was $\sim 2.7\ \mu\text{m}$ [61]. The valley at around $3.1\ \mu\text{m}$ is due to the water absorption. This demonstrates the applicability of the GeSn system in a much wider range of the IR spectrum.

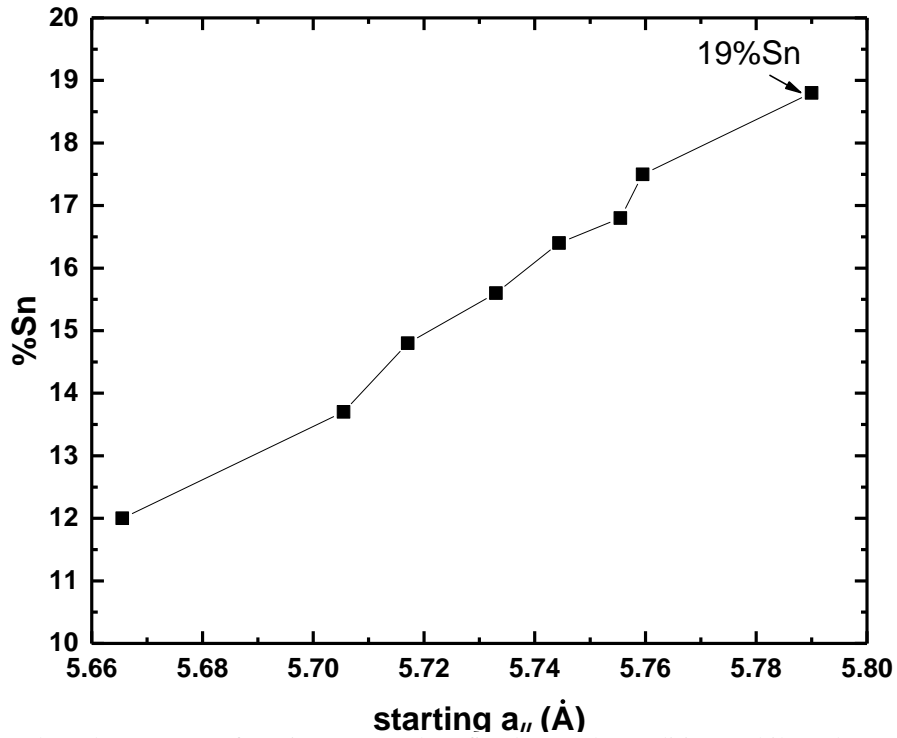


Figure 32 Plots the amount of Sn incorporated at fixed growth conditions while only varying the starting lattice constant of the relaxed GeSn buffer layer. Growth directly on the Ge buffer is limited to 12%Sn but for the same conditions up to 19%Sn can be achieved if the strain of growing layer is reduced.

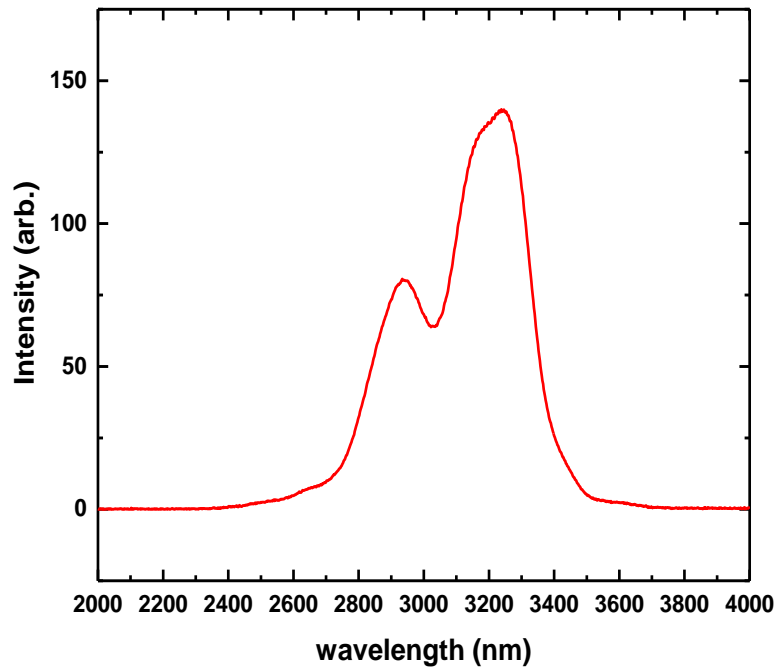


Figure 33 150 K photoluminescence spectrum of a 17.5% Sn layer which was grown on the multi-layered buffer. The emission peak at 3133 nm was observed. The valley at around 3.1 μm is due to the water absorption [56].

CHAPTER 5

GROWTH OF UNDOPED $\text{Si}_Y\text{Ge}_{1-X-Y}\text{Sn}_X$

5.1 INTRODUCTION TO $\text{Si}_Y\text{Ge}_{1-X-Y}\text{Sn}_X$

The ternary $\text{Si}_{1-x-y}\text{Ge}_x\text{Sn}_y$ alloy will allow independent tuning of the band-gap and lattice constant. Figure 34 below shows the theoretical lattice constant and band gap space (a , E_g) that can be covered for silicon (5.43Å, 1.12 eV), germanium (5.65 Å, 0.66 eV), and tin (6.49 Å, 0 eV). Vegard-type equations are used to predict the variation of lattice constant and band gap as:

$$a_{\text{SiGeSn}} = (1 - x - y)a_{\text{Ge}} + xa_{\text{Si}} + ya_{\text{Sn}} + x(1 - x)b_{\text{SiGe}} + y(1 - y)b_{\text{GeSn}} \quad (66)$$

$$E_{\text{SiGeSn}}^{\Gamma,L} = (1 - x - y)E_{\text{Ge}}^{\Gamma,L} + xE_{\text{Si}}^{\Gamma,L} + yE_{\text{Sn}}^{\Gamma,L} + x(1 - x - y)b_{\text{SiGe}} + y(1 - x - y)b_{\text{GeSn}} - xyb_{\text{SiSn}} \quad (67)$$

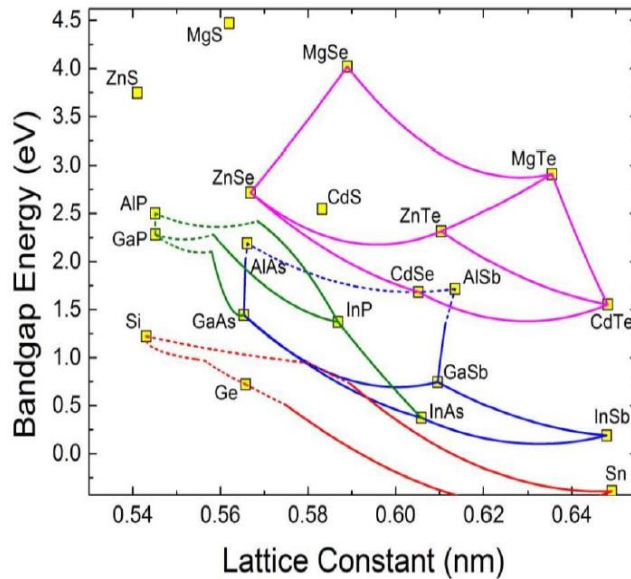


Figure 34 Bandgap and lattice constant coverage for the Si-Ge-Sn system. III-V and II-VI are also shown in the figure for comparison

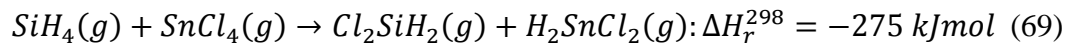
Where b represents bowing parameters in the linear behavior of the lattice parameter and/or band gap, these exact values can be found in references [62,63]. However unlike Ge which has a small 0.136 eV offset between the direct Γ -valley and indirect L-valley, the offset for Si is quite large at 2.3 eV. Therefore as silicon is added to a GeSn alloy the direct-indirect crossover is pushed-out to higher and higher tin levels. Propitiously a direct band gap is not explicitly required for SiGeSn as it would primarily be used as cladding/barrier material and recombination will be confined to the GeSn active region. Rather the control of the composition is required to ensure type-I band alignment, however this is complicated if the indirect barrier layer and direct gap active layerl conduction band minima are misaligned in k-space. Moreover the positions of the conduction band maxima are complicated by splitting of HH and LH bands. Therefore the SiGeSn composition is at least nominally selected with the position of the GeSn band-edges in mind. Practically speaking however strain and growth chemistry are additional constraints which limit access to certain compositions.

5.2 $\text{Si}_Y\text{Ge}_{1-X-Y}\text{Sn}_X$ GROWTH RESULTS

CVD growth progress of the ternary $\text{Si}_{1-x-y}\text{Ge}_x\text{Sn}_y$ has lagged behind that of $\text{Ge}_{1-x}\text{Sn}_x$. This is despite the fact that theory predicts that the three component alloy should be more thermodynamically stable owing to increased mixing entropy [64]. Also, for the same Sn content in a layer, a layer with Si will act to compensate the compressive strain due to Sn. Si compensates the strain effect of Sn at a ratio of 3.7 to 1, which should reduce the driving force for Sn segregation and surface degradation. The caveat to these points

however is that they assume the layer is a random alloy. Recent work indicates that there are in-fact preferred bonding and ordering arrangements, and that Si atoms will seek sites which minimize nearest neighbor interactions with Sn atoms [65]. This may account for the difficulty in producing high-quality SiGeSn layers in practice. Thus far CVD growth has been successfully done using SnD₄ and SnCl₄ tin precursors with higher order germanes, Ge_nH_{2n+2}, and silanes, Si_nH_{2n+2} [63, 64]. Despite the success of these approaches the CVD precursors are not the optimum choice from a manufacturing point of view. SiH₄ and GeH₄ are industry standard precursors and are preferred in terms of achieving low-cost CMOS integrated epitaxy solutions for group IV photonics. These lower order hydrides were for a long time considered unsuitable for (Si)GeSn CVD due to their poor cracking efficiencies at low temperature. None-the-less we have been successful in our use of GeH₄ for GeSn growth and although we have demonstrated that SiGeSn growth with SiH₄ is possible, our understanding and control is limited at this point [32].

It is perhaps unexpected that SiH₄ reacts at temperatures of ~ 300°C when the Si-H bond dissociation energy is 398 kJ/mol [66]. In the gas phase the reaction of SiH₄ with SnCl₄ the formation chlorosilanes should be highly favorable:



Within the group IV epitaxy community chlorosilanes such as dichlorosilane (DCS) are only considered suitable for higher temperatures i.e. T > 650°C. This is mainly due to the

lower growth rate of DCS relative to SiH_4 at a given temperature. However, contrary to popular belief the lower growth rate is not due to less efficient decomposition of the chlorinated species relative to the hydride at a fixed temperature. Rather it is due to increased Cl surface coverage and or etching upon dissociation. In fact the Si-H bond strength decreases with increasing Cl substitution. For example the Si-H bond energy in SiH_4 is 398 kJ/mol and for H_2SiCl_2 the Si-H bond energy is 390 kJ/mol. Furthermore kinetic effects produce a much higher low temperature ($T < 400^\circ\text{C}$) sticking coefficient for DCS than for SiH_4 [66]. Therefore the above gas-phase reactions may enable Si incorporation at such low temperatures.

At low SiH_4 flow rate the growth rate does not change much whereas at high SiH_4 flow rate the growth rate can be drastically reduced. Figure 35 plots the growth rate and Si composition as functions of $\text{SiH}_4/\text{GeH}_4$ ratio at constant SnCl_4 flow rate. The Sn composition for each epitaxy run is annotated next to the data points. The decrease in growth rate is not unexpected due to the formation of Si-H and S-Cl surface species which would slow the overall desorption rate relative to the GeSn-only surface. The Si incorporation follows a power law dependence saturating at high ratio of $\text{SiH}_4/\text{GeH}_4$ while the Sn composition decreases along with $\text{SiH}_4/\text{GeH}_4$. The saturation of Si-content as well as the decrease in Sn-content with increasing $\text{SiH}_4/\text{GeH}_4$ is expected based on the repulsive interaction explained above. As expected at higher temperature an increase in Si incorporation can be observed for the same $\text{SiH}_4/(\text{GeH}_4 + \text{SnCl}_4)$ ratio. Not only is the SiH_4 more reactive as temperature is increased but the characteristic reduction in Sn content at elevated temperature would partially relieve repulsive interactions between Si

and Sn. However an increase in the SnCl₄ flow at fixed SiH₄/GeH₄ will result in a decrease in the Sn and Si contents.

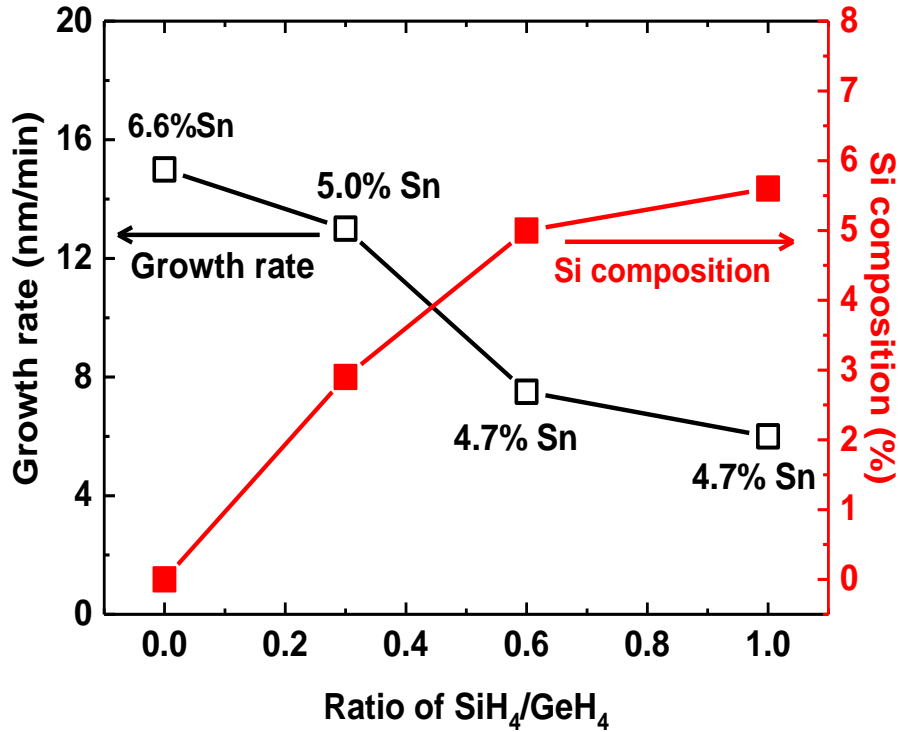


Figure 35 plots the growth rate of SiGeSn vs. SiH₄/GeH₄ (left axis) and the Si composition vs. SiH₄/GeH₄ (right axis) for a fixed SnCl₄ flow. The Sn composition is annotated at each point in black.

This is illustrated in figures 36(a) and (b) where the SIMS for two SiGeSn layers is compared. For both layers the growth temperature is 300°C and the SiH₄/GeH₄ = 0.6. However the layer in 36(a) had a SnCl₄/GeH₄ = 0.012 and the layer shown in 36(b) had SnCl₄/GeH₄ = 0.0085. It can be seen in figure 36(a) that there is a grading in Si profile or perhaps a delay in Si incorporation. The Si content peaks at 2.8% in this layer and the Sn content peaks at 4.5% but decreases to ~ 3% near the surface. Comparatively the layer in 36(b) has flat profiles with equal amounts of Si and Sn at 4.5%. These results suggest that

a parasitic reaction is occurring at higher SnCl_4 flows. The increased Cl surface coverage at higher SnCl_4 flow may promote the etching of incorporated Si via the formation of SiCl_x species which are minimally reactive at such low growth temperatures. The Si-Cl bond is quite favorable with a bond energy of 3.95 eV and it is likely that this etching behavior reduces the Si content in the layer.

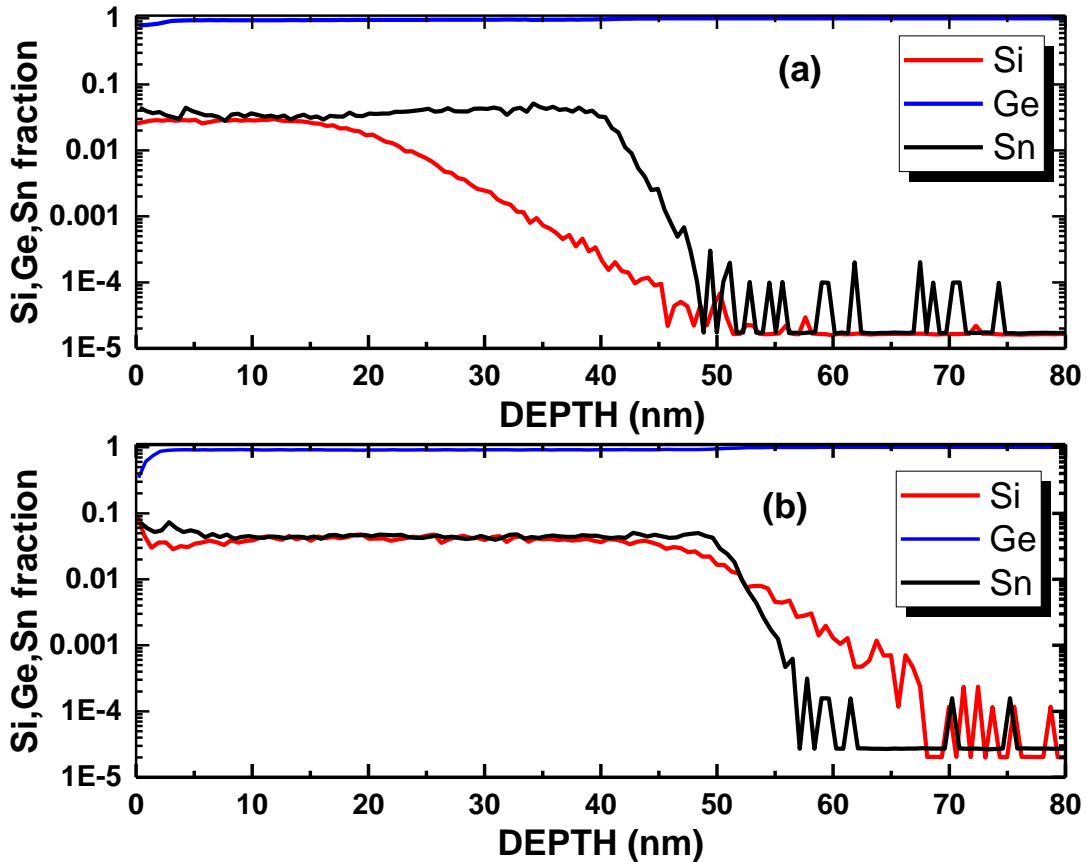


Figure 36(a) and (b) the SIMS of SiGeSn layers grown at high $\text{SnCl}_4/\text{GeH}_4$ (a) and low $\text{SnCl}_4/\text{GeH}_4$ (b). The layer grown at higher $\text{SnCl}_4/\text{GeH}_4$ has a graded Si profile with only 2.8% Si incorporated while the one grown at low $\text{SnCl}_4/\text{GeH}_4$ has a flat Si profile with 4.5% Si

Despite the compositional grading effects described above high quality layers can still be realized by proper selection of growth conditions. The XRD scans in figure 37 show a range of SiGeSn compositions that can be grown. All these layers feature single, well-defined SiGeSn peaks indicating homogenous composition. The SiGeSn peak appears at a larger Bragg angle for more Si-rich layers. SiGeSn peaks are observed on both sides of the Ge-buffer layer peak indicating both compressive and tensile strained layers. The various ranges of Si and Sn compositions that can be growth demonstrate the potential of SiGeSn in strain and band-gap tuning.

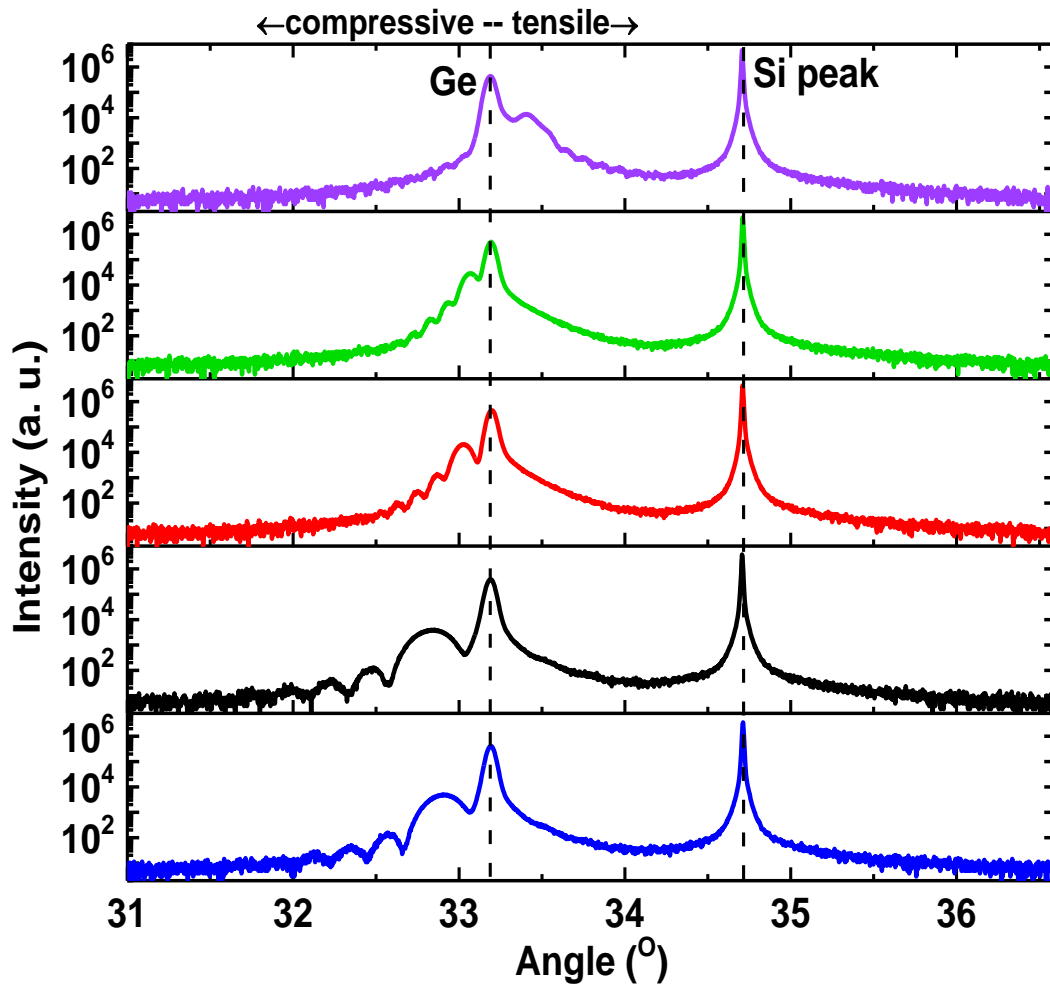


Figure 37 HRXRD scans of SiGeSn layers with various compositions and lattice constants. SiGeSn peaks which are located to the right of the Ge-buffer peak are tensile strained while those to the left are compressive.

CHAPTER 6

GROWTH OF DOPED SI-GE-SN ALLOYS

The use of semiconductor materials in electronic and optoelectronic devices of course requires the formation of p-n junctions. Similar to the growth requirements of semiconductor alloys the doping concentration and concentration profile must be uniform and abrupt. Given that the dopant atom is a solute species with different surface energy and covalent radius, segregation can make this requirement a challenging one. There is the added complication the even though the concentration profile may be uniform the dopant atoms may not occupy tetrahedral bonding sites rendering them electrically inactive. In other semiconductor materials systems post-growth annealing can be employed to electrically activate dopant atoms. This is however not a favorable condition for producing p and n-type GeSn(Si) due to its inherent meta-stability. Obtaining high activation in as-deposited layers is an essential consideration.

6.1 P-TYPE $\text{Ge}_{1-x}\text{Sn}_x$

The growth of p-type $\text{Ge}_{1-x}\text{Sn}_x$ was accomplished through the addition of B_2H_6 to the process chemistry. With the addition of B_2H_6 significantly a notable increase in growth rate was observed. This phenomenon has been observed in other hydrogen-mediated low temperature growth of group IV materials and is thought to be a result of the B-catalyzed H desorption. This is similar to the effect we have previously discussed in section 3.1 for surface Sn atoms however it is not as simple as a weaker B-H bond energy. The effect was found to be more pronounced at higher temperatures possibly due to less efficient

hydrogen desorption at lower temperatures. Growth rates of up to 40 nm/min were observed for the highest B_2H_6 flows at 350-375°C. Growth rates this high at such low temperatures are generally not achievable however the effects of catalytic H-desorption from Sn and B sites could be an important future technological tool. Figure 38 plots the growth rate (left-axis) vs. B_2H_6 flow and the Sn incorporation (right-axis) vs. B_2H_6 flow. The complimentary behavior is shown in figure 39 where the B incorporation determined from SIMS is plotted vs. $SnCl_4/GeH_4$ for 4, 15, and 25 sccm of B_2H_6 . The observed reduction in Sn incorporation with increasing B_2H_6 has been reported by Vincent et. al. [10] and the authors attribute this behavior to site-competition. However site-competition should not occur between B and Sn as the smaller B atom would seek sites under local compressive strain while Sn atoms would seek sites under local tensile strain. Figure 5 illustrates the Si/Ge (100) 2×1 dimer reconstructed surface and the nature of the sites. A more likely explanation is that the incorporation of B induces compressive strain in the layer which would increase Sn-segregation out of the layer as discussed in section 4.2. Conversely an increase in $SnCl_4$ flow would limit boron incorporation through etching-type reactions i.e. the formation of boro-chloride species.

Layer thicknesses and compositions were measured by SIMS which revealed Sn and B profiles that were uniform and abrupt. A representative SIMS profile with 6.8% Sn and $1.38 \times 10^{19} \text{ cm}^{-3}$ B is shown in figure 40 below. The evaluation of the active boron concentration in the films was based on a comparison of the resistivity (electrically active boron) versus the total boron content of the layer obtained by SIMS. The measured

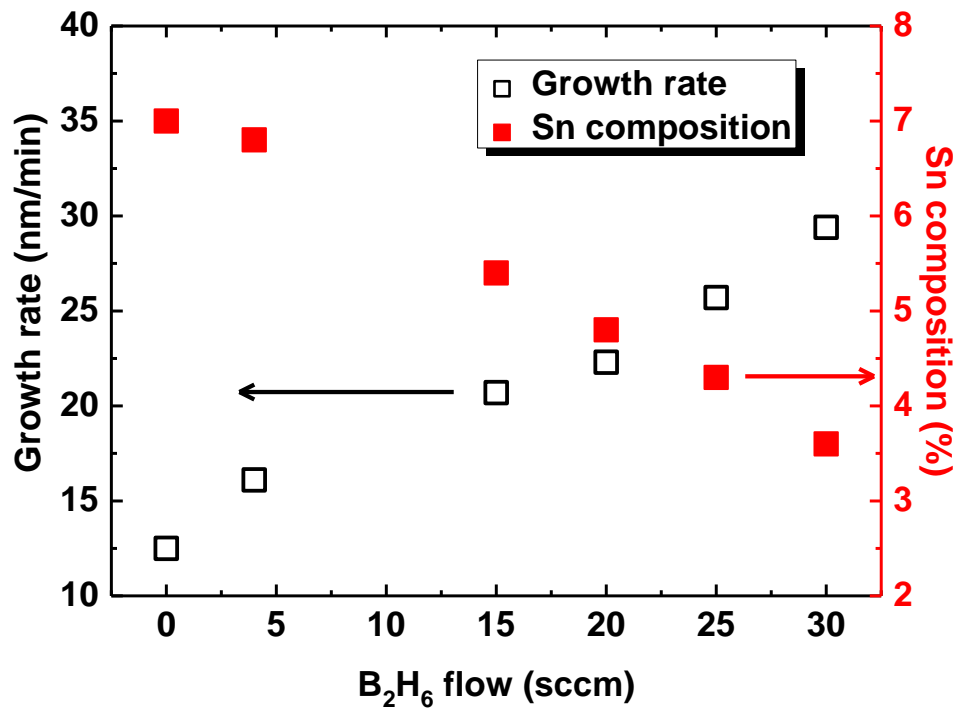


Figure 38 Plots the growth rate (left-axis) and %Sn incorporation (right-axis) as a function of B_2H_6 flow.

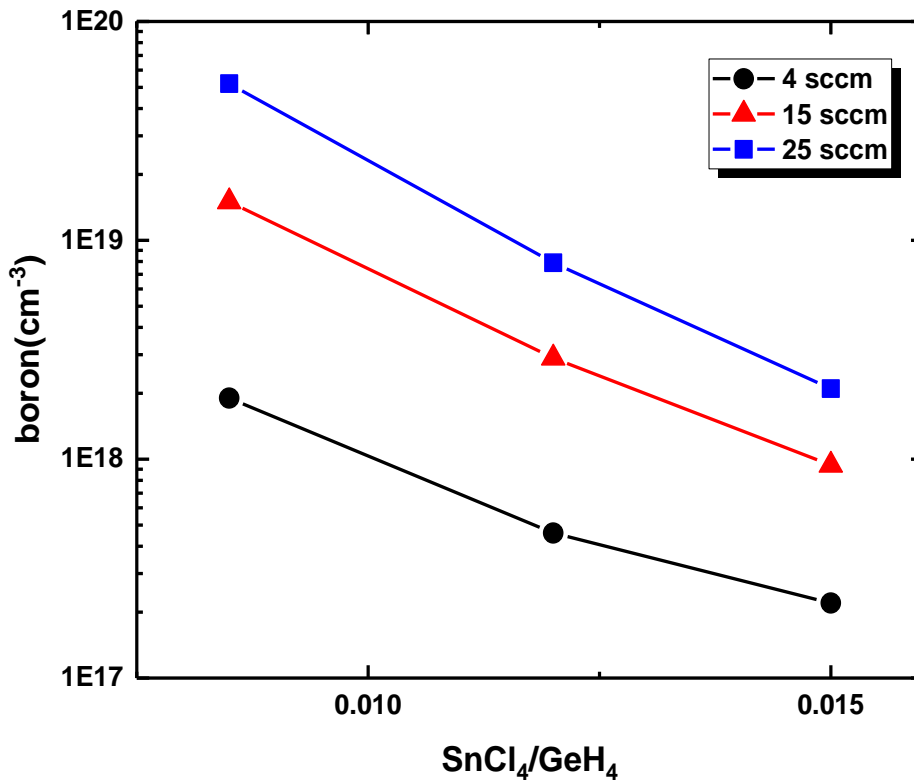


Figure 39 Boron incorporation vs. $SnCl_4/GeH_4$ at four different B_2H_6 flows.

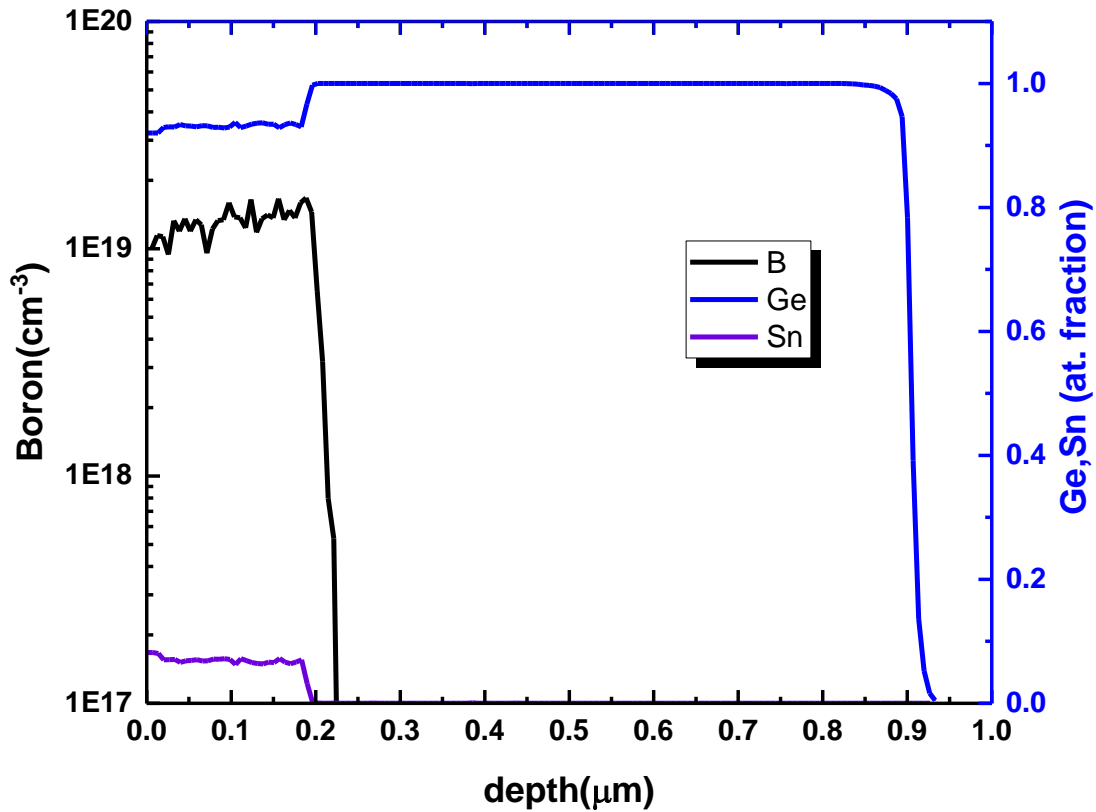


Figure 40 SIMS depth profile of a GeSn:B layer on Ge-buffered Si. Boron is shown in black, Sn in violet, and Ge in blue. The B concentration is on the left axis and the Ge/Sn on the right axis.

resistivity values, ρ , were used to estimate the electrically activated concentration of boron by considering $\rho = en\mu_h$. To calculate this properly one needs material specific hole/electron mobility values, μ_h , over a wide range of dopant concentrations. Electron and hole mobility values for $\text{Ge}_{1-x}\text{Sn}_x$ have not been studied in great detail yet and the mobility should vary with Sn-concentration as well as doping concentration. However for the low Sn-concentrations discussed in this work pure germanium could be used as an approximation. Figure 41 plots the SIMS/chemical dopant concentration (left axis) and

resistivity (right axis) vs. the B_2H_6 flow with all other conditions held constant. It is obvious from the figure that the B is incorporating into tetrahedral bonding sites due to the consistent decrease in resistivity with increasing chemical B concentration. From the lowest to highest B_2H_6 flows we observe an increase (decrease) in the B concentration (resistivity) of $1.80 \times 10^{18} \text{ cm}^{-3}$ and $6.1 \text{ m}\Omega$ at 4 sccm to $6.0 \times 10^{19} \text{ cm}^{-3}$ and $0.49 \text{ m}\Omega$ at 30 sccm.

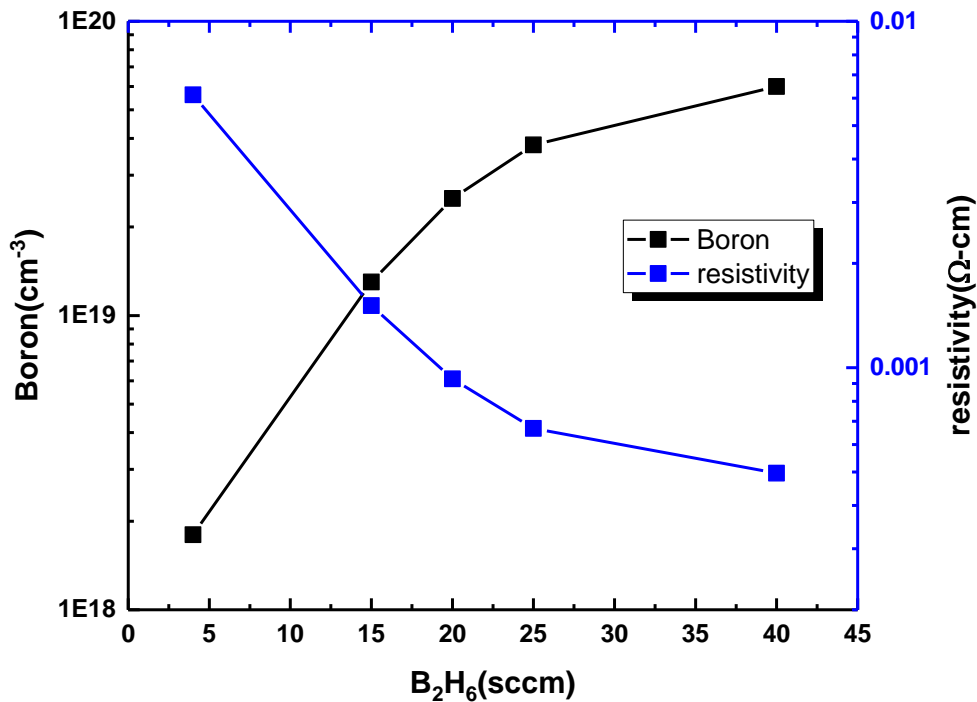
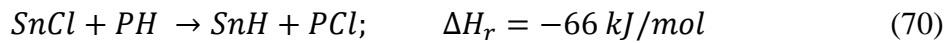


Figure 41 Plots the chemical B concentration as determined by SIMS (left-axis) and the resistivity (right-axis) as a function of the B_2H_6 flow.

6.2 N-TYPE $Ge_{1-x}Sn_x$

PH_3 was first selected as the n-type doping gas for GeSn. The addition of this gas also has a significant impact on the growth kinetics. Figure 42 plots the growth rate and Sn-composition as a function of PH_3 . No change in growth rate is observed with increasing

PH₃ flow although an increase in the Sn-content relative to the undoped growth was noticed. There is a modest initial increase in the Sn composition from 7.1% to 7.9% however this increase saturates with continued PH₃ increase. This behavior is not well understood however it is repeatable for multiple temperatures and precursor flows. The PH_x fragments on the surface may assist in the reduction of Sn-Cl* surface species which based on simple bond energy considerations should be favorable:



BH_x fragments from B₂H₆ dissociation should also assist in Sn-Cl reduction from a thermochemical point-of-view however the differences in bond length and thus strain may account for the difference. The Ge-Ge, Ge-P, and Ge-B bond lengths are 2.48Å, 2.46Å, and 2.28 Å respectively. Therefore the additional compressive strain created from B incorporation relative to P, which is almost strain-neutral, could counteract any catalytic effects of the B₂H₆ molecule on the surface. Figure 43 shows a representative SIMS profile for a P doped GeSn layer with $7.29 \times 10^{18} \text{ cm}^{-3}$ P and 9.8% Sn. The P profile is uniform and abrupt however Hall effect measurements revealed very low dopant activation. It is not clear at this point why P doping produces such low free carrier concentrations. AsH₃ was therefore screened as an alternative to PH₃ and the results were quite encouraging. For the same AsH₃/PH₃ flows a ~ 10x increase in incorporated As was measured relative to incorporated P [67]. Figure 44 plots the measured As/P by SIMS for the same AsH₃/PH₃ showing this behavior over a range of flows and compositions. Not only was the chemical incorporation of As higher than P

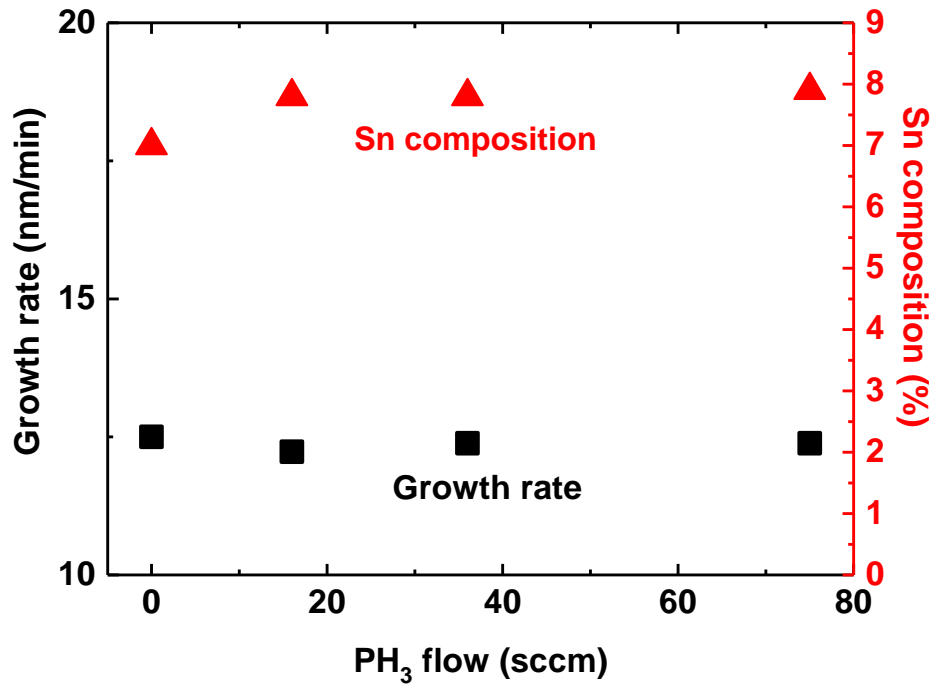


Figure 42 Plots the growth rate (squares, left axis) and the Sn composition (triangles, right axis) as a function PH₃ flow

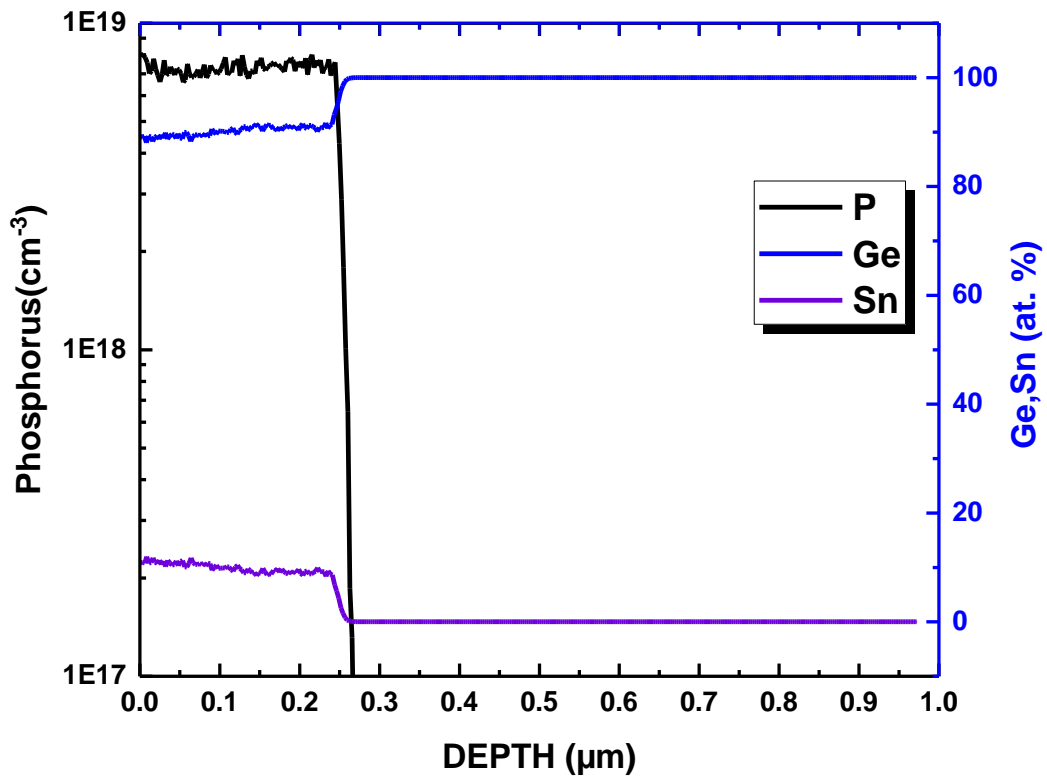


Figure 43 SIMS depth profile for a GeSn:P layer on Ge-buffered Si with Sn in red, P in violet, and Ge in black.

but it was also 90% electrically activated. AsH_3 is known to have a lower adsorption energy on Ge (100) and Si (100) than PH_3 [68, 69] thus for the same flows a higher fraction of AsH_3 would react on the surface. This is especially true for growth temperatures $< 400^\circ\text{C}$. The increased active fraction may also be related to the increased reactivity and/or lower As-H bond energy (294 kJ/mol) relative to the P-H bond energy (323 kJ/mol). Both AsH_3 and PH_3 dissociatively adsorb in the steps: $(\text{AsH}_3)\text{PH}_3 \rightarrow (\text{AsH}_2)\text{PH}_2 \rightarrow (\text{AsH})\text{PH} \rightarrow (\text{As})\text{P}$. The stronger P-H bonds may not allow for complete decomposition of P-H before being incorporated into the layer which effectively passivates the potential donor atom.

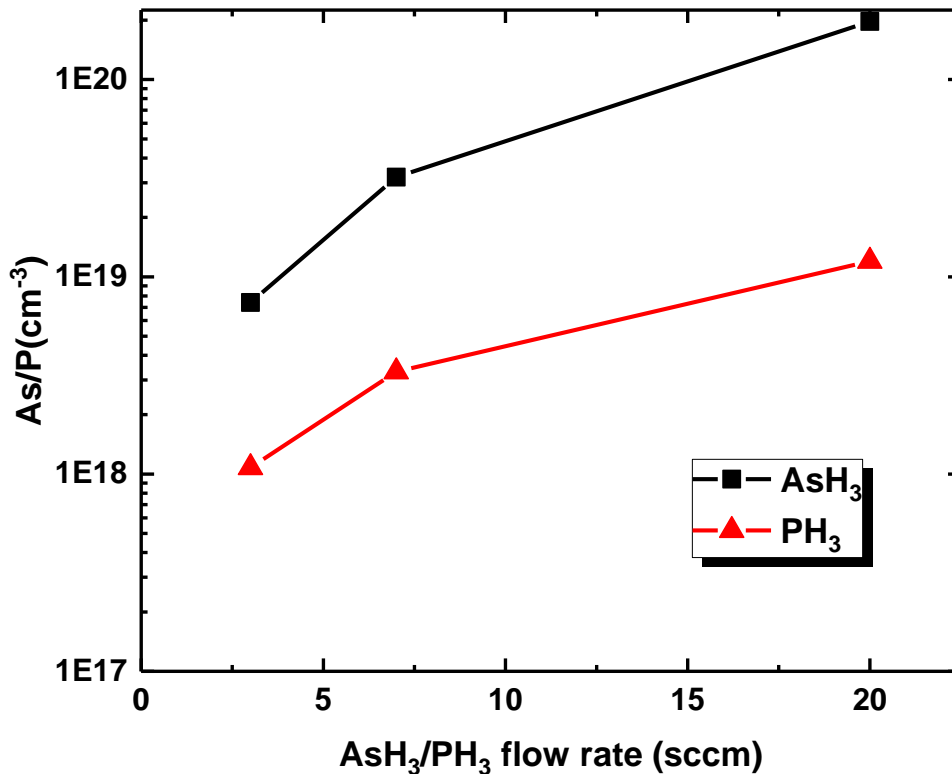


Figure 44 Plots the As (black squares) and P (red triangles) SIMS content as a function of equal AsH_3/PH_3 respective flow rates.

CHAPTER 7

OPTICALLY STIMULATED LASING IN GESN

Achieving an electrically-injected group-IV laser remains the most challenging element to the full realization integrated photonics. In 2015 the first optically-pumped GeSn laser was demonstrated emitting at $\sim 2.3 \mu\text{m}$ at temperatures up to 90 K. A year later our group reported a GeSn laser emitting at $\sim 2.5 \mu\text{m}$ at temperatures up to 110 K. These are significant steps forward however they represent only a narrow operating margin in terms of emission wavelength and operating temperature. In this section we demonstrate broad lasing wavelength coverage from 2-3 μm at even higher temperatures up to 180 K. Using the growth methods described in section 4 we produced low defect density multi-layered GeSn structures that were then tested by temperature dependent PL and optical pumping measurements.

The PL measurements were performed using a standard off-axis configuration with a lock-in technique (optically chopped at 377 Hz). A continuous wave (CW) laser emitting at 532 nm wavelength was used as an excitation source. The laser beam was focused down to a 100 μm spot and the power was measured to be 100 mW. The PL emission was collected by a spectrometer and then sent to a PbS detector (cut-off at 3.0 μm , higher signal-to-noise ratio) or a InSb detector (cut-off at 5.0 μm , lower signal-to-noise ratio). The optical pumping characterization was performed using a pulsed laser operating at 1060 nm with 45 kHz repetition rate and 6 ns pulse width. The laser beam was collimated to a narrow stripe ($\sim 20 \mu\text{m}$ width and 0.3 cm length) via a cylindrical lens to

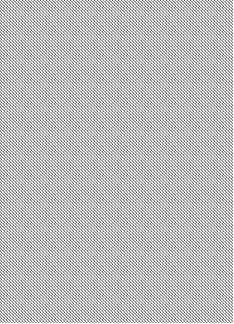
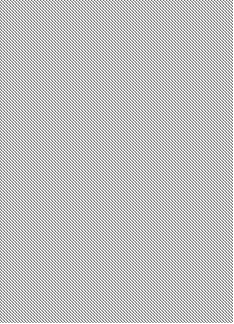
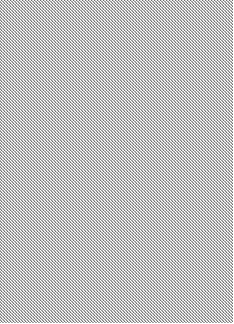
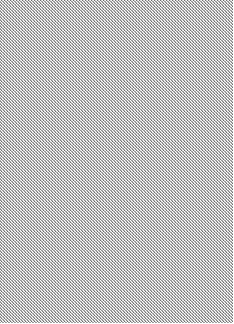
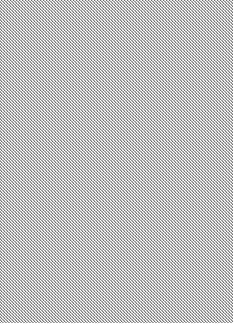
pump the GeSn waveguide structure. Since the spatial intensity profile of the laser beam features Gaussian distribution, the knife-edge technique was applied to determine the pumping power density. The device was first mounted on a Si chip carrier and then placed into a continuous flow cryostat for low temperature measurement. The emission from the facet was collected by a spectrometer and then sent to a PbS or InSb detector. The integrated emission intensity was measured by setting the grating at zero order.

Table 3 lists the samples with their respective composition, thickness, characteristic temperature, lasing wavelength, and lasing threshold [70]. To achieve Sn contents up to 17.5% the step grading growth method was used and thus for some layers there are three different compositions listed. Figure 45 shows the temperature dependent PL results for samples D and G, which both show increasing PL intensity with decreasing temperature indicating the direct nature of the band gap. Sample D shows a 12x increase in intensity and sample G a 23x increase in intensity in going from 300K to 10K. Because the wavelength of the excitation laser was 532 nm most of the light is absorbed in the first 100 nm of the layer.

An HCl: H₂O₂: H₂O=1:1:10 at 0°C etching solution was used along with standard photolithography to fabricate ridge-waveguide-based edge-emitting lasers. A facet is formed by (311) crystal plane due to the high lateral etch rate which for an etch depth of 800 nm produced a waveguide structure with 2 and 5 μm widths at the top and bottom of the ridge, respectively. After etching, the samples were lapped down to ~70 μm thickness and then cleaved to different cavity length to finish the devices. Figure 46 is a

cross-section illustration of the waveguide structure used in the optical pumping experiments [70].

TABLE 3 SUMMARY OF LASING CHARACTERISTICS

sample	GeSn 1 st layer*		GeSn 2 nd layer		GeSn 3 rd layer**		T ₀ (K)	Lasing wavelength @ 77 K (nm)	Threshold @ 77 K (kW/cm ²)
	Sn%	Thickness (nm)	Sn%	Thickness (nm)	Sn%	Thickness (nm)			
A	5.6%	210	7.3%	680			N. A.	2070	300
B	8.3%	280	9.9%	850			76	2400	117
C	9.4%	180	11.4%	660			87	2461	160
D	10.5%	250	14.4%	670			73	2627	138
E	11.6%	210	15.9%	450			N. A.	2660	267
F	9.8%	160	12.7%	680	16.6%	290	84	2767	150
G	11.9%	310	15.5%	550	17.5%	260	73	2827	171

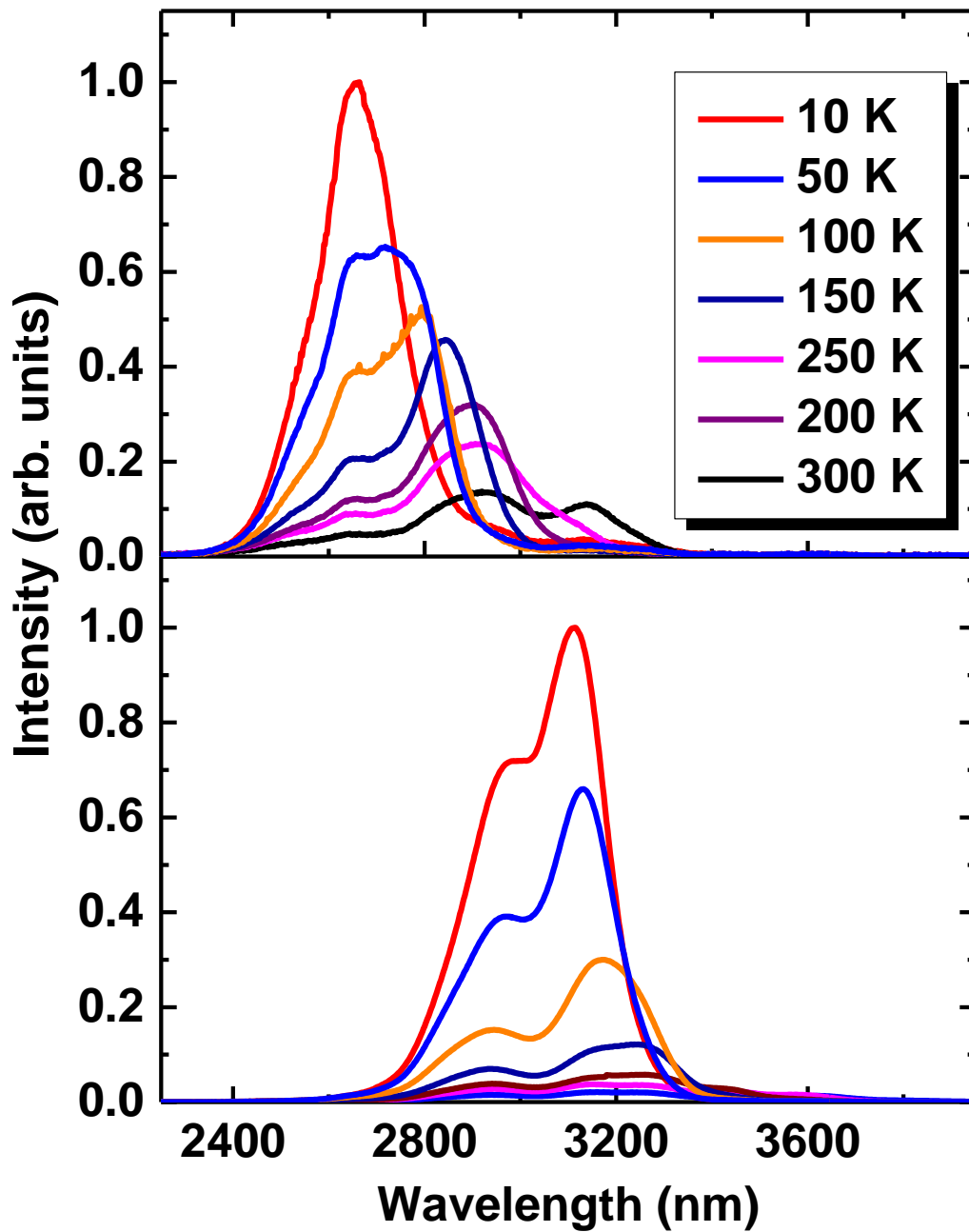


Figure 45 Temperature-dependent PL spectra of samples D and G. The dramatically increased PL intensity at lower temperature indicates the direct bandgap material nature. Inset: Integrated PL intensity. The additional valley feature appearing at $\sim 3.0 \mu\text{m}$ in all spectra is due to the water absorption.

L-L plots for samples D and G are shown in figures 47 and 48 respectively. At 77 K, the lasing thresholds for all samples ranged from 117 to 300 kW/cm², as listed in Table V. Sample A which had a Sn content of 7.3% would be expected to have the least direct band gap which may explain the relatively high lasing threshold of 300 kW/cm². Sample E also had a lasing

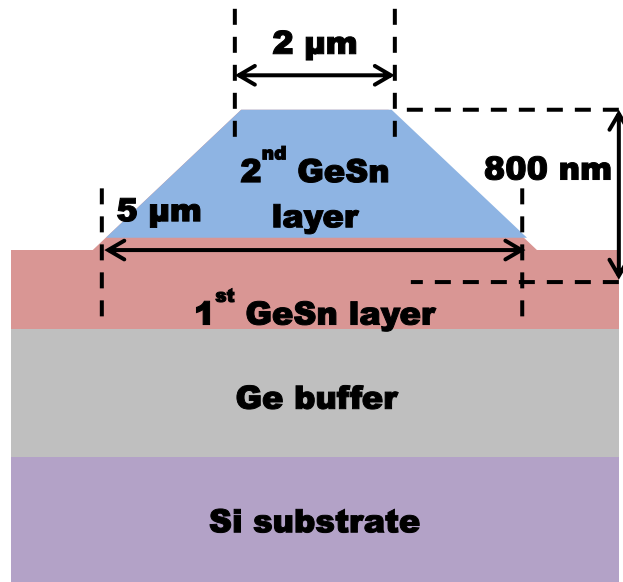


Figure 46 Cross-sectional schematic of optical pumping structures (not to scale).

threshold of 267 kW/cm² despite having a Sn content of 15.9%, the high threshold therefore may be a result of lower material quality. The remaining five samples had lasing thresholds ranging from 117 to 171 kW/cm² at 77 K. These values are substantially lower than that of our previously demonstrated GeSn laser [4] which had a threshold of

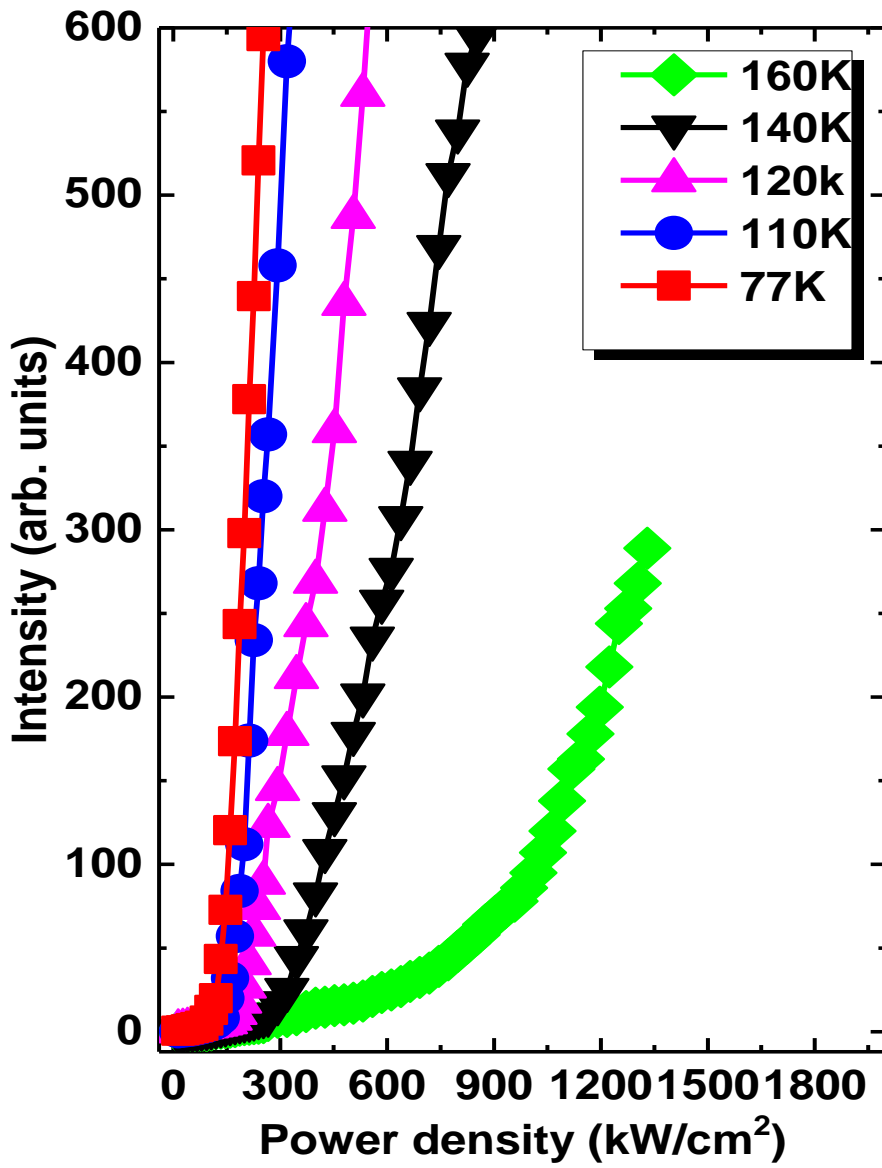


Figure 47 Sample D light output power versus pump laser power at various temperatures. Lasing was observed up to 160 K.

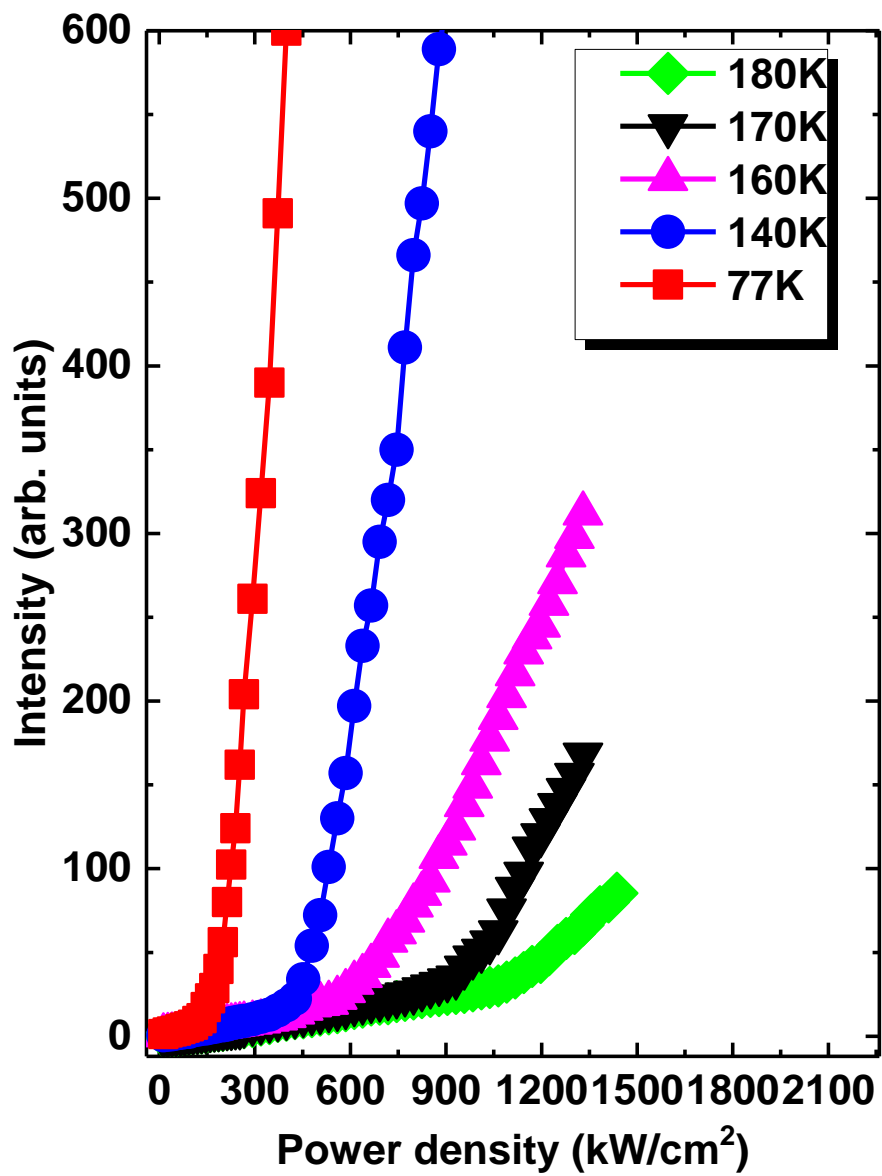


Figure 48 Sample G light output power versus pump laser power at various temperatures. Lasing was observed up to 180 K

~200 kW/cm² at 77K. Also of note are the maximum lasing temperatures of 160 K and 180 K for samples D and G respectively. Despite the high thresholds of 795 and 920 kW/cm² these are the highest lasing temperatures yet reported for GeSn. Likewise, the lasing wavelength of 2845 nm observed for sample G is a significant increase in the spectral coverage for GeSn-based lasers and indicates utility in MWIR device applications.

The characteristic temperature for each sample was extracted by temperature-dependent lasing threshold except for samples A and E due to insufficient data points, as listed in Table 3. The values ranged from 73 K to 87 K for the samples which were analyzed. Sample G is shown as an example, in figure 49 at the bottom inset with a fitted characteristic temperature of 73 K between 77 and 180 K. In comparison, the characteristic temperatures of earlier developed InP and GaAs based optically pumped lasers were reported as 100 and 129 K, respectively [71,72].

The laser emission spectra for samples A through G are summarized in figure 50. At 77 K, lasing was observed for all of the samples however upon increasing the temperature to 110 K samples A and E ceased lasing. Samples B, C, D, F, and G all continued to lase at 140 K and samples D and G lased at 160 K, finally at 180 K lasing was only observed from sample G. It is perhaps important to note that theoretical studies have predicted that 200 K should be the upper limit lasing temperature for bulk heterostructure GeSn due to dominant Auger recombination above this temperature [73].

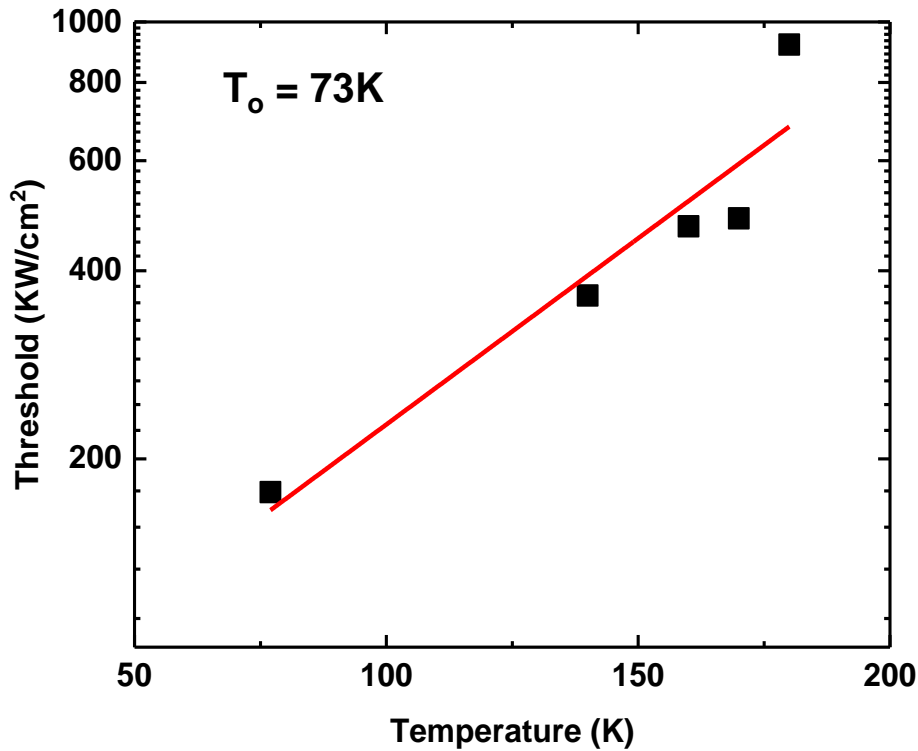


Figure 49 Plots the threshold power density vs. temperature for sample D. The characteristic temperature was extracted from the slope of the fitted line.

In figure 51 the PL spectra of samples D and G are compared to their respective Lasing spectra. There is a blue-shift in the lasing spectra of both samples however the shift is 11x greater in sample G. This blue-shift may be a result of the band filling effect, in which carriers are forced to populate higher energy levels under high injections conditions. Sample G features a larger blue-shift relative to sample D. This is mainly due to the thinner GeSn top layer of sample G (3rd GeSn layer of 260 nm) compared to that of sample D (2nd GeSn layer of 670 nm). The thinner active region would force injected carriers to populate higher energy states resulting in shorter wavelength emission.

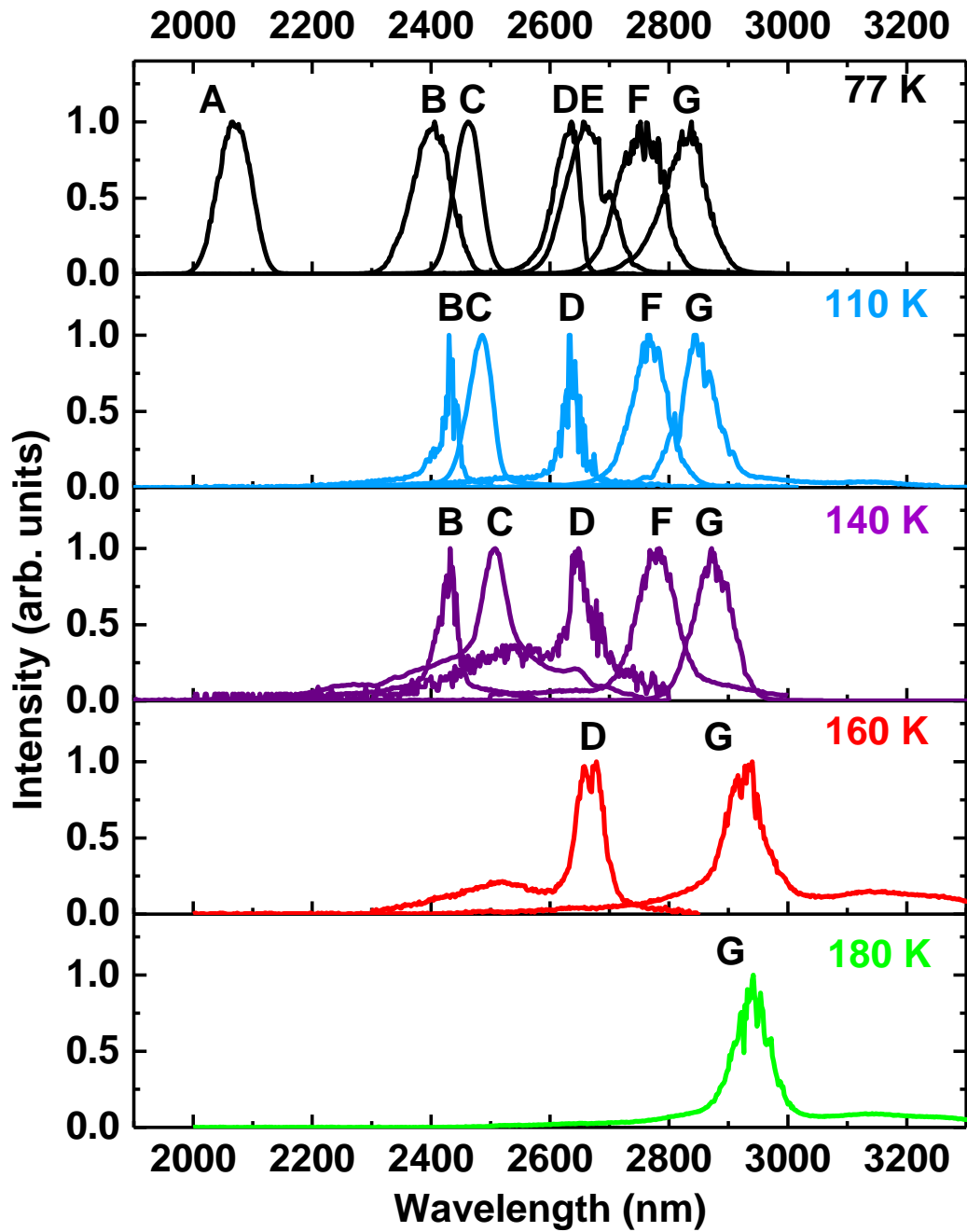


Figure 50 GeSn laser performance characterization. a, Spectra of GeSn lasers fabricated from samples A to G at temperatures from 77 to 180 K

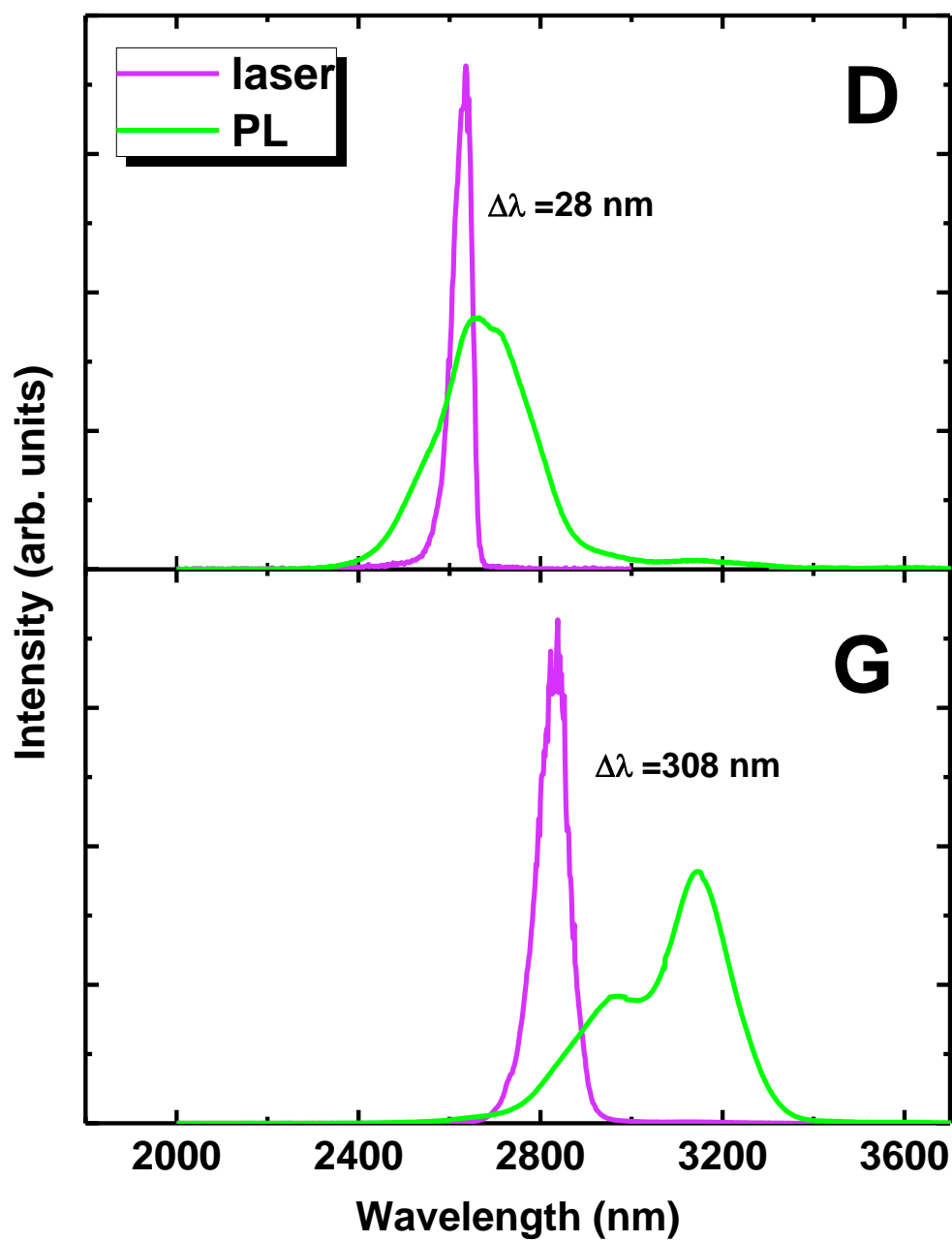


Figure 51 Lasing spectra of samples D and G at 77 K of samples compared with those PL spectra. The lasing peak blue-shift is due to the typical band filling effect.

CHAPTER 8

QUANTUM WELL STRUCTURES

The realization of an electrically injected GeSn-based laser will require the use of doped heterostructures. Theoretical calculations predict that bulk heterostructures will have a large Auger recombination component and would inhibit lasing except for at low temperatures [73]. The Auger process can be suppressed through the use of quantum wells owing to their lower density of states, however the thin active region of QW's reduces the confinement factor and modal gain. Therefore multiple quantum wells should be used to increase the modal gain of the structure [73]. Central to the design of MQW's is determining the materials compositions of the barrier and well layers which will result in type-I alignment. It is necessary that the well(s) have a direct bandgap as this is where electron-hole recombination takes place therefore the Sn-composition must be maximized and the compressive strain must be minimized. Interfacial abruptness is also an essential characteristic of MQW structures, but this has proved difficult to realize in practice. Here we present the results of our initial GeSn and SiGeSn QW development. These structures were grown strained to the Ge buffer and thus lack a direct band gap in the well region. None the less these are useful in developing an understanding of the challenges unique to design, growth, and characterization of Si-Ge-Sn QW's.

8.1 $\text{Ge}_{0.95}\text{Sn}_{0.05}/\text{Ge}_{0.9}\text{Sn}_{0.1}/\text{Ge}_{0.95}\text{Sn}_{0.05}$ QUANTUM WELLS

It is of the utmost importance to demonstrate abrupt interfacial composition control for successful QW-based devices. The tendency for Sn atoms to segregate from regions of higher Sn to regions of lower Sn makes this challenging from a fundamental materials science perspective. Segregation and interdiffusion can be limited by minimizing the growth temperature and careful control of the surface chemistry. From an engineering perspective interfacial control requires that precursor gases can be switched on and turned off rapidly, and that residual gas can be quickly pumped out of the reactor volume. Our QW growth development was started with a relatively simple structure consisting of $\text{Ge}_{0.95}\text{Sn}_{0.05}/\text{Ge}_{0.9}\text{Sn}_{0.1}/\text{Ge}_{0.95}\text{Sn}_{0.05}$ to identify the primary challenges before moving to more complicated structures.

The first barrier layer $\text{Ge}_{0.95}\text{Sn}_{0.05}$ is grown at 320°C at a molar flow ratio ($\text{SnCl}_4/\text{GeH}_4$) of $\dot{M} = 0.009$ targeting 30 nm. The reactor is continuously purged with 15 slm of H_2 gas to ensure the deposition precursors move quickly through the chamber volume. After completion of the first barrier the temperature is ramped to 290°C in 15 slm H_2 and the deposition gases are directed to the vent/exhaust while the temperature stabilizes. During this time the molar flow ratio is increased to $\dot{M} = 0.012$ and allowed to stabilize, once flow and temperature have stabilized the deposition gases are redirected into the chamber volume for growth of the 10 nm $\text{Ge}_{0.9}\text{Sn}_{0.1}$ well region. The deposition gases are then switched back to vent/exhaust and the temperature and flows are ramped back to 320°C and $\dot{M} = 0.009$ and after stabilization the second $\text{Ge}_{0.95}\text{Sn}_{0.05}$ barrier layer is grown. Ideally the structure would be grown isothermally however due to the strong

influence of temperature on composition achieving such a difference in well and barrier compositions requires growth a high and low temperature. Finally a Ge passivation cap is deposited at 320°C targeting 150 nm.

The SIMS depth-profile and TEM cross-section of this structure are shown in figures 52 (a) and (b) respectively. From these figures we observe a Ge layer ~ 9-10 nm thick in between the well and second barrier that was not intended to be part of the structure. There is also an apparent increase in Ge and decrease in Sn at the interface of the first barrier and well. These are obviously not a desired features and we address the source and solution to this issue is discussed further later in this section.

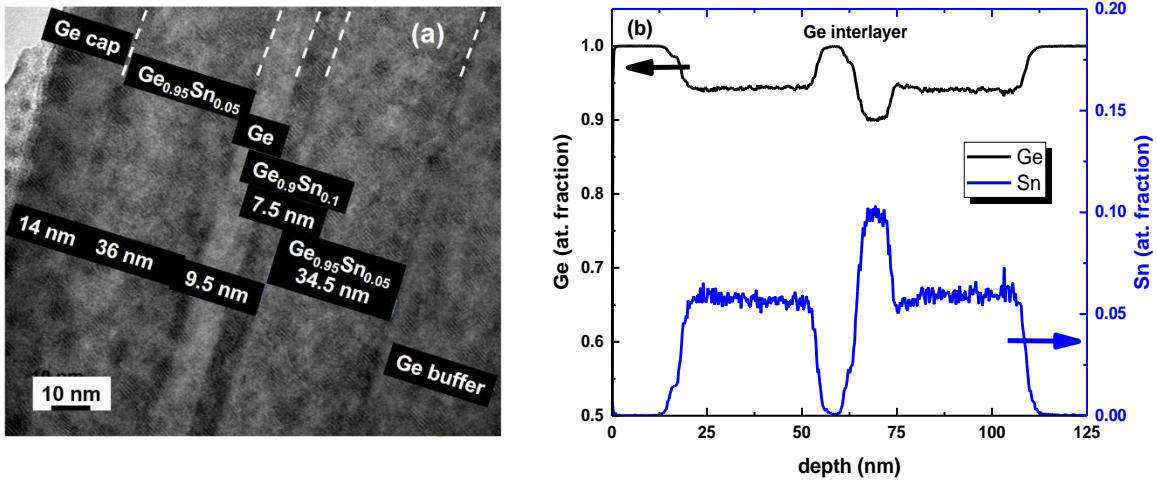


Figure 52(a) shows a cross-sectional TEM of a $\text{Ge}_{0.95}\text{Sn}_{0.05}/\text{Ge}_{0.9}\text{Sn}_{0.1}/\text{Ge}_{0.95}\text{Sn}_{0.05}$ structure. 52(b) is a SIMS depth profile of this same sample the Ge interlayer can be seen in both TEM and SIMS [32].

The GeSn/GeSn QW was further analyzed by XRD-RSM to determine the layer strain and calculate the theoretical band diagram and band offsets. In figures 53 the (224) XRD-RSM is shown and based on the interference fringes appear to have excellent

structural quality. It is apparent that the QW, barriers, and Ge buffer are aligned in $a_{//}$ indicating they are fully strained to the Ge-buffer. The strain and compositions determined by XRD RSM are summarized in table 4 [74]. Using these values the band-offsets and sub-band energy levels were calculated using the effective mass

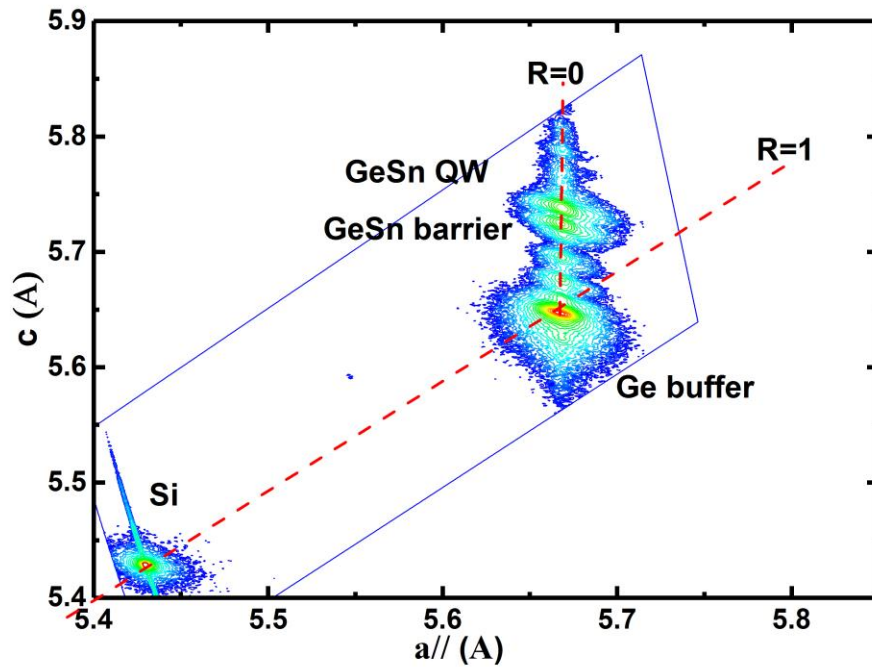


Figure 53 XRD-RSM in shows the well (9.16% Sn) and barriers (4.85% Sn) are fully strained to the Ge-buffer. There are also fringes observed in between the Ge buffer and barriers and on the far side of QW, this indicates smooth interfaces and high structural quality.

Table 4 SUMMARY OF QW STRAIN AND BAND OFFSETS

Structure	GeSn/GeSn QW			
	Thickness (nm)	Si (%)	Sn (%)	Strain (%)
Cap	14	0	0	0.01
Barrier	36	0	4.8	-0.84
Well	7.5	0	9.1	-1.39

Sample	$\Delta E_{c\Gamma}$ (meV)	ΔE_{cL} (meV)	ΔE_{vHH} (meV)	ΔE_{vLH} (meV)	$\Delta E_{\Gamma-1HH}$ (meV)	ΔE_{1L-1HH} (meV)	$\Delta E_g = E_{g\Gamma} - E_{gL}$ (meV)
A	76	15	36	5	590	527	18

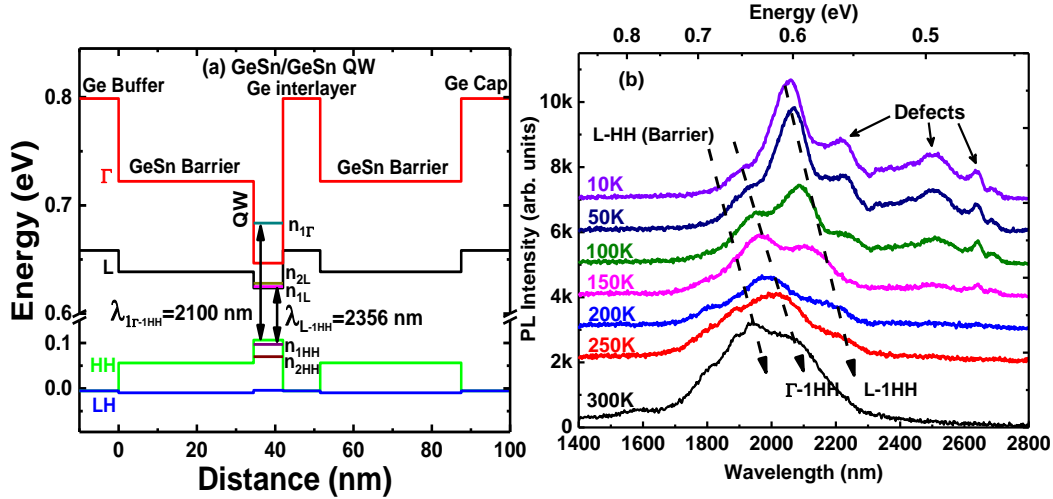


Figure 54(a) plots the calculated band alignment and the energy sub-band levels for the Ge_{0.95}Sn_{0.05}/Ge_{0.9}Sn_{0.1}/Ge_{0.95}Sn_{0.05} with the Ge interlayer. 54(b) shows the temperature dependent PL for the same sample from 10K-300K [74].

approximation and the 6 band K·P methods for the conduction and valence bands, respectively. The calculations predict type-I band alignment so that electrons and holes are confined to the well with strong wavefunction overlap. The band alignments are illustrated in figure 54(a). Temperature dependent photoluminescence studies were done on the structure from 10K to room temperature with the results shown in figure 54(b). At room temperature there are two peaks observed at ~1950 nm and ~ 2100 nm. The former is attributed to the indirect bandgap transition in GeSn barrier region however the

intensity decreases with temperature as the excess carriers preferentially populate the well region. The peak at 2100 nm most likely corresponds to the $n_{1\Gamma}$ - n_{1HH} transition in the GeSn well region. The n_{1L} - n_{1HH} transition is weak at 300 K because the vast majority of carriers in the L-valley recombine via Shockley-Read-Hall (SRH) non-radiative process before the occurrence of inefficient radiative recombination. Once temperature decreases, the indirect transition PL peak attributed to n_{1L} - n_{1HH} transition of GeSn well region is shown. In low temperatures, thermal energy (i.e. $KT \sim 1\text{meV}@10\text{K}$) is lower than the barrier height of the L-valley. Therefore, carriers are confined at the L-valley ground state of the GeSn QW. This behavior is characteristic of the indirect nature of the QW band gap, which is not desirable for light emitting devices. It is therefore essential that the Sn composition be increased and the compressive strain be reduced in order to realize optimum QW performance.

8.2 $\text{Si}_{0.05}\text{Ge}_{0.95}\text{Sn}_{0.05}/\text{Ge}_{0.9}\text{Sn}_{0.1}/\text{Si}_{0.05}\text{Ge}_{0.95}\text{Sn}_{0.05}$ QUANTUM WELLS

SiGeSn alloys offer additional flexibility as QW barrier layers because the band gap /band offsets can be tuned independently. The larger band gap of SiGeSn relative to GeSn should allow superior carrier confinement in the QW region. Not unexpectedly there are somewhat similar issues with compositional control with the ternary barrier-layer materials however there is the added complication of a third deposition precursor. The growth of the second barrier-layer on the Sn-rich QW surface results in reduced growth rate and reduced silicon composition for the same growth conditions. This produces a compositionally asymmetric QW structure, however there is no Ge-interlayer formation observed at the interface of the QW and the second barrier layer. We delay a

detailed discussion of the surface/interface chemistry until section 7.3 and here we discuss the characterization results of our first attempts at SiGeSn/GeSn QW's which produced promising results.

The (224) XRD-RSM is shown in figure 55 show strong interference fringes. We can see that the QW, barriers, and Ge buffer are aligned in $a_{//}$ indicating this is a fully strained structure. The strain and compositions for each layer determined by XRD-RSM are listed in table 5 and the calculated band offsets are listed in table V.B and illustrated in figure 56(a). The strain values in each layer closely match those of the corresponding layers in the GeSn/GeSn version of QW and as expected the offsets at $E_{c\Gamma}$, E_{cL} , E_{vHH} , and E_{vLH} are larger than GeSn/GeSn version of the QW. The sub-band energy levels are also similar between the two structures and in figure 56(b) we observe two peaks at ~ 1950 nm and ~ 2100 nm corresponding to the $n_{1\Gamma} - n_{1HH}$ and $n_{1L} - n_{1HH}$ transitions respectively. At 300K the L1-HH transition is weak due to the low barrier energy of 13 meV which allows carriers to thermally depopulate the L1 sub-band. There is only a 41 meV energy separation between the L1 and $\Gamma 1$ levels so that at high temperature electrons can be excited into $\Gamma 1$ where radiative recombination is much more efficient. The $\Gamma 1$ -HH transition therefore dominates the PL spectra at $T > 150K$ however as the temperature decreases the electrons are confined to the L1 level and the L1-HH transition becomes the primary feature of the spectra. From the band diagram it is also seen that the $\Gamma 1$ level is higher in energy than the L-valley minima in the SiGeSn barriers. This allows electrons in that sub-band to spill into the barrier thereby reducing the radiative recombination rate in the QW, thus this particular design is not optimum

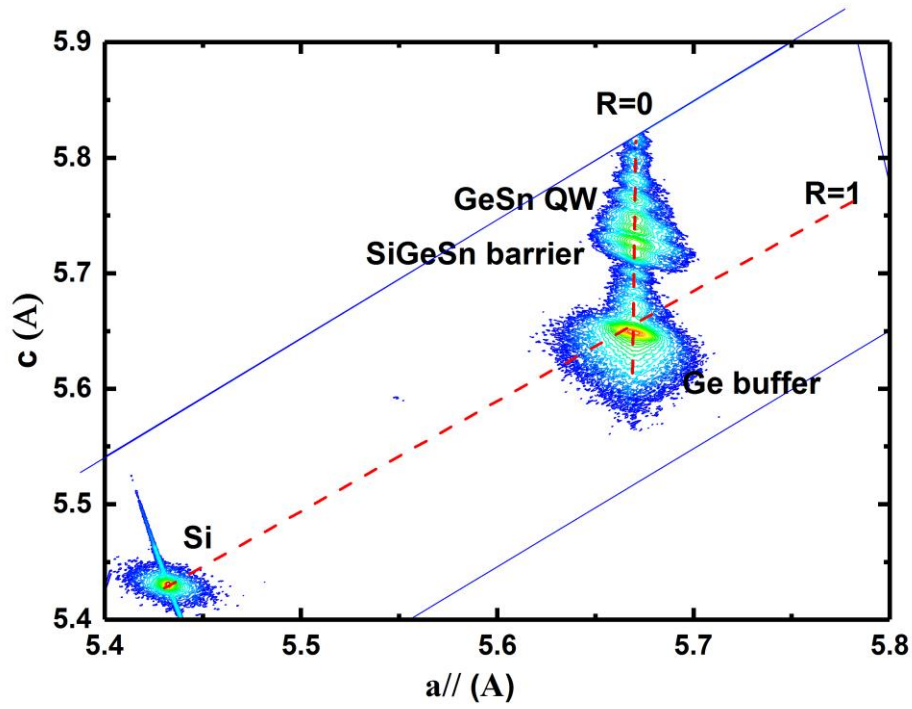


Figure 55 shows the XRD-RSM on the $\text{Si}_{0.05}\text{Ge}_{0.95}\text{Sn}_{0.05}/\text{Ge}_{0.9}\text{Sn}_{0.1}/\text{Si}_{0.05}\text{Ge}_{0.95}\text{Sn}_{0.05}$ sample. All of the layers align along the red dashed line at $R = 0$ indicating fully strained QW layers.

Table 5 SUMMARY OF QW STRAIN AND BAND OFFSETS

Structure	SiGeSn/GeSn QW			
	Thickness (nm)	Si (%)	Sn (%)	Strain (%)
Cap	10	0	0	0.01
Barrier	42	12	9	-0.82
Well	11	0	9.1	-1.38
Barrier	44.5	12	8.2	-0.70
Buffer	700	0	0	0.01

Sample	$\Delta E_{c\Gamma}$ (meV)	ΔE_{cL} (meV)	ΔE_{vHH} (meV)	ΔE_{vLH} (meV)	$\Delta E_{1\Gamma-1HH}$ (meV)	ΔE_{1L-1HH} (meV)	$\Delta E_g = E_{g\Gamma} - E_{gL}$ (meV)
B	287	13	80	34	584	543	8

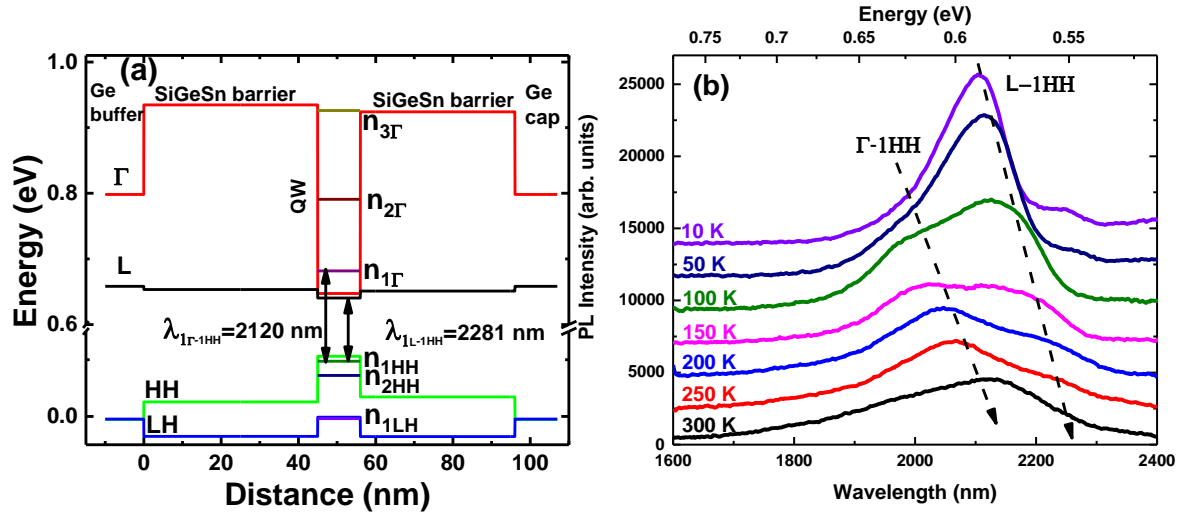


Figure 56 (a) plots the calculated band alignment and the energy sub-band levels for the $\text{Si}_{0.05}\text{Ge}_{0.95}\text{Sn}_{0.05}/\text{Ge}_{0.9}\text{Sn}_{0.1}/\text{Si}_{0.05}\text{Ge}_{0.95}\text{Sn}_{0.05}$ with the Ge interlayer. 56(b) shows the temperature dependent PL for the same sample from 10K-300K [74].

8.3 INTERFACIAL COMPOSITION CONTROL IN QUANTUM WELLS

In order to eliminate these unwanted interfacial profiles the growth sequence was first carefully examined for a possible stagnant gas or thermal cause that could be eliminated with an engineering solution. In one experiment the flows were kept the same as described above however there was no temperature ramping in between steps. Without the temperature ramping the delay between deposition of layers 1, 2, and 3 was eliminated. A second test was run in which the H_2 carrier flow was increased to 20 slm, this was done to increase the gas velocity across the wafer. SIMS on these test structures revealed that the Ge inter-layer remained with no meaningful change in thickness. Additionally we see from figure 52(b) that the Ge-enrichment increases as the Sn content on the starting surface increases. There is a small increase in the Ge content at the interface of the first barrier and well during the transition from a 5% Sn layer to a 10% Sn

layer. However when transitioning from 10% Sn layer to a 5% Sn layer in the second barrier, a completely separate Ge layer is formed. This indicates that the source of the inter-layer formation is likely something more fundamental and related to the surface chemistry.

The cause can be explained both kinetically and energetically. In section 3.1 we have discussed the growth kinetics and chemistry and we found that Ge incorporation rate increases as $\sim [GeH_4]\theta^n$ where $n > 1$, whereas Sn only increases as $\sim [SnCl_4]\theta$. Or in other words, a higher availability of open surface sites increase the initial Ge incorporation efficiency relative to that of Sn. Additionally the desorption/etching of surface $SnCl_2$ can lead to delays in attaining adsorption equilibrium. This is again due to the reaction pathways which govern the growth, the $SnCl_4$ molecule undergoes multiple intermediate gas-phase reactions and is already partially dissociated during adsorption. GeH_4 on the other hand arrives at the surface primarily in-tact and therefore must dissociatively adsorb on multiple sites. The Sn-enriched surface will have a larger θ due to weaker H and Cl bonding therefore during the initial injection of precursors GeH_4 achieves a more rapid adsorption equilibrium than $SnCl_4$. In energetic terms the Sn surface sites may have lower adsorption barriers due to the local strain of Ge-Sn surface dimers. Theoretical calculations by Cheng et. al. indicate that GeH_4 has lower adsorption energy barriers on the strained SiGe (100) surfaces than the Ge (100) surface [75]. Although this work did not include adsorption specifically on GeSn surfaces it did show generally that compressive strain made surface adsorption sites more reactive. Since $SnCl_4$ is already partially dissociated in the gas-phase this increased surface reactivity

would have only minor impact on Sn-incorporation but a large impact on Ge-incorporation, which allows the interlayer formation.

To compensate for this effect the SnCl_4 flow can be set to a higher flow during the initial gas injection for the second barrier layer growth. The SnCl_4 flow is then ramped back down to the target value over a 10-20 second time period. Figure 57 is a SIMS depth profile of two QW structures, the first was grown using the flow compensated version of the recipe and the second was grown with no flow compensation. Figure 58 compares simplified versions of the structure of the uncompensated and compensated growth recipes to illustrate how the precursor flows and temperatures are changed.

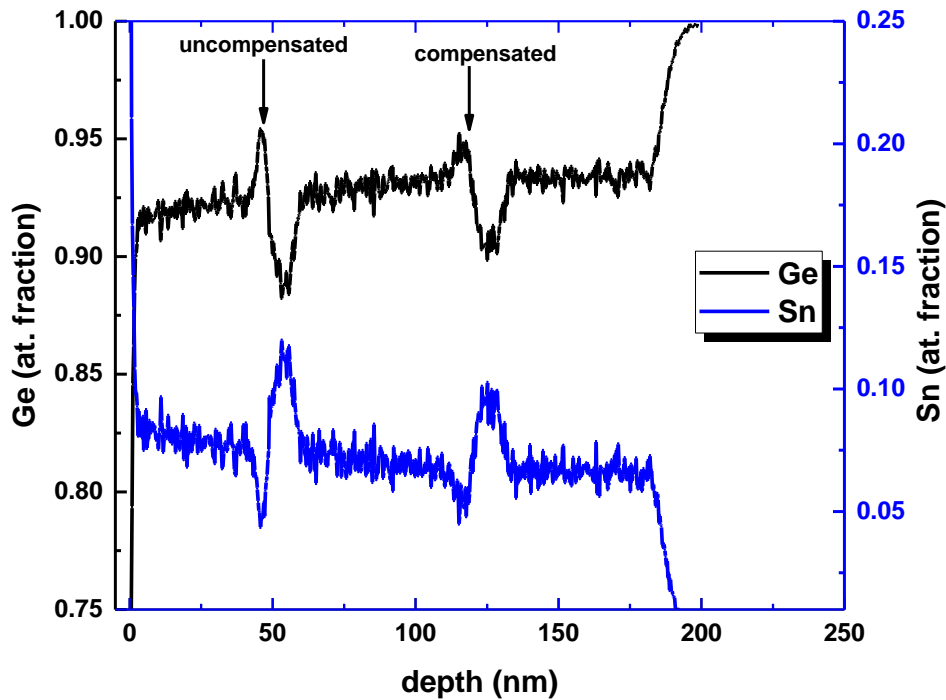


Figure 57 plots the SIMS depth profile of two $\text{Ge}_{0.95}\text{Sn}_{0.05}/\text{Ge}_{0.9}\text{Sn}_{0.1}/\text{Ge}_{0.95}\text{Sn}_{0.05}$ QW's. The first was flow compensated and the second is the uncompensated control

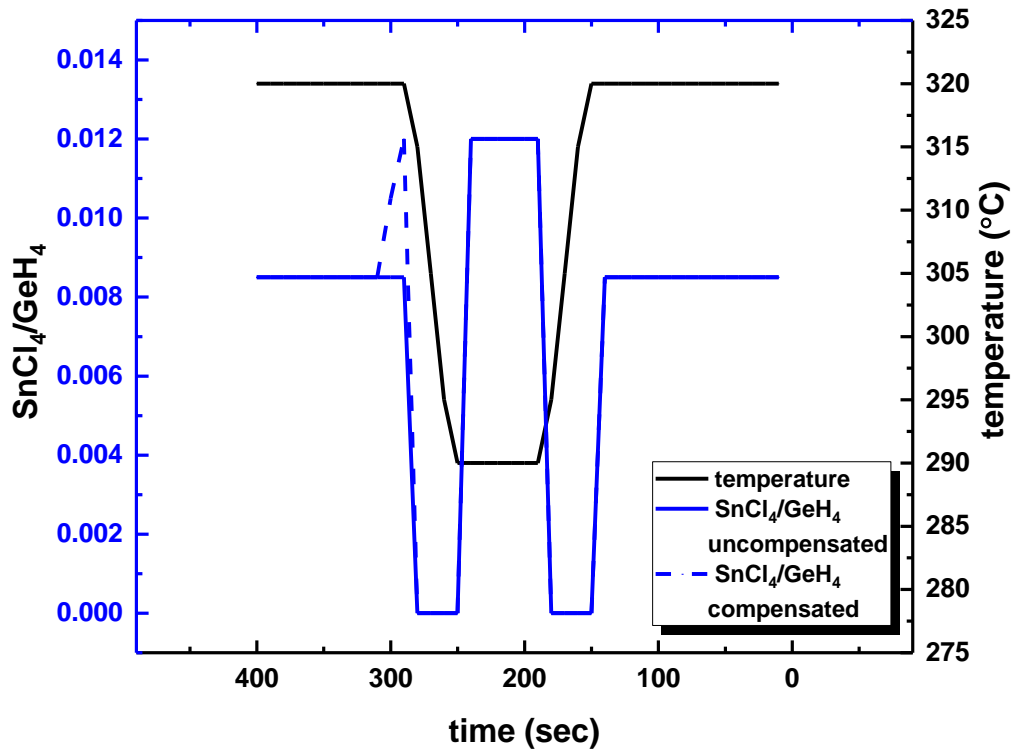


Figure 58 Outlines the temperature and flow during the course of the $\text{Ge}_{0.95}\text{Sn}_{0.05}/\text{Ge}_{0.9}\text{Sn}_{0.1}/\text{Ge}_{0.95}\text{Sn}_{0.05}$ compensated and uncompensated QW's. The temperature is the same for both recipes however the flow is shown as a dashed and solid lines for the compensated and uncompensated recipes, respectively.

uncompensated version. It is evident from this SIMS profile that the Ge-interlayer thickness can be reduced using this method. The increased SnCl_4 flow during the initial injection into the reaction chamber partially compensates for the initial kinetic advantage of the GeH_4 . SnCl_4 eventually achieves kinetic balance with GeH_4 and the flow can be ramped back down to the target value.

Interfacial composition control in $\text{SiGeSn}/\text{GeSn}/\text{SiGeSn}$ QW's is easier to achieve. There is still a slight Ge-enrichment at the interface of the QW and second barrier layer but there is no interlayer formation. The main challenge for these structures is in achieving symmetric barrier layers on either side of the QW. For the same SiH_4 ,

GeH₄, and SnCl₄ flows, and same growth time and temperature the second barrier layer has a different composition and thickness. A summary of the growth conditions and the SIMS results can be found in table 6 and figure 59. It is apparent that there is a difference in the growth kinetics for the Sn-rich starting surface of the QW. On the Sn- rich surface the Si incorporation decreases, the Ge incorporation increases, and the growth rate is reduced. This is a result of competitive adsorption between the GeH₄ and SiH₄, both precursors are stable in the gas-phase and therefore must undergo dissociative adsorption. Both have adsorption rates $\sim \theta^n$ where $n > 1$, and therefore both require multiple open surface sites. The Sn-rich surface will create a higher a density of adsorption sites however GeH₄ will have a higher efficiency due the lower Ge-H bond energy. The theoretical work in reference [75] indicates that GeH₄ should have a lower adsorption

Table 6 SUMMARY OF BARRIER LAYER ASYMMETRY

layer	Temperature (°C)	Time (min)	SnCl ₄ /GeH ₄	SiH ₄ /GeH ₄
Barrier 1	320	5	0.0085	0.4
Barrier 2	320	5	0.0085	0.4

layer	SIMS results			
	Thickness (nm)	Si (%)	Sn (%)	Ge (%)
Barrier 1	60	4.4	6.6	0.89
Barrier 2	44	3.5	6.6	0.90

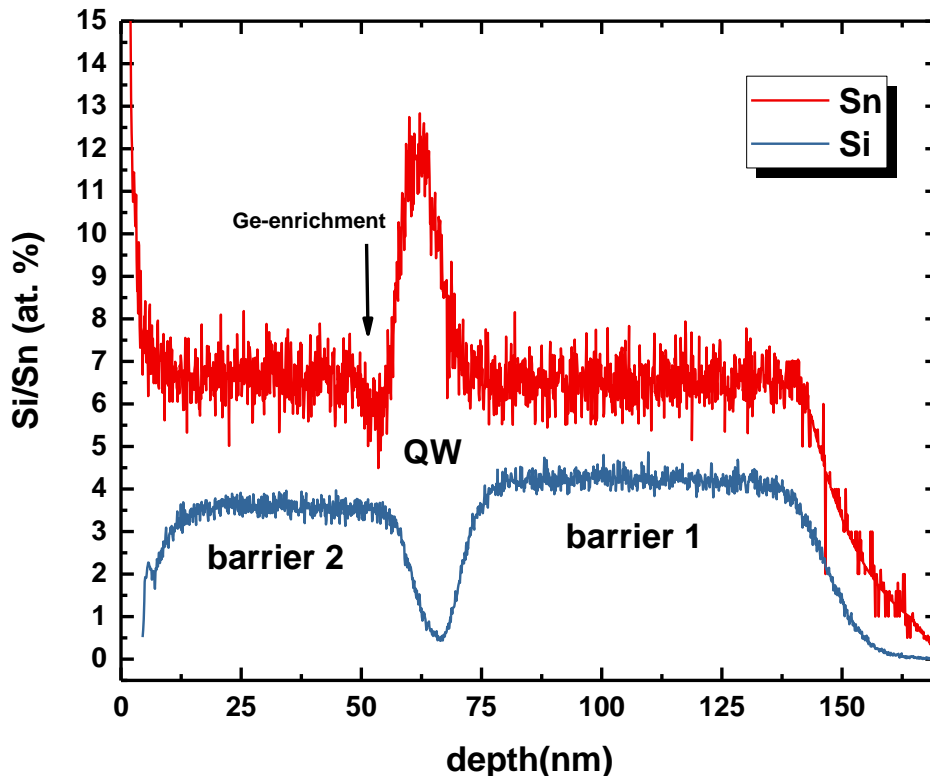


Figure 59 Plots the SIMS depth profile of a SiGeSn/GeSn QW. The conditions for both SiGeSn barriers were identical however the 2nd barrier shows a lower Si composition and growth rate.

energy barrier than SiH_4 for Ge (100) and SiGe (100) surfaces. The increased compressive strain in the GeSn QW which we have discussed would even further increase the reactivity of GeH_4 relative to SiH_4 . The end result of these effects is that Ge wins the competition for available surface sites and shifts the composition, however this competition also has a benefit. We have mentioned that there is no Ge interlayer formation which may be the result of this competition between SiH_4 and GeH_4 . In binary GeSn growth the SnCl_4 and GeH_4 do not compete in the same way due to the gas-phase dissociation of SnCl_4 . Therefore the reactivity of GeH_4 on the Sn-rich surface is

unhindered whereas in the ternary growth the GeH_4 reactivity is buffered by SiH_4 . In the former case a complete Ge-interlayer can be formed where in the latter case only Ge-enrichment is allowed. The problem of barrier asymmetry is easily fixed by increasing the SiH_4 flow and the growth time on the second barrier. The Ge-enrichment can be eliminated by similarly introducing a higher SnCl_4 flow during the initial gas injection and then ramping back to the target flow.

8.4 MULTIPLE QUANTUM WELLS ON STRAIN-RELAXED BUFFER LAYERS

With interfacial control established the next step will be to take this learning on to our strain relaxed platform presented in section 4. Strain-relaxation will allow access to previously forbidden Sn compositions in the well and facilitate more favorable band alignment. It is important that the GeSn QW have a direct or nearly-direct band gap which for most Sn-compositions requires growth on a strain-relaxed GeSn-buffer. In terms of photonic application multiple quantum wells are often desired. However for the reasons discussed at the introduction of this chapter GeSn should especially benefit from the use of MQW's.

Figure 60 is a SIMS depth profile of a $4x \text{Si}_{0.03}\text{Ge}_{0.9}\text{Sn}_{0.07}/\text{Ge}_{0.86}\text{Sn}_{0.14}$ MQW on a strain-relaxed $\text{Ge}_{0.91}\text{Sn}_{0.09}$ buffer layer. A cross-sectional TEM image is shown in in figure 61, both the SIMS and TEM show the abrupt interfaces of the barrier/well regions. Based on the XRD-RSM shown in figure 62 the GeSn buffer is 74% relaxed such that starting lattice constant, a , for the MQW structure is 5.719 \AA . The relaxed buffer layer allows Sn contents of 14% in the QW region and these layers are only under 0.88 %

compressive strain. As a comparison, a 14% QW layer grown lattice matched to the Ge-buffer with starting $a = 5.66 \text{ \AA}$ would be under 1.8% compressive strain, the reduced strain should the material more direct band gap. The strain calculated from the XRD-RSM is summarized for each layer in table VII.

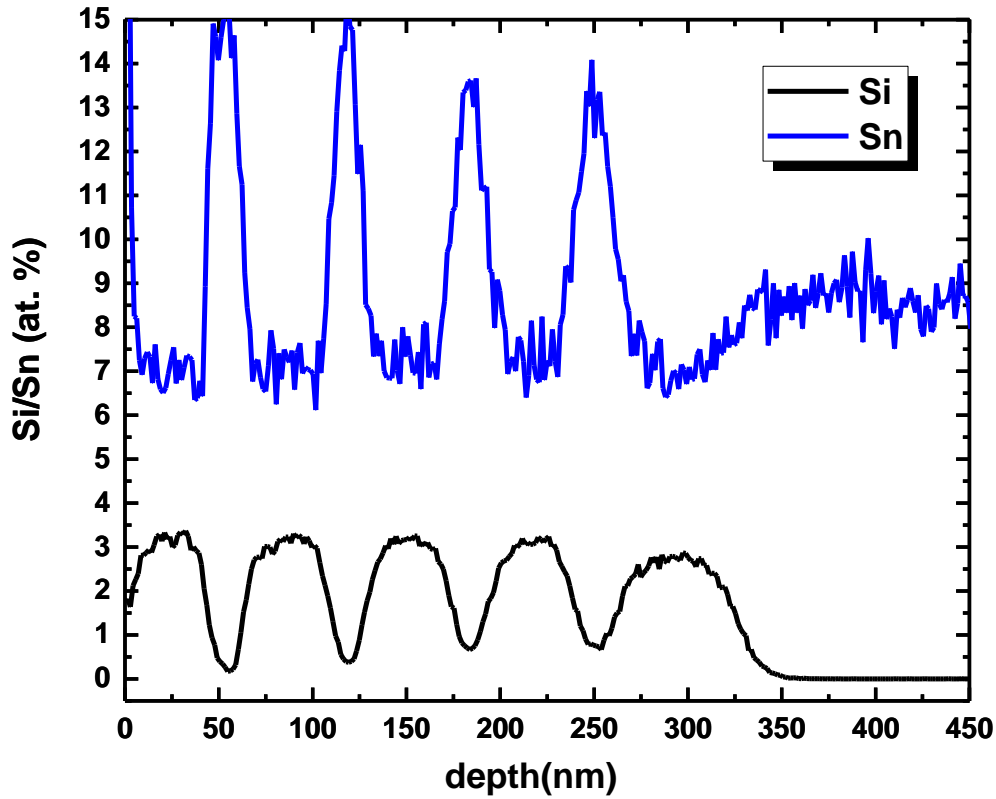


Figure 60 is a SIMS depth profile of a 4x $\text{Si}_{0.03}\text{Ge}_{0.9}\text{Sn}_{0.07}/\text{Ge}_{0.86}\text{Sn}_{0.14}$ MQW on a strain-relaxed $\text{Ge}_{0.91}\text{Sn}_{0.09}$ buffer layer.

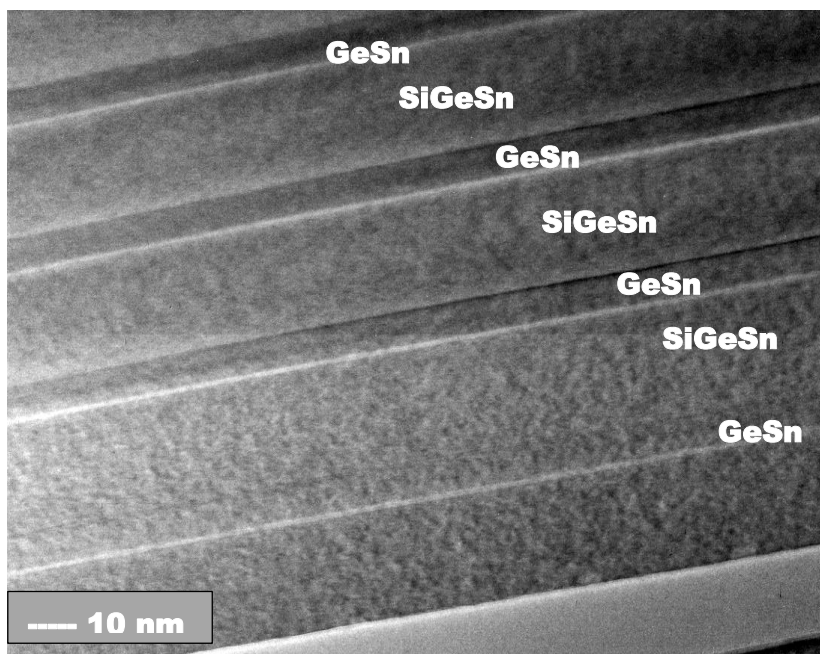


Figure 61 Cross-sectional TEM of the 4x $\text{Si}_{0.03}\text{Ge}_{0.9}\text{Sn}_{0.07}/\text{Ge}_{0.86}\text{Sn}_{0.14}$ MQW.

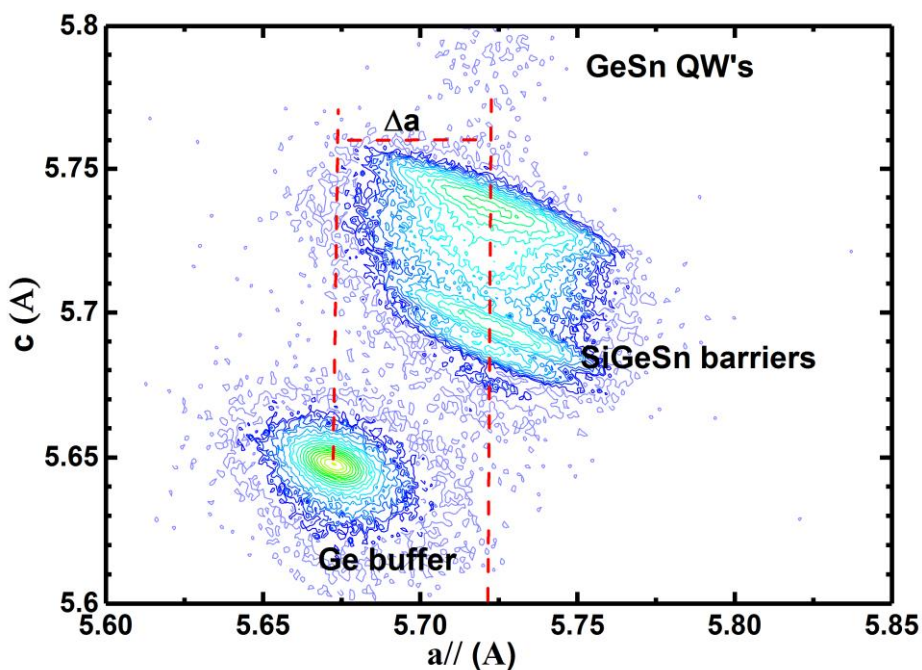


Figure 62 Lattice space map of 4x $\text{Si}_{0.03}\text{Ge}_{0.9}\text{Sn}_{0.07}/\text{Ge}_{0.86}\text{Sn}_{0.14}$ MQW on a strain-relaxed $\text{Ge}_{0.91}\text{Sn}_{0.09}$ buffer layer. The dashed lines show the shift in the in plane lattice constant which was made possible by growing on a strain-relaxed GeSn buffer instead of a Ge-buffer

The calculated band diagram is shown in figure 63 indicates the QW regions are direct band gap. There is a $\Delta E_g = -140$ meV between the direct (Γ) and indirect (L) valley. This is an improvement over previous SiGeSn/GeSn QW structures which had $\Delta E_g = +8$ meV. The conduction sub-band $n_1\Gamma$ is shown at 0.53 eV and the temperature dependent PL in figure 64 reveals a strong intensity peaks at 2585 nm/0.48 eV and 2645 nm/0.47 eV for 10K and 80K respectively. The PL emission energy most closely matches the $n_1\Gamma \rightarrow E_v(lh)$ transition which from the band diagram calculation is 0.47 eV. Optical pumping was done with a 1054 nm laser at 2 mW, the cavities were fabricated in the same way as described in chapter 7. The optical pumping results in a decrease in the peak FWHM

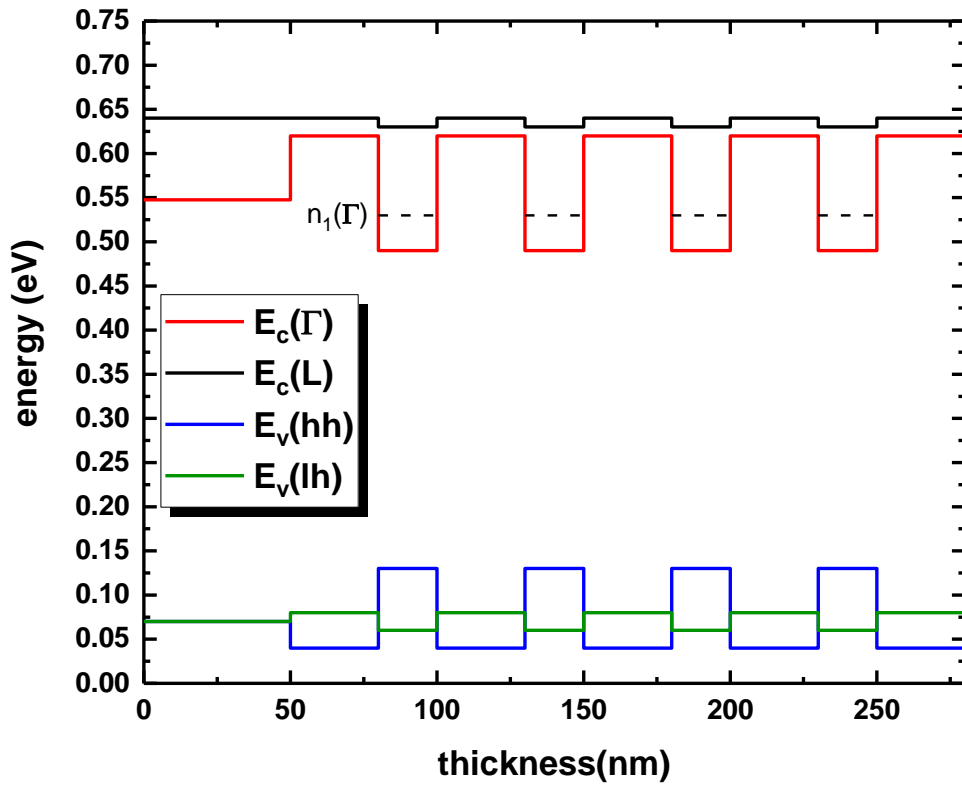


Figure 63 Plots the band diagram for the 4x $\text{Si}_{0.03}\text{Ge}_{0.9}\text{Sn}_{0.07}/\text{Ge}_{0.86}\text{Sn}_{0.14}$ MQW

which is indicative of lasing. The output intensity is measured as a function of optical pumping power in the L-L curve shown in figure 65, the lasing threshold is seen at 33, 44, and 127 kW/cm² for 10, 40, and 80K respectively. This is a significant advance in GeSn-based photonic devices and up to this point lasing from SiGeSn/GeSn QW's has not been published.

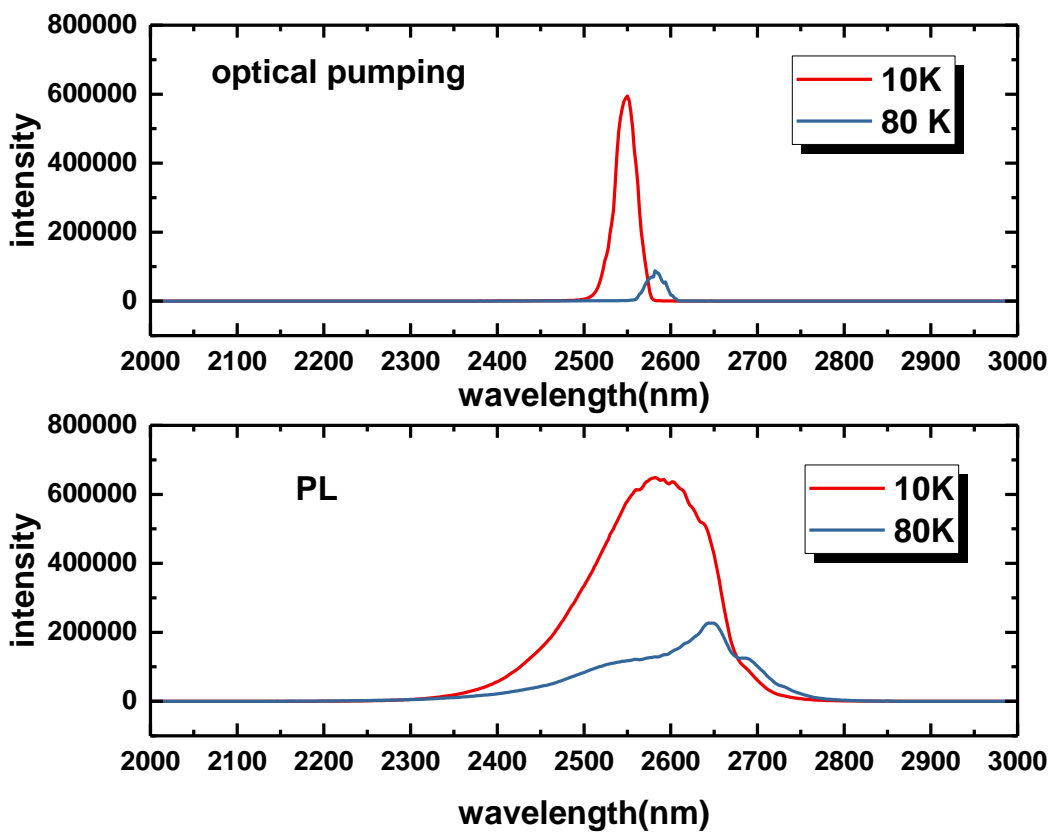


Figure 64 compares optical pumping (top) and PL (bottom) at 10K and 80K for the 4x Si_{0.03}Ge_{0.9}Sn_{0.07}/Ge_{0.86}Sn_{0.14} MQW

Table 7 SUMMARY OF MQW STRAIN

Structure	SiGeSn/GeSn QW			
	Thickness (nm)	Si (%)	Sn (%)	Strain (%)
GeSn buffer	700	0	9	-0.17
SiGeSn Barrier	35	3	7	-0.36
Well	17	0	14	-0.88

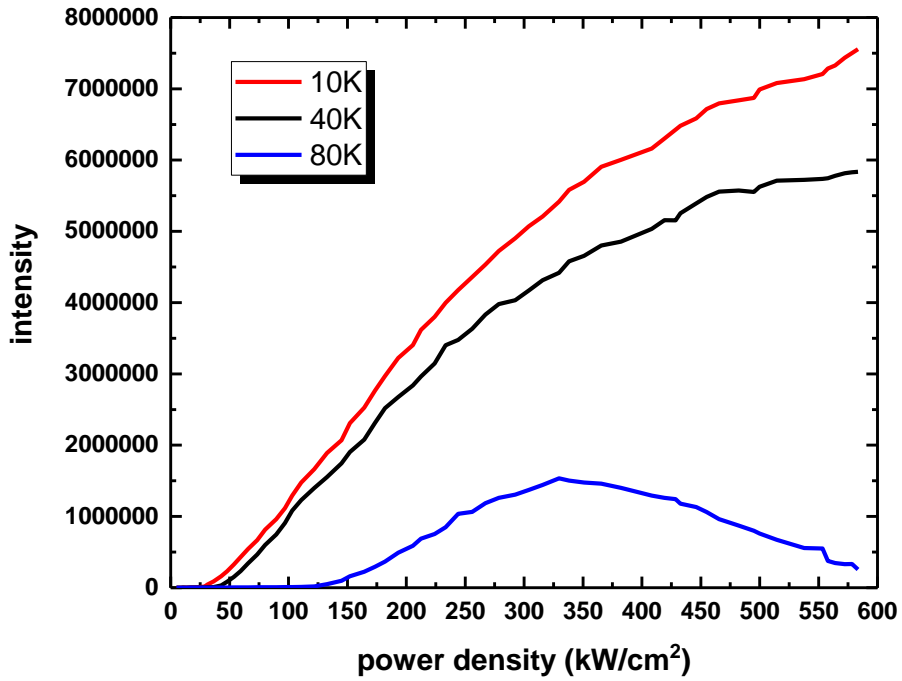


Figure 65 plots the L-L output for the MQW at 10,40,and 80K. Threshold power densities were 33, 44, and 127 kW/cm^2 for 10, 40, and 80K respectively

CONCLUSIONS

In this work we have discussed the growth of epitaxial GeSn alloys on Ge-buffered silicon. The growth was done using an industrial CVD reactor with a simple manufacturing-compatible chemistry. Using experimental results we decipher the fundamental surface chemical phenomena critical to successful epitaxial growth of GeSn. We found that GeSn growth is initially delayed due to kinetic limitations to the incorporation of Sn in the layer. However once growth is initiated the presence of surface Sn acts to catalyze the growth. This understanding is essential for producing multi-layered epitaxial structures such as multiple quantum wells. Our analysis also indicates that the SnCl_4 and GeH_4 react in the gas-phase to produce intermediates which are critical to facilitating growth at low temperatures.

We next studied the relaxation of GeSn by growth beyond the critical thickness and show that the relaxation first occurs through the propagation of 60° misfits from the substrate. However immobile 90° edge dislocations are subsequently formed by the reaction of 60° misfits resulting in defects being confined to the first ~ 150 nm. Continued strain-relaxation allows increased Sn-incorporation resulting in two distinct layers, the first with lower Sn and high defect density and the second with higher Sn and low defect density. We found that the strain, due to lattice mismatch, is the limiting factor in Sn-incorporation. Moreover, the strain limited Sn-incorporation can be overcome by step-grading the Sn-composition and lattice constant. We used this

method to achieve Sn concentrations $> 17\%$ which are fully-relaxed and emitting light at $> 3.0 \mu\text{m}$.

SiH_4 -based growth of the ternary alloy SiGeSn was presented followed by a discussion of p and n-type doping of GeSn. We find that SiH_4 is suitable precursor for ternary alloy growth however the window for quality epitaxial growth is narrowed relative to binary GeSn. B_2H_6 was evaluated as a p-type dopant source and was found to be effective at achieving active carrier concentrations of $\sim 6 \times 10^{19} \text{cm}^{-3}$. In regards to n-type dopant sources PH_3 was found to be inferior to AsH_3 with poor incorporation efficiency and activation, whereas As doping levels $\sim 1 \times 10^{20} \text{cm}^{-3}$ were realized.

The work culminates in the demonstration of optically stimulated lasing in thick GeSn layers and SiGeSn/GeSn multiple quantum wells. Lasing wavelengths ranging from $2\text{-}3 \mu\text{m}$ at temperatures up to 180K are realized in thick layers. The challenges in quantum well growth are discussed and basic QW structures were structurally and optically characterized. Finally we demonstrate SiGeSn/GeSn multiple quantum well layers on a strain-relaxed GeSn buffer. This structure has enabled the first reported Si-Ge-Sn based QW laser operating up to 80K at thresholds as low as 33 kW/cm^2 .

REFERENCES

1. B. Vincent, Y. Shimura, S. Takeuchi, T. Nishimura, G. Eneman, A. Firrincieli, J. Demeulemeester, A. Vantomme, T. Clarysse, O. Nakatsuka, *Microelectronic Engineering*, **88**, 342 (2011).
2. S. Gupta, V. Moroz, L. Smith, Q. Lu, K.C. Saraswat, *Electron Devices, IEEE Transactions on*. **61**, 1222 (2014).
3. R. Soref, *Proceedings of the IEEE*, **81**, 12 (1993)
4. S. Wirths, R. Geiger, N. von den Driesch, G. Mussler, T. Stoica, S. Mantl, Z. Ikonic, M. Luysberg, S. Chiussi, J.M. Hartmann, H. Sigg, J. Faist, D. Buca, D. Grutzmacher, *Nature Photonics*, **9**, 88, (2015)
5. Sattar Al-Kabi, Seyed Amir Ghetmiri, Joe Margetis, Thach Pham, Yiyin Zhou, Wei Dou, Bria Collier, Randy Quinde, Wei Du, Aboozar Mosleh, Jifeng Liu, Greg Sun, Richard A. Soref, John Tolle, Baohua Li, Mansour Mortazavi, Hameed A. Naseem and Shui-Qing Yu, *Appl. Phys. Lett.* **109**, 171105 (2016)
6. F. Gencarelli, B. Vincent, J. Demeulemeester, A. Vantomme, A. Moussa, A. Franquet, A. Kumar, H. Bender, J. Meersschaut, W. Vandervorst, R. Loo, M. Caymax, K. Temst, M. Heyns, *ECS Transactions*, **50** (9) 875 (2012)
7. L. Kormos, M. Kratzer, K. KostECKI, M. Oehme, T. Sikola, E. Kasper, J. Schulze, C. Teichert, *Surface and Interface Analysis*, doi: 10.1002/sia.6134
8. F. Gencarelli, Y. Shimura, A. Kumar, B. Vincent, A. Moussa, D. Vanhaeren, O. Richard, H. Bender, W. Vandervorst, M. Caymax, R. Loo, M. Heyns, *Thin Solid Films*, **590**, 163 (2015)
9. J. Taraci, J. Tolle, J. Kouvetakis, M.R. McCartney, D.J. Smith, J. Menendez, M.A. Santana, *Appl. Phys. Lett.* **78**, 3607 (2001)
10. B. Vincent, F. Gencarelli, H. Bender, C. Merckling, B. Douhard, *Appl. Phys. Lett.* **99**, 152103 (2011)
11. S. Wirths, D. Buca, A.T. Tiedermann, B. Hollander, P. Bernardy, T. Stoica, D. Grutzmacher, S. Mantl, *ECS Transactions*, **50**, 885 (2012)

12. J. Margetis, S. A. Ghetmiri, W. Du, B. R. Conley, A. Mosleh, R. A. Soref, G. Sun, L. Domulevicz, H.A. Naseem, S.Q. Yu, and J. Tolle, *ECS Transactions*, **64** (6) 711 (2014)
13. J. Werner, M. Oehme, A. Schirmer, E. Kasper, J. Schulze, *Thin Solid Films*, **520**, 3361 (2012)
14. Nupur Bhargava, Matthew Coppinger, Jay Prakash Gupta, Leszek Wielunski, and James Kolodzey, *Appl. Phys. Lett.* **103**, 4, 041908 (2013)
15. Xiaochen Sun, Jifeng Liu, Lionel C. Kimerling, and Jurgen Michel, *Appl. Phys. Lett.* **95**, 011911 (2009)
16. M. El Kurdi, T. Kociniewski, P. Ngo, J. Boulmer, D. Debarre, P. Boucaud, J. F. Damlencourt, O. Kermarrec, D. Bensahel, *Appl. Phys. Lett.* **94** (19), 191107 (2009)
17. Suyog Gupta, Blanka Magyari-Kope, Yoshio Nishi, and Krishna C. Saraswat *J. Appl. Phys.* **113**, 073707 (2013)
18. Mee-Yi Ryu, Tom R. Harris, Y. K. Yeo, R. T. Beeler, and J. Kouvetakis, *Appl. Phys. Lett.* **102**, 171908 (2013)
19. E. Kasper, J. Werner M. Oehme, S. Escoubas, N. Burle, J. Schulze, *Thin Solid Films*, **520**, 3591 (2012)
20. N. Von Den Driesch, D. Stange, S. Wirths, G. Mussler, B. Holländer, Z. Ikonc, JM Hartmann, T. Stoica, S. Mantl and D. Grützmacher, *Chemistry of Materials*, **27**, 4693 (2015)
21. H. Jorke, *Surface Science*, **193**, 569 (1988)
22. J.S. Harris, H. Lin, R. Chen, Y. Huo, E. Fei, S. Paik, S.-J. Cho, T. Kamins, *ECS Transactions* **50**, 601 (2012)
23. S.I.Shah, J.E.Greene, L.L.Abels, QiYao, P.M.Raccah, *J. Crystal Growth* **83**, 3(1987)
24. P.R. Pukite, Alex Harwit, S.S. Iyer, *Appl. Phys. Lett.* **54**, 2142 (1989)
25. G. He and H. Atwater, *Phys. Rev. Lett.* **79**, 1937 (1997)
26. Matthew Bauer, Cole Ritter, Peter Crozier, J. Menendez, Jie Ren and J. Kouvetakis, *Applied Physics Letters*, **83**, 2163 (2003)

27. P. Aella, C. Cook, J. Tolle, S. Zollner, A.V.G. Chizmeshya, and J. Kouvetakis, *Applied Physics Letters* **84**, 888 (2004)
28. Junqi Xie, J.Tolle, V.R. D'Costa, C. Weng, A.V.G. Chizmeshya, J. Menendez, J. Kouvetakis, *Solid State Electronics*, **53**, 816 (2009)
29. J. Xie, A.V.G. Chizmeshya, J. Tolle, V.R. D'Costa, J. Menéndez, J. Kouvetakis, *Chemistry of Materials* **22**, 3779 (2010)
30. Chi Xu, Richard T. Beeler, Gordon J. Grzybowski, Andrew V.G. Chizmeshya, David J. Smith, José Menéndez, and John Kouvetakis, *Journal of the American Chemical Society*, **134**, 220756 (2012)
31. S.Wirths, D.Buca, Z.Ikonic, P.Harrison, A.T.Tiedemann, B.Holländer, T.Stoica, G.Mussler, U.Breuer, J.M.Hartmann, D.Grützmacher, S.Mantl, *Thin Solid Films*, **557**, 183 (2014)
32. Joe Margetis, Aboozar Mosleh, Seyed Amir Ghetmiri, Sattar Al-Kabi, Wei Dou, Wei Du, Nupur Bhargava, Shui-Qing Yu, Harald Profijt, David Kohen, Roger Loo, Anurag Vohra, John Tolle, *Materials Science in Semiconductor Processing*, **70**, 38 (2017)
33. C.M. Comrie, C.B. Mtshali, P.T. Sechogela, N. M. Santos, K. van Stiphout, R. Loo, W. Vandervorst, and A. Vantomme, *Appl. Phys. Lett.* **120**, 14 (2016)
34. K.W. Kolasinski, *Surface Science* (Wiley, West Sussex, UK, 2009) 2nd edition, p. 226-379
35. N.M. Hwang, D.V. Yoon, *Journal of Crystal Growth*, **143**, 103 (1994)
36. H.-C. Luan, D.R. Lim, K.K. Lee, K.M. Chen, J. G. Sandland, K. Wada, L. C. Kimerling, *Appl. Phys. Lett.* **75**, 2909 (1999)
37. J.E. Ayers, *Journal Crystal Growth*, **135**, 71, (1994)
38. Hiromu Ishii and Yasuo Takahashi, *J. Electrochem. Soc.* **135**, 1539 (1988)
39. J. Margetis, A. Mosleh, S. Al-Kabi, S. A. Ghetmiri, W. Du, W. Dou, M. Benamara, B. Li, M. Mortazavi, H. A. Naseem, S.-Q. Yu and J. Tolle, *Journal of Crystal Growth*, **463**, 128 (2017)
40. Mark D. Allendorf and Carl F. Melius, *J. Phys. Chem. A*, **109**, 4939 (2005)
41. Kazuo Takahashi, Andreas Kunz, Dirk Woiki, and Paul Roth, *J. Phys. Chem. A*, **104**, 4939 (2000)

42. M. Hierlemann and C. Werner, *Materials Science in Semiconductor Processing*, **3**, 31 (2000)
43. K. Suh and H.H. Lee, *Journal of Applied Physics*, **88**, 4044 (2000)
44. S. Ito, T. Nakamura, and S. Nishikawa, *Appl. Phys. Lett.* **69** (8) 1098 (1996)
45. E. Bauer. *Zeitschrift für Kristallographie* **110**, 372 (1958)
46. Cody V. Cushman, Philipp Brüner, Julia Zakel, George H. Major, Barry M. Lunt, Nicholas J. Smith, Thomas Grehl, and Matthew R. Linford, *Analytical Methods*, **8**, 3419 (2016)
47. C.L. Senaratne, P.M. Wallace, J.D. Wallace, P.E. Sims, J. Kouvetakis, J. Menendez, *J. Appl. Phys.* **120**, 025701 (2016)
48. H.P. Tang, L. Vescan, and H. Luth, *Journal of Crystal Growth*, **116**, 1 (1992)
49. Gregorio H. Coccoletzi, P.H. Hernandez, Noboru Takeuchi, *Thin Solid Films*, **490**, 196 (2005)
50. Liming Wang and Jingsong Zhang, *J. Phys. Chem. A*, **108**, 10346 (2004)
51. Federica Gencarelli, Benjamin Vincent, Jelle De Meulemeester, Andre Vantomme, Roger Loo, Matty Caymax, Marc Heyns, *ECS Journal of Solid State Science and Technology*, **2** (4), 134 (2013)
52. W. Wang , Q. Zhou , Y. Dong , E. S. Tok , and Y.-C. Yeo , *Appl. Phys. Lett.* **106**, 232106 (2015)
53. Aboozar Mosleh, Mourad Benamara, Seyed Amir Ghetmiri, Benjamin R Conley, Murtadha Abdulmueen Alher, Wei Du, Greg Sun, Richard Soref, Joe Margetis, John Tolle, Shui-Qing Yu and, Hameed A Naseem, *ECS Transactions*, **64** (6) 895 (2014)
54. J. Aubin, J.M. Hartmann, A. Gassenq, L. Milord, N. Pauc, V. Reboud, V. Calvo, *J. Crystal Growth*, **473** 20 (2017)
55. V. M. Kaganer, R. Köhler, M. Schmidbauer, R. Opitz, and B. Jenichen, *Phys. Rev. B* **55**, 1793 (1997)
56. Joe Margetis, Shui-Qing Yu, Nupur Bhargava, Baohua Li, Wei Du, John Tolle, *Semiconductor Science and Technology*, **32** (12), 124006 (2017)
57. Y.B. Bolkhovityanov and L.V. Sokolov, *Sem. Sci. Technol.* **27**, 043001 (2012)

58. S.D. Kim, Susan M. Lord, and James S. Harris, *J. Vac. Sci. Technol. B*, **14**, 642 (1996)
59. A. Rockett, T.J. Drummond, J.E. Greene, and H. Morkoc, *J. Appl. Phys.* **53**, 7085 (1982)
60. P. Wynblatt and R.C. Ku, *Surface Science*, **65**, 511 (1977)
61. A. Gassenq, L. Milord, J. Aubin, K. Guilloy, S. Tardif, N. Pauc, J. Rothman, A. Chelnokov,, J. M. Hartmann, V. Reboud, and V. Calvo, *Appl. Phys. Lett.* **109** (2016)
62. Sun, G. and Soref, R. A. and Cheng, H. H., *Journal of Applied Physics*, **108**, 033107 (2010)
63. Nils von den Driesch, Daniela Stange, Stephan Wirths, Denis Rainko, Ivan Povstugar, Aleksei Savenko, Uwe Breuer, Richard Geiger, Hans Sigg, Zoran Ikonc, Jean-Michel Hartmann, Detlev Grützmacher, Siegfried Mantl, Dan Buca, *Small*, **13** (16) 1603321 (2017)
64. J. Xie, A.V.G. Chizmeshya, J. Tolle, V.R. D'Costa, J. Menéndez, J. Kouvetakis, *Chemistry of Materials* **22**, 3779 (2010)
65. S. Mukherjee, N. Kodali, D. Isheim, S. Wirths, J. M. Hartmann, D. Buca, D. N. Seidman, and O. Moutanabbir, *Phys. Rev. B*, **95**, 161402 (2017)
66. M.A. Hall, C. Mui, C.B. Musgrave, *Journal of Physical Chemistry B*, **105** (48) 12068 (2001)
67. Bhargava, J Margetis, J Tolle, *Sem. Sci. Technol.*, **32** (9), 094003 (2017)
68. Junqi Xie, J Tolle, VR D'Costa, C Weng, AVG Chizmeshya, Jose Menendez, John Kouvetakis, *Solid State Electronics*, **53** (8) 816 (2009)
69. T. L. McDonell, N. A. Marks, O. Warschkow, H. F. Wilson, P. V. Smith, and M. W. Radny, *Phys. Rev. B*, **72**, 193307 (2005)
70. Joe Margetis, Sattar Al-Kabi, Wei Du, Wei Dou, Yiyin Zhou, Thach Pham, Perry Grant, Seyed Ghetmiri, Aboozar Mosleh, Baohua Li, Jifeng Liu, Greg Sun, Richard Soref, John Tolle, Mansour Mortazavi, Shui-Qing Yu, *ACS Photonics*, **5** (3), 827 (2018)
71. Casey Jr. H. C. T, *J. Appl. Phys.* **56**, 1959 (1984).

72. Miller, R. C. *J. Appl. Phys.* **47**, 4509 (1976).
73. G. Sun, S.Q. Yu, *Solid State Electronics*, **83**, 76 (2013)
74. Wei Dou, Seyed Amir Ghetmiri, Sattar Al-Kabi, Aboozar Mosleh, Yiyin Zhou, Bader Alharthi, Wei Du, Joe Margetis, John Tolle, Andrian Kuchuk, Mourad Benamara, Baohua Li, Hameed A. Naseem, Mansour Mortazavi, Shui-Qing Yu, *Journal of Electronic Materials*, **45** (12) 6265 (2016)
75. Chia-Liang Cheng, Dah-Shyang Tsai, Jyh-Chiang Jiang, *Surface Science*, **600** (16) 3194 (2006)